

AMERICAN UNIVERSITY OF BEIRUT

CATALYTIC PYROLYSIS OF WASTE RUBBER

by
AYMAN MOHAMMAD HIJAZI

A thesis
submitted in partial fulfillment of the requirements
for the degree of Master of Science in Chemical Engineering
to the Department of Chemical and Petroleum Engineering
of the Faculty of Engineering and Architecture
at the American University of Beirut

Beirut, Lebanon
January 2017

AMERICAN UNIVERSITY OF BEIRUT

CATALYTIC PYROLYSIS OF WASTE RUBBER

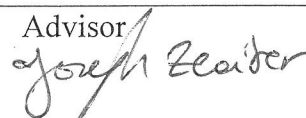
by

AYMAN MOHAMMAD HIJAZI

Approved by:

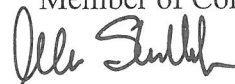
Dr. Joseph Zeaiter, Assistant Professor
Department of Chemical and Petroleum Engineering

Advisor



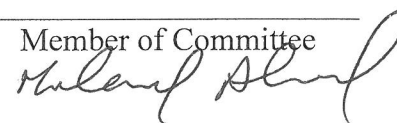
Dr. Alan Shihadeh, Interim Dean & Professor
Department of Mechanical Engineering

Member of Committee



Dr. Mohammad Ahmad, Chairperson & Professor
Department of Chemical and Petroleum Engineering

Member of Committee



Date of thesis defense: January 30, 2017

AMERICAN UNIVERSITY OF BEIRUT

THESIS, DISSERTATION, PROJECT RELEASE FORM

Student Name: Hijazi Ayman Mohammad
Last First Middle

Master's Thesis Master's Project Doctoral Dissertation

I authorize the American University of Beirut to: (a) reproduce hard or electronic copies of my thesis, dissertation, or project; (b) include such copies in the archives and digital repositories of the University; and (c) make freely available such copies to third parties for research or educational purposes.


I authorize the American University of Beirut, to: (a) reproduce hard or electronic copies of it; (b) include such copies in the archives and digital repositories of the University; and (c) make freely available such copies to third parties for research or educational purposes

after:

One ---- year from the date of submission of my thesis, dissertation, or project.

Two ---- years from the date of submission of my thesis, dissertation, or project.

Three years from the date of submission of my thesis, dissertation, or project.

 13 February 2017

Signature

Date

ACKNOWLEDGEMENTS

My most sincere thanks go to my advisor Dr. Joseph Zeaiter. He gave me the opportunity to conduct state of art scientific research. I thank him for his continuous guidance during experimental work. Last but not least, he taught me self-discipline and guided me towards higher research strength.

I am grateful to my committee members: Dr. Mohammad Ahmad and Dr. Alan Louis Shihadeh. They have provided me with valuable academic expertise and helped me perform towards the completion of my masters of science.

Especially, I thank my co-advisor Dr. Mohammad Ahmad for his great help as an academic advisor. His insights and believes in my abilities gave me the opportunity to be enrolled in the academic research at American University of Beirut.

Many thanks for Mr. Marc Ayoub and Mr. Nicolas Aramouni for their extensive assistance in the technical work.

Special thanks for Mr. Adnan El Makdah and Mr. Mohammad Baassiri for their academic assistance during the whole duration of my masters' degree.

I want to express my sincere gratitude to IBC SAL Company and particularly the general manager Mr. Nabil Zantout for providing me the permission to conduct my graduate studies in parallel with my industry duties.

I would like to express my eternal gratitude to my parents and family for their everlasting love and support.

AN ABSTRACT OF THE THESIS OF

Ayman Mohammad Hijazi for Master of Science
Major: Chemical Engineering

Title: Catalytic Pyrolysis of Waste Rubber

The waste crisis striking most countries has made it crucial to consider treatment methods that would leave minimal impact on the environment. Statistics show that rubber tires contribute to a significant portion of waste on local and global scales. Different techniques have been developed to cope with waste tires, one of which is pyrolysis. This work aims at enhancing two types of pyrolysis, namely thermal pyrolysis and solar pyrolysis, by using different catalysts. Thermal pyrolysis temperature is fixed at 590 °C, whereas solar pyrolysis is conducted at an irradiation between 900-1100 W/m².

Nine catalysts are synthesized based on the acidic Hbeta zeolite structure, Hbeta, Pd/Hbeta, Pt/Hbeta, Pd-Pt/Hbeta and on the semi-conductor TiO₂ photo active catalyst, TiO₂, Pd/TiO₂, Pt/TiO₂, Pd-Pt/TiO₂, and Bi₂O₃/SiO₂/TiO₂. Thermal pyrolysis results highlighted the enhancement effect of palladium noble metal that gave the highest pyrolytic gas yield of 37.02%, while Hbeta zeolite gave 27.89% only. On the other hand, solar pyrolysis with photocatalytic Pd/TiO₂ produced the highest gas yield of 40.94%. The pyrolysis oil samples were collected and characterized using GC-MS to determine the carbon chain length which is found to decrease to C₉-C₁₂ gasoline range under Pd/Hbeta and Pd/TiO₂.

Meanwhile, catalyst behavior and activity were investigated using several techniques including; BET isotherm, SEM, EDX, and XRD. The highest surface area for Hbeta zeolite based catalysts was 449 m²/g for Pd/Hbeta zeolite. While the semi-conductor TiO₂ based catalyst, Pd-Pt/TiO₂ gave a surface area of 130.9 m²/g. Palladium metal produced the highest dispersion on the support surface and inside the pores. The bimetallic Hbeta zeolite catalyst and the tri-metallic Bi₂O₃/SiO₂/TiO₂ catalyst had a layered structure as detected by SEM.

Palladium noble metal doping showed a significant enhancement for both Hbeta acidic surface and photo active semi-conductor TiO₂. Pd/ Hbeta zeolite provoked the dehydrogenation-hydrogenation mechanism that resulted in enhancing metal-acidic catalyst activity. Pd/ TiO₂, enhanced photo activity by preventing the charge-hole recombination and decreased the binding energy between the valence band and conduction band.

CONTENTS

ACKNOWLEDGEMENTS	v
ABSTRACT	vi
LIST OF ILLUSTRATIONS	xii
LIST OF TABLES	xiv

Chapter

I. INTRODUCTION	1
II. LITERATURE REVIEW	3
A. Waste tire constituents	3
B. Waste tires as feedstock for pyrolysis.....	4
C. The Pyrolysis Process	5
D. Waste tire pyrolysis complex reactions and mechanisms.....	8
E. Types of pyrolysis.....	9
1. Slow pyrolysis.....	10
2. Fast pyrolysis	10
3. Catalytic pyrolysis	11

F.	Parameters affecting tire pyrolysis.....	12
1.	Feedstock composition.....	12
2.	Temperature factor.....	15
a.	Temperature effect on liquid yield.....	20
b.	Temperature effect on gas fraction.....	21
c.	Temperature factor on solid fraction.....	22
3.	Particle Size	24
4.	Carrier gas flow rate:	25
G.	Catalysis.....	26
1.	Acidic Catalysts	26
2.	Photoactive Catalysts.....	34
a.	Charge carriers	41
b.	Surface chemistry factor.....	42
H.	ENERGY ECONOMICS.....	45
I.	ENVIRONMENTAL ASPECTS.....	47
J.	RESEARCH OBJECTIVE	50
III.	METHODOLOGY	51
IV.	CATALYST PREPARATION.....	52
A.	Synthesis Methods	52
1.	Hbeta zeolite Support.....	52
a.	Hbeta zeolite preparation	53
i.	Materials	53
ii.	Procedure.....	53
b.	Pd (0.25wt. %) / Hb zeolite.....	54
i.	Materials	54
ii.	Procedure.....	54
c.	Pt (0.25wt. %) / Hb zeolite.....	54

i.	Materials	54
ii.	Procedure	55
d.	Pt (0.5mol%)-Pd (0.5mol %) /Hb zeolite	55
i.	Materials	55
ii.	Procedure	56
2.	Titanium dioxide Support	56
a.	Pd (0.25wt. %) /TiO ₂	56
i.	Materials	56
ii.	Procedure	57
b.	Pt (0.25wt. %) /TiO ₂	57
i.	Materials	57
ii.	Procedure	57
c.	Pt (0.5mol%)-Pd (0.5mol %) /TiO ₂	58
i.	Materials	58
ii.	Procedure	58
d.	SiO ₂ (5wt. %) /TiO ₂ / Bi ₂ O ₃ (5wt. %)	59
i.	Materials	59
ii.	Procedure	59
B.	Synthesis Stoichiometric Calculations	60
1.	Hb zeolite support	60
a.	Hb zeolite	60
b.	Pd (0.25wt. %) / Hb zeolite	61
c.	Pt (0.25wt. %) / Hb zeolite	61
d.	Pt (0.5mol%)-Pd (0.5mol %) /Hb zeolite	62
2.	Titanium dioxide Support	64
a.	Pd (0.25wt. %) /TiO ₂	64
b.	Pt (0.25wt. %) /TiO ₂	64
c.	Pt (0.5mol%)-Pd (0.5mol %) /TiO ₂	65
d.	SiO ₂ (5wt. %) /TiO ₂ / Bi ₂ O ₃ (5wt. %)	67
V. EXPERIMENTAL		70
A.	Thermal Pyrolysis	70
B.	Solar Pyrolysis	73

C. Gas Yield Calculation	74
VI. CATALYST CHARACTERIZATION	75
A. BET Isotherm	75
B. XRD Analysis	77
C. SEM Analysis	77
D. EDX Analysis	78
VII. RESULTS AND DISCUSSION	79
A. Characterization	79
1. BET Isotherm Analysis	79
2. XRD Analysis	88
3. SEM Analysis	97
4. EDX analysis	104
B. Pyrolysis Results	113
1. Thermal Pyrolysis	113
2. Solar Pyrolysis	123
C. Pyrolytic Oil Analysis	128
VIII. CONCLUSION	132
Appendix	134
BIBLIOGRAPHY	135

ILLUSTRATIONS

Figure	Page
1. Waste tire pyrolysis empirical Formula.....	9
2. Constant Liquid, solid and gas (Martínez et al. 2013).....	18
3. Liquid: decreases, Solid: constant, gas: increases (Martínez et al. 2013).....	19
4. Solid: increase, gas: increase and liquid: decrease (Martínez et al. 2013).	19
5. SiO ₄ tetrahedra building unit for zeolite (Chorkendorff and Niemantsverdriet 2003)	27
6. Hbeta zeolite framework and pore structure.....	29
7. Bronsted Acid site of zeolite (Chorkendorff and Niemantsverdriet 2003).....	30
8. Examples of hydroxyl groups in zeolites (Cejka et al. 2010).....	31
9. Formation of Lewis Acid by dehydroxylation of zeolite (Cejka et al. 2010).....	32
10. Similar electrochemistry for different photocatalytic processes (Wen et al. 2015a)	37
11. Surface chemistry reactions (Wen et al. 2015a)	43
12. Acidic surface formations by sulfate ions on Titanium surface (Wang et al. 2005c)	44
13. Electric furnace unit.....	70
14. Thermal furnace heating compartments.....	71
15. Fixed bed reactor (FBR): rubber pieces (black), cotton glass (blue), and catalyst (red).....	71
16. Automated solar unit (Zeaiter et al. 2015).....	73
17. Type II BET isotherm (Chorkendorff and Niemantsverdriet 2003).....	76
18. Hbeta zeolite BET adsorption/desorption curve.....	81
19. Pt/Hbeta zeolite BET adsorption/desorption curve.....	81
20. Pd/Hbeta zeolite BET adsorption/desorption curve.....	82
21. Pt-Pd/Hbeta zeolite BET adsorption/desorption curve.....	82
22. TiO ₂ semi-conductor BET adsorption/desorption curve.....	83
23. Pd/TiO ₂ semi-conductor BET adsorption/desorption curve.....	84
24. Pt /TiO ₂ semi-conductor BET adsorption/desorption curve.....	84
25. Pt-Pd/TiO ₂ semi-conductor BET adsorption/desorption curve.....	85
26. SiO ₂ /TiO ₂ / Bi ₂ O ₃ BET adsorption/desorption curve	85
27. BET Type IV adsorption/desorption isotherm (Chorkendorff and Niemantsverdriet 2003)	87
28. Hbeta zeolite catalyst XRD results at 2θ, WL=1.54060.....	89
29. Pd/Hbeta zeolite XRD results at 2θ, WL=1.54060.....	90
30. Pt/Hbeta zeolite XRD results at 2θ, WL=1.54060.....	91
31. Pt-Pd/Hbeta zeolite XRD results at 2θ, WL=1.54060	91
32. TiO ₂ semi-conductor pure anatase XRD results at 2θ, WL=1.54060.....	92
33. Pd/TiO ₂ semi-conductor XRD results at 2θ, WL=1.54060.....	93
34. Pt/TiO ₂ semi-conductor XRD results at 2θ, WL=1.54060	93
35. Pt-Pd/TiO ₂ semi-conductor XRD results at 2θ, WL=1.54060.....	94
36. SiO ₂ /TiO ₂ /Bi ₂ O ₃ XRD results at 2θ, WL=1.54060.....	94

37. (SEM) Scanning electron microscope image for Hbeta zeolite.....	98
38. (SEM) Scanning electron microscope image for Pd/Hbeta zeolite	98
39. (SEM) Scanning electron microscope image for Pt/Hbeta zeolite	99
40. (SEM) Scanning electron microscope image for Pt-Pd/Hbeta zeolite.....	99
41. (SEM) Scanning electron microscope image for TiO ₂ semi-conductor	100
42. (SEM) Scanning electron microscope image for Pd/TiO ₂ semi-conductor	101
43. (SEM) Scanning electron microscope image for Pt/TiO ₂ semi-conductor	101
44. (SEM) Scanning electron microscope image for Pd-Pt/TiO ₂ semi-conductor..	102
45. (SEM) Scanning electron microscope image for Bi ₂ O ₃ /SiO ₂ /TiO ₂	102
46. (EDX) Energy dispersive x-ray spectrum for Pd/Hbeta zeolite catalyst	105
47. (EDX) Energy dispersive x-ray spectrum for Pt/Hbeta zeolite catalyst	106
48. (EDX) Energy dispersive x-ray spectrum for Pt-Pd/Hbeta zeolite catalyst.....	107
49. (EDX) Energy dispersive x-ray spectrum for Pt/TiO ₂ semi-conductor catalyst	108
50. (EDX) Energy dispersive x-ray spectrum for Pd/TiO ₂ semi-conductor catalyst	109
51. (EDX) Energy dispersive x-ray spectrum for Pt-Pd/TiO ₂ semi-conductor catalyst	110
52. (EDX) Energy dispersive x-ray spectrum for Bi ₂ O ₃ /SiO ₂ /TiO ₂ catalyst.....	111
53. Pyrolysis products: Pyrolytic gas, pyrolytic oil, and carbon black (char) (Ahoor and Zandi-Atashbar 2014)	113
54. Examples about zeolite selectivity (Chorkendorff and Niemantsverdriet 2003)	117
55. Pyrolytic oil samples diluted with ethanol.....	128
56. Carbon number distribution in pyrolytic oil with two different catalysts: Hbeta zeolite (Dotted) & Pd/Hbeta (Diagonal).....	129
57. Carbon number distribution in pyrolytic oil with semi-conductor catalysts: TiO ₂ (Dotted) & Pd/TiO ₂ (Diagonal)	130

TABLES

Table	Page
1. Elemental and proximate analysis, and calorific value of different tires reported in literature (Martínez et al. 2013).....	5
2. chemical compositions of tires (Rubber Manufactures Association 2010).	13
3. Temperature for degradation of the main type compounds reported in literature (Martínez et al. 2013).....	14
4. Pyrolysis product yields reported in literature with null effect of temperature parameter change of yields. (Martínez et al. 2013)	16
5. Temperature effect on pyrolysis product yields reported in literature. (Martínez et al. 2013)	17
6. Zeolite types composition and geometry	28
7. Metals/ acidic supported catalysts (Chorkendorff and Niemantsverdriet 2003)	34
8. CO ₂ emissions from combustion of fossil fuels and volatiles released in waste tire pyrolysis (International Energy Agency 2009)	48
9. BET isotherm analysis results: Surface area (m ² /g), pore size (nm), and pore volume (cc/g)	80
10. Composition analysis for the selected spectrum on point 32.....	105
11. Composition analysis for the selected spectrum on point 6.....	106
12. Composition analysis for the selected spectrum on point 4.....	107
13. Composition analysis for the selected spectrum on point 8.....	108
14. Composition analysis for the selected spectrum on point 1.....	109
15. Composition analysis for the selected spectrum on point 29.....	110
16. Composition analysis for the selected spectrum region 1.....	111
17. Thermal pyrolysis gas yield results in the presence of nitrogen carrier gas	114
18. Solar pyrolysis gas yield results in the presence of nitrogen carrier gas	123

CHAPTER I

INTRODUCTION

The extensive high usage of fossil fuel has pushed it to depletion, in addition to the generation of harmful pollutants including SO₂, NO_x and VOCs, which have negative impact on the environment (World Business Council for Sustainable Development 2011). Parallel to the solid waste disposal problem, waste tires have been one of the most critically polluting sources. It was reported that around 1.4 billion new tires are sold across the world each year and afterward just as many fall into the category of end-of-life tires (European Tyre & Rubber Manufacturers' Association 2011). In units sold, passenger car tires represent more than 90% whilst truck tires and other categories constitute the remaining 10% (Shulman 2004). It is estimated that one car tire per person is discarded each year in developed countries hence, 1 billion waste tires are disposed-off globally each year. At Present, an estimated 4 billion waste tires are dumped in landfills or stockpiled worldwide (World Business Council for Sustainable Development 2011). Another worrying number shows that there are 3.2 million tons of tires (out of 4.5 million tons of produced tires in 2010) discarded annually from EU27 countries and Turkey. This represents around 26.5% of the world tire production (17 million tons) (European Tyre & Rubber Manufacturers' Association 2011). As a result, the disposal of waste tire is considered as an increasing environmental and economic problem (Williams et al. 1995).

Therefore, the aim of waste tire disposal solution has the same logical approach as any other type of waste, which is to minimize the dangerous impact of the material on the environment by recycling, energy recovery and landfilling (Aguado et al. 2008). It is essential to take into consideration that rules and legislations are pushing research for new

techniques that lower environmental hazards and find suitable solution for disposal management. For instance, waste tire landfilling is banned in the EU (European Council Directive 1999). Hence, thermochemical alternative processes such as pyrolysis, gasification and incineration would contribute to waste minimization while maximizing energy savings.

This thesis is structured as follow: First, the literature review section introduces waste tire material and its constituents along with the pyrolysis process, parameters affecting tire pyrolysis and the types of possible acidic and photo active catalysts to be used. Then, energy economics and environmental aspects are discussed to highlight the need of a sustainable and green waste treatment technology such as pyrolysis. This is followed by highlighting the research objectives and application steps. The reader is guided afterwards to the catalyst preparation and synthesis methods section. The experimental section explains the two different setups that adopt thermal and solar pyrolysis. In addition, all characterization techniques used to analyze the catalysts are shown in the catalyst characterization part. In the section that follows, thermal and solar pyrolysis test runs and results are presented. Finally, the conclusion section summarizes achieved project outcomes and recommendations for further research.

CHAPTER II

LITERATURE REVIEW

A. Waste tire constituents

The materials that tires are made up of are rubber, which constitute 60-65%, carbon black (CB) that represents 25-35% in addition to accelerators and fillers. The rubber portion is considered as hydrocarbons in the form of C_xH_y (Leung and Wang 1998), a combination between natural rubber (NR) that originates from Hevea tree and synthetic rubber (SR) that is derived from petroleum derivative (Shulman 2004). Natural rubber (NR) is a principal constituent of rubber tire due to its elastic specifications. The existence of elastic polymers gives the rubber tire an enhanced mechanical and durability strength (Shulman 2004).

Concerning the carbon black fraction, it originates in the form of amorphous carbon of quasi-graphitic structure by partially combusting fossil hydrocarbons. This material is mixed with rubber in order to increase its strength (Martínez et al. 2013). In addition, there is 7 wt. % of organic and 3 wt. % of inorganic fillers due to the added extender oil that is made up of aromatics, naphthenic and paraffinic hydrocarbons. The aim of oil addition is to have softer rubber (Martínez et al. 2013).

It is important to know that not all tires have the same composition and there are different compounds that differ from brand to another (Mastral et al. 1999a; Mastral et al. 2000b).

The process of rubber tire manufacturing includes vulcanization, by which elastic polymers react with sulfur and other chemicals to produce crosslinks between the elastic polymers. These 3-D rearrangements add more strength and elasticity and reduce the rate of decomposition of rubber tires (Isayev 2005). Vulcanization is non-reversible

and includes the addition of catalyst that is made up of accelerator (organic-sulfur compound), ZnO and stearic acid. These additives can serve as rubber physical properties enhancers (Mastral et al. 1999a; Mastral et al. 2000b; Williams and Besler 1995; Kyari et al. 2005). Sulfur content originating from accelerator additives occupy around 1.5 wt. % of the rubber tire (Mastral et al. 2000b).

B. Waste tires as feedstock for pyrolysis

Scrap tires represent a cheap and readily accessible source of chemicals and fuel derivatives. Their conversion by pyrolysis can produce gaseous and liquid products of similar quality to petroleum fuel. Any fuel considered as a source of energy is analyzed to determine the amount of moisture, volatile matter, fixed carbon and ash. Concerning the composition of a rubber tire, the volatile fraction consists mainly of polymeric compounds and the solid fraction of fixed carbon represents the carbon black used during tire manufacturing (de Marco Rodriguez et al. 2001a).

The proximate and elemental analysis, in addition to calorific values, of rubber tires (on steel free basis) are reported in several references as shown in Table 1. It is observed that various ash contents (2.4% to 20.12 %), volatile matter (57.50% to 73.74%) and fixed carbon (19.45% to 32.28%) can be obtained depending on the type of tires. Therefore, the pyrolysis products percentages will vary between different tire brands (Martínez et al. 2013, Cypres and Bettens 1989).

Elemental analysis on dry basis (wt%)						Proximate analysis on as received basis (wt%)				CV (MJ/kg)
C	H	N	S	O	A	A	VM	FC	M	
81.72	6.54	0.55	1.87	2.68	6.64	6.64	62.58	30.07	0.71	n.r.
83.80	6.90	0.60	2.00	2.30	4.40	4.30	63.40	30.40	1.90	n.r.
83.80	7.60	0.40	1.40	3.10	3.70	3.70	67.30	28.50	0.50	36.45 ^a
82.36	6.92	2.30	1.40	2.03	5.00	4.95	73.74	20.22	1.09	37.06 ^b
75.50	6.75	0.81	1.44	15.50 ^c		20.10	57.50	20.85	1.53	29.18 ^{a,e}
85.90	8.00	0.40	1.00	2.30	2.40	2.40	66.50	30.30	0.80	40.0 ^a
75.40	7.03	0.21	1.62	5.09	10.21	10.21	62.32	26.26	1.31	33.29 ^a
84.33	7.81	0.49	1.66	3.32	2.40	7.10	62.20	29.40	1.30	40.0 ^a
82.80	7.60	0.50	1.30	4.50	3.30	3.30	68.70	27.20	0.80	36.46 ^a
86.70	8.10	0.40	1.40	1.30	2.10	8.00	61.90	29.50	0.70	36.20 ^a
80.29	7.25	0.31	1.84	4.90	5.41	5.30	67.50	25.20	2.10	37.30 ^b
85.05	6.79	0.50	1.53	1.75	4.40	4.35	62.24	32.28	1.14	34.90 ^a
81.50	7.10	0.50	1.40	3.40	6.10	6.07	64.87	28.56	0.50	36.80 ^a
86.09	6.74	0.19	1.93	1.35	3.70	3.70	65.50	29.40	0.90	n.r.
86.70	6.90	0.30	1.90	0.90	3.30	4.40	64.00	30.70	0.90	31.80 ^b
83.92	6.83	0.78	0.92	3.39	4.16	4.16	64.97	30.08	0.75	38.6 ^{a,c}
85.25	7.94	0.41	1.38	1.19	3.83	3.83	64.09	31.14	0.94	n.r.
83.00	6.79	0.32	1.37	3.46	5.06	5.00	64.10	29.70	1.20	35.00 ^b
67.08	6.12	0.17	2.05	24.58 ^c		19.10	59.69	19.45	1.72	27.37 ^a
81.79	7.99	0.48	1.81	3.04	4.90	4.88	65.74	28.98	0.40	38.30 ^{a,d}
84.00	7.19	0.49	1.42	3.30	3.60	3.60	65.60	30.00	0.80	38.80 ^a
83.15	6.78	0.28	1.77	0.84 ^d	7.10	7.10	61.90	29.90	1.10	37.35 ^a
74.30	7.20	0.90	1.71	15.89 ^c		18.90	58.20	21.30	1.60	30.50 ^{a,e}
83.20	7.70	1.50	1.44	6.16 ^c		5.00	66.10	27.50	1.40	33.40 ^{a,f}

n.r., not reported; A, ash; VM, volatile matter; FC, fixed carbon; M, moisture.

^a Higher.

^b Lower.

^c Including ash.

^d Mixture between passenger car and truck tyres.

^e Passenger car tyre.

^f Truck tyre.

^g Motorcycle tyre.

Table 1 Elemental and proximate analysis, and calorific value of different tires reported in literature (Martínez et al. 2013).

In comparison with coal (Mastral et al. 1999b), rubber tires are very different in terms of moisture and ash contents, however, only small differences exist for the contents of C and S and very similar values regarding N and H.

C. The Pyrolysis Process

It is considered that waste tires are one of the most difficult candidates for waste management because of their durable structure. They are made up of 3-D elastic polymer networks that allow them to handle harsh conditions including mechanical stresses and weather.

It is reported that tire lifetime in landfills ranges between 80 to 100 years due to the difficulty of the constituting polymers to be separated into their constituents' chemical components (Bennett 1993).

One can argue that incineration can act as an efficient technique to recover energy out from waste rubber tires. However, large emissions of dioxins, PAHs, VOCs and particulate matter are produced when waste tires are burnt and therefore, this option is always avoided due to its severe negative impact on the environment (Mastral et al. 1999a; Mastral et al. 2000b; Levendis et al. 1996; Conesa et al. 2008).

Additional numbers show to which extent combustion has bad impact on environment. For instance, since the 1970's, significant quantities of Zn particles are emitted from combustion of rubber tires (Buekens 1977). This was confirmed by (Gieré et al. 2006) who found that Zn quantities jumped from 15g/h to 2.4 kg/h if coal and rubber tire were burned in a ratio of 19:1 (e.g. in coal fired power plants). When waste tires are mixed with coal in cement kilns (of a cement plant with a capacity of one million tons of cement per year), emissions of CO and SO₂ increased by 47% and 30% respectively, and a decrease by 15% of NO_x were reported (Carrasco et al. 1998).

Coal and rubber tire combustion were compared from PAHs emissions perspective. PAHs emissions from the combustion of tires were 15-20 times higher than coal combustion (Levendis et al. 1996). The reason behind PAHs emissions is the presence of CB (carbon black) constituent of rubber tires with their high surface/weight ratio that adsorbs PAHs depositions (Mastral et al. 2000a).

On the other hand, pyrolysis has been utilized for producing high-energy products since 1700s to 1900s. It produced charcoal from biomass for thousands of years.

In fact, the pyrolysis of coal and biomass (especially wood) produces fuel gas and smokeless solid fuel (Rezaiyan and Cheremisinoff 2005).

The term pyrolysis has several synonyms, such as, thermal distillation or thermolysis. It is a thermochemical treatment that involves breaking apart chemical bonds (Wampler 2006) via thermal decomposition under either inert gas medium or vacuum, in order to prevent non-oxidative conditions of feedstock. Pyrolysis can also be defined as reverse polymerization, thermal depolymerization or polymer cracking. The main benefit of the pyrolysis process is the ability to convert wastes that are difficult to recycle into reusable products (Scheirs and Kaminsky 2006).

Through this thermochemical treatment, solid wastes are transformed into high calorific fuels, chemicals, monomers or other valuable materials. The generated products are high-energy-density volatile gases and carbonaceous solids known as carbon black. The volatile gases produced can be divided into two portions; condensable high molecular weight compounds and low molecular weight compounds known as syngas or pyro gas (Rezaiyan and Cheremisinoff 2005).

The operating temperature for waste rubber pyrolysis should be higher than 400°C. The process is held in the absence of oxygen, such that once the feedstock is heated up to threshold temperature, numerous reactions including dehydration, cracking, isomerization, dehydrogenation, aromatization and condensation would occur (Rezaiyan and Cheremisinoff 2005). The resulting compounds are considered to be hydrocarbons with a large range of carbon chains that extend from light alkane gases to heavy complex coke. Therefore, process conditions or process characteristics such as particle size, temperature, reaction time, heating rate, and inert flow rate can be manipulated to achieve desired yields (Scheirs 2006a).

D. Waste tire pyrolysis complex reactions and mechanisms

Rubbery materials consists of carbon-carbon double bonds, which are decomposed when prone to thermal treatment to produce highly reactive free radicals (Dodds et al. 1983). The thermal degradation process according to a radical chain reaction pathway comprising hydrogen transfer steps along with the progressive breaking of the polymer backbone is fully described (Aguado et al. 2006). To study the thermal degradation of natural rubber, pyrolysis gas chromatography at 500°C was used by (Groves et al. 1991). According to their work it was concluded that there is a probability for monomer recombination by Diels-Alder mechanism that will form dimer compounds during rubber pyrolysis. Meanwhile, (Mastral et al. 2000b) also suggested a possible reaction pathway for rubber tire conversion through polyisoprene depolymerization and further cyclisation. (Pakdel et al. 2001) proposed that the polyisoprene of the rubber thermally decomposes through a β -scission mechanism to an isoprene intermediate radical. These intermediate radicals will transfer into isoprene molecules (depropagation) in the gas phase, which will dimerize to dipentene. In addition, (Kwon and Castaldi 2009) claimed that thermal degradation of waste tire takes place via bond scission on each monomer of the chain composing rubber tires, followed by hydrogenation and recombination by gas phase reaction between monomers produced.

From all of the above research papers, it is clear that thermal pyrolysis process involves multiple reactions taking place in three stages:

- Primary pyrolysis
- Secondary post cracking reaction of pyrolytic volatiles that has a great impact on BTX yields
- Pyrolytic carbon black gasifying reaction with CO₂/H₂O/O₂ (Li et al. 2004a).

The influence that each group of reaction can be imposed on the overall pyrolysis process is linked to two parameters: temperature and reaction time.

To wrap up, an empirical formula based on mass conservation enables a workable and feasible pyrolysis reaction scheme (Buekens 2006).

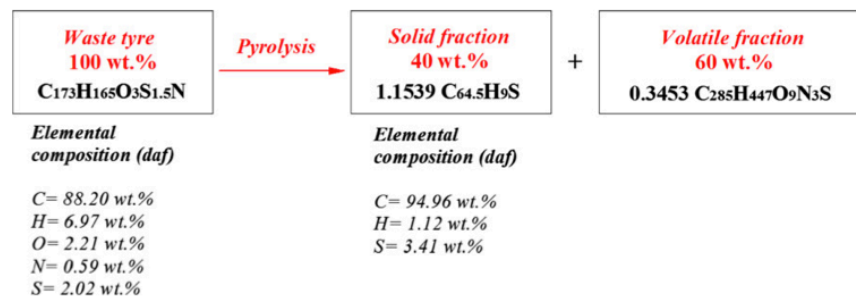


Figure 1 Waste tyre pyrolysis empirical Formula

Figure 1 shows that waste tires are composed of hydrocarbons with main elements of; carbon, hydrogen, oxygen, nitrogen and sulfur. These will decompose under thermal treatment into fixed solid known as carbon black and volatile products containing both heavy and light (noncondensable) portion. A conversion of 60 wt. % to volatiles can be reached. For simplicity, it is assumed that only the hydrocarbon-organic fraction of waste tires will undergo pyrolysis (Buekens 2006).

E. Types of pyrolysis

As mentioned above, the temperature, heating rate and volatiles residence time are critical parameters that can affect the pyrolysis process output. Accordingly, pyrolysis can be classified under several types. For example, the pyrolysis process can be divided

into two main categories, which are slow and fast pyrolysis. Pyrolysis termed fast is relevant to higher heating rates and less volatile residence time (Martínez et al. 2013). It is reported by (Martínez et al. 2013) that the pyrolysis process, which is conducted in the absence of oxygen can be performed in other environments instead. Accordingly, pyrolysis is classified into oxidative pyrolysis, hydro-pyrolysis, steam-pyrolysis, and catalytic-pyrolysis and vacuum pyrolysis. In addition, pyrolysis classification can be based on heating system used, for instance, microwave or plasma pyrolysis.

1. Slow pyrolysis

This type of pyrolysis is related to sluggish pyrolytic cracking such that there will be longer residence time at low temperatures with low heating rates. The longer time pyrolysis process takes, the more coke, tar as well as thermally stable products via secondary conversion occur (Buekens 2006). Therefore, char production is the major target product (as residues) by slow pyrolysis although tar and gases are also obtained but not retrieved.

2. Fast pyrolysis

This type of pyrolysis is relevant to fast thermal cracking by high heating rates. For fast pyrolysis, volatile products are removed fast enough to allow the formation of liquid products. The volatiles released will condense before further reaction into simpler gaseous compounds within shorter residence time. A small feedstock particle size is needed to conduct fast pyrolysis (Cunliffe and Williams 1998). As a result of the early removal of volatile compounds, a higher calorific liquid fuel is obtained due to more complexity of liquids. Hence, it is taken into consideration that fast pyrolysis favors the

production of liquid fuels, chemical and derived products with higher yields (Martínez et al. 2013).

The short residence time for fast pyrolysis ranges from milliseconds to seconds. According to (Bridgwater and Peacocke 2000) the residence time of the volatile portion of waste tires should be below 2 seconds. As residence time increases, the process starts to mimic slow pyrolysis with a reduction in volatile organic yield due to further secondary reactions.

3. Catalytic pyrolysis

The pyrolytic yield and products are highly linked to the feedstock composition, process temperature and heating rates. Fortunately, the quality of pyrolytic products and yield can be manipulated by adding certain catalysts to the pyrolysis process. For instance, by using zeolite catalysts (Y-type and ZSM-5) the production of single ring aromatic compounds in the liquid fraction is enhanced (Williams and Brindle 2002). In addition, (Kar 2011) used an expanded perlite catalyst to enhance the liquid fraction yield and its fuel properties. (Zhang et al. 2008) revealed that the NaOH addition favored lower pyrolysis temperatures. The routes of production of liquid portions are enhanced up to 49.7 wt. % at 480 °C together with higher hydrogen in the gas. Using Ru/MCM-41 catalyst increased the gas fraction over the liquid (Dũng et al. 2009). Meanwhile, higher H₂ and CO concentrations and a decrease in CH₄ and C₂-C₄ concentrations are encountered in a two-stage pyrolysis-gasification process at 500-800°C in the presence of Ni-Mg-Al (1:1:1) catalyst (Elbaba et al. 2010).

F. Parameters affecting tire pyrolysis

Due to the endothermic aspect of thermal degradation, the most effective parameters in pyrolysis is temperature (Martínez et al. 2013). Thermodynamically, temperature is related to equilibrium conversion (X_e) such that as temperature increases, the equilibrium conversion decreases for exothermic reactions and increases for endothermic reactions. Therefore, temperature has a great impact on both products and conversion grade (Martínez et al. 2013).

Furthermore, pyrolysis time factor has a direct link with particle size and heating rate that influence each other and the overall heat transfer mechanism. As a result, gas, liquid and solid distributions and their physicochemical properties are effected (Martínez et al. 2013).

The pyrolysis process is usually conducted in the absence of oxygen, inert gases such as nitrogen or argon are generally used. Hence, the type and flowrate of the carrier gas are considered an important parameter. It affects the stimulus on secondary pyrolysis reactions, including, recondensation, char formation, re-polymerization and thermal cracking (Martínez et al. 2013). It is also worth noting that pressure together with feedstock composition also play a major role in product yield and composition (Martínez et al. 2013).

1. Feedstock composition

Rubber tires are mainly consisted of natural rubber and synthesized rubber that contribute to the volatile fraction. In addition, carbon black is another major constituent of rubber tires that is included in the process, which refers to fixed carbon. Rubber tires produced are of various types depending on the brand and production process utilized

(Williams and Besler 1995; Kyari et al. 2005; Islam et al. 2008; Mastral et al. 1996). The produced rubber tires are classified into different classes depending on the different proportions of natural rubber and synthesized rubber (Rubber Manufactures Association 2010). Table 2 shows different groups of rubber tires with their relevant natural rubber, synthesized rubber, carbon black, steel and fabric, fillers, accelerators percentages. It is observed from the table that passenger car tires consist of higher portions of synthesized rubber (27wt. %), while truck tires contain more natural rubber (27wt. %) (Rubber Manufactures Association 2010).

Compound	Passenger car tyre (wt%)	Truck tyre (wt%)
Natural rubber	14	27
Synthetic rubber	27	14
Carbon black	28	28
Steel	14–15	14–15
Fabric, fillers, accelerators, antiozonants, etc.	16–17	16–17

Table 2 chemical compositions of tires (Rubber Manufactures Association 2010).

One of the most important qualities of rubber thermal cracking is the degradation rate. It is defined as the weight percentage lost per unit time, and coordinated by the material composition of the rubber tires: Natural rubber, styrene-butadiene rubber and butyl rubber (Martínez et al. 2013). Although rubber degradation starts at 200°C when volatile compounds are highly released, the degradation behavior dependence on feedstock composition is dominant (Groves et al. 1991; Murillo et al. 2006a; Berrueco et al. 2005). This degradation rate - feedstock composition relationship was proved by a

research study (Kwon and Castaldi 2009) and it was established that polyisoprene rubber encountered a rate of 0.21 wt. % while SBR rubber met a rate of 0.25 wt. % (Kwon and Castaldi 2009). Comparing tire rubber sample with polyisoprene and SBR rubber highlights the critical aspect of rubber material effect on degradation temperature and thereby degradation rate. Therefore, it was noticed that both polyisoprene and SBR rubber materials have a degradation temperature in the range of 320-480°C, while tire rubber is in the range of 280-500°C (Kwon and Castaldi 2009). It is worth showing different degradation temperatures relevant for each component (NR, SBR and BR) in Table 3.

NR			SBR			BR			Heating rate (°C/min)
Initial	Peak	Final	Initial	Peak	Final	Initial	Peak	Final	
325	375	460	350	455	485	405	455	485	5
300	377	475	300	444	490	340	465	500	10
300	365	470	300	447	480	300	465	500	10
280	378	460	300	458	500	340	468	510	10

Table 3 Temperature for degradation of the main type compounds reported in literature (Martínez et al. 2013)

Information that put emphasis on the importance of different tire materials used on the pyrolysis products yields is abundant in literature. For instance, (Kyari et al. 2005) selected seven different brands of tires to undergo pyrolytic analysis; afterwards, the produced gas was analyzed and it was found that different gas compositions with different calorific values are produced. Furthermore, the calorific values ranged between 29.9 MJ/m³ and 42.1 MJ/m³ and the pyro-oil (liquid) showed different aromatic concentrations.

When comparing groups passenger car tires (PCT) and truck tires (TT) dissimilarity in the yield of products and their contents were observed. Results executed

by (Ucar et al. 2005) exhibited liquid yields of 47.4% and 55.6% at 550°C for PCT and TT respectively. In addition, sulfur content and aromatic content returned from PCT that contains NR of 35 wt.% are 1.35 wt.% and 41.54 vol.% respectively (Ucar et al. 2005), however, TT that contains NR of 51 wt.% had a yielded liquid content of 0.83 wt.% and 15.41 vol.% respectively.

Similarly, (Buekens 1977) analyzed the liquid yield from pyrolysis process of high content NR truck tires and found that it contains low aromatic contents.

It was found by (Roy et al. 1997) that more aromatic compounds are produced by tire pyrolysis rather than pyrolysis of pure polyisoprene (NR) due to the presence of SBR and processing oil in the former. This confides the factor of production of aromatic radical species via SBR thermal breakdown as suggested by (Kwon and Castaldi 2008). All the preceding information agree with results shown by (Lopez et al. 2009) that aromatics are produced in greater amounts in tire type rubber used as PCT (43.7 wt.%) than in tire type used as TT (33.4 wt.%). These results were gathered at a temperature of 500°C. It was emphasized that PCT was analyzed to have 29.6 wt. % NR & 29.6 wt. % SBR while TT contained 58 wt. % and 0 wt. % for NR and SBR respectively (Lopez et al. 2009). Therefore, higher amounts of aromatic hydrocarbons produced are associated with SBR cracking.

2. Temperature factor

It is described by (Martínez et al. 2013) that waste tire pyrolysis process is an endothermic reaction that needs thermal energy in order to take place. Thus, temperature is considered to be an indispensable parameter. The temperature factor is widely studied in literature by many authors; for instance, waste tire pyrolysis is considered optimal at a

temperature of 500°C at atmospheric pressure (Mastral et al. 2000b; de Marco Rodriguez et al. 2001b; Aylón et al. 2005; Murillo et al. 2006a; Aguado et al. 2005; Gieré et al. 2006; Ucar et al. 2005; Berrueco et al. 2005). (de Marco Rodriguez et al. 2001b) inspected the existence of sticky-gummy, which consists of SBR, BR and NR as pyrolytic product from pyrolysis operating at lower temperatures.

However, the existence of secondary reactions as a result of pressure, heating rate and superficial velocity of the carrier gas have big influences. Therefore, the absence of secondary reactions would make the change of temperature ineffective in changing the pyrolysis products yields (de Marco Rodriguez et al. 2001a; Roy et al. 1990; Ucar et al. 2005; Miguel et al. 1998). Table 4 shows null variation of pyrolysis product yields at different conditions.

Average product yields (wt%)			Temperature range (°C)	Type of reactor	Experimental conditions	Ref.
Gas	Liquid	Solid				
17.5 ^a	38.3 ^a	44.2 ^a	From 500 to 700	FBR	A piece of tyre of 2–3 cm (wide) pyrolysed under N ₂ at 1000 cm ³ /min and 15 °C/min	[50]
6.0	61.0 ^c	33.0	From 415 to 500	Bench scale reactor	Pyrolysis under vacuum pressure, below 3 kPa	[59]
7.6 ^a	50.7 ^{a,c}	41.7 ^a	From 550 to 800	FBR	130 g of scrap tyres pyrolyzed at 7 °C/min up to the desired temperature and hold for 1 h	[69]
8.0 ^b	58.4 ^{b,c}	33.6 ^b	From 500 to 1000	RKR ^e	Particle size < 0.42 mm. The sample (200 g) was heated at 5 °C/min up to desire temperature at 500 mL/min of N ₂	[168]
6.8 ^d	53.1	40.1				

Table 4 Pyrolysis product yields reported in literature with null effect of temperature parameter change of yields. (Martínez et al. 2013)

Any impact of temperature increase on increasing gas yield is strictly linked to the existence of secondary reactions. It is essential to note that this increase in gas yield happens at the expense of liquid yield (Chang 1996). (Chang 1996) conducted an experiment by a TG balance at 550°C with a particle size of 2mm and a carrier gas flow

of 50cm³/min. The results showed an increase of gas yield above 50 wt. % as temperature increased from 350°C to 550°C.

In Table 5 the gas, liquid and solid yields wt. % are acquired while changing temperature. Each author conducted the experiment at different conditions in various reactors.

Average product yields (wt%)			Temperature (°C)	Type of reactor	Experimental conditions and observations	Ref.
Gas	Liquid	Solid				
17.9	41.5	40.6	600	AR	Mixture of tyres from trucks, tractors and passenger cars with a particle size around 5 mm. N ₂ flow of 11.4 L _N /h	[8]
29.7	31.3	39.0	700			
31.5	27.5	41.0	800			
9.0	47.0	44.0	425	FBR	Motorcycle tyres of 4 cm ³ . The volatiles residence time was around 5 s (8 L/min of N ₂)	[51]
10.0	49.0	41.0	475			
19.0	41.0	40.0	575			
4.5	58.1	37.4	450	FBR ^b	Passenger car tyres as feedstock pyrolysed at 5 °C/min. The maximum residence time in the reactor was around 120 s	[54]
5.2	56.9	37.8	525			
8.9	53.1	38.0	600			
6.0	55.4	38.6	500	FBR	4 g of scrap tyres (passenger car tyre) were pyrolysed at 75 cm ³ /min	[56]
10.8	52.2	37.0	600			
26.7	36.6	36.7	700			
14.0	46.0	38.0	500	FBR ^a	N ₂ as a carrier gas. Similar trend using CO ₂	[104]
18.0	43.0	38.0	600			
22.0	38.0	38.0	700			
2.4	38.1	49.1	550	RKR	Pilot plant working with a light over-pressure (maximum working pressure of 300 mm w.c.); 4.8 kg/h of feeding rate and 1.4 m ³ /h of N ₂	[138]
8.2	33.0	47.4	600			
10.7	31.8	48.9	680			

Table 5 Temperature effect on pyrolysis product yields reported in literature. (Martínez et al. 2013)

The larger production of gas yield at the expense of oil fraction might face a major setback by having an increase of solid fraction as pyrolysis temperature increases. Solid formation is favored upon high temperatures due to the absorption of volatile compounds on the surface of pyrolytic char and formation of fixed carbon material. It is stated that the formation of this carbonaceous material by secondary reactions at higher heating rates is provoked in spouted bed reactors and fluidized bed reactors due to gas-solid contact (Kaminsky and Sinn 1980; Conesa et al. 1996; López et al. 2010). As a result, production of carbon material from volatile compounds increased the yield of both solids and gas. The phenomena of oil adsorption on the surface of the solids fraction was

experienced by (López et al. 2010) that used CSBR reactor operated at high temperatures. The results showed a weight percentage of 33.9% and 35.8% at 425°C and 600°C respectively. (Conesa et al. 2004) practiced an intense case in a FBR reactor with no liquid yield at all and a solids composition of pyrolytic carbon of 37 wt. % and carbonaceous solid of 25 wt. %.

Hence, the occurrence of secondary reactions, which are a function of other governing parameters, for instance, carrier gas type and flow rate, heating rate, pressure and particle size and composition, is still the main manipulator of pyrolysis yields.

In order to understand the relation between the temperature factor effect and other governing parameters, three cases are further studied.

In Figure 2 liquid, solid and gas yields show no change with the increase of temperature, there is no secondary reaction-taking place.

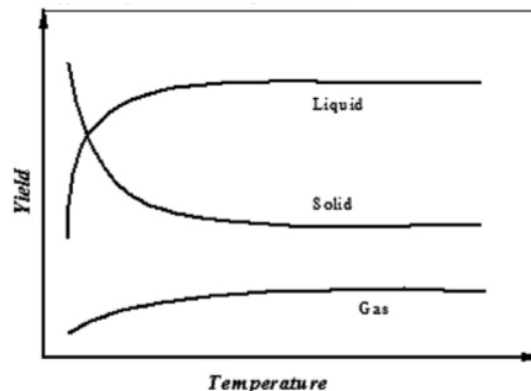


Figure 2 Constant Liquid, solid and gas (Martínez et al. 2013).

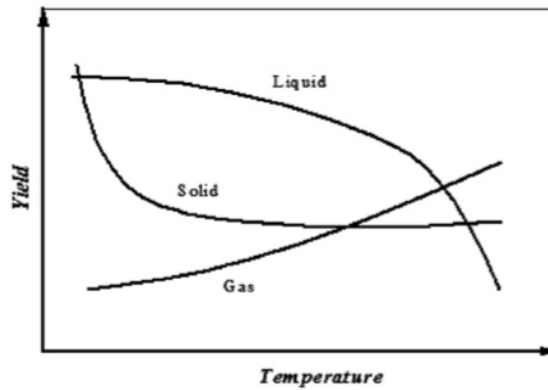


Figure 3 Liquid: decreases, Solid: constant, gas: increases (Martínez et al. 2013).

In Figure 3 gas yield increases at the expense of liquid yield that decreases in return. In addition, solid yield remained constant due to the absence of secondary reactions in solid fraction.

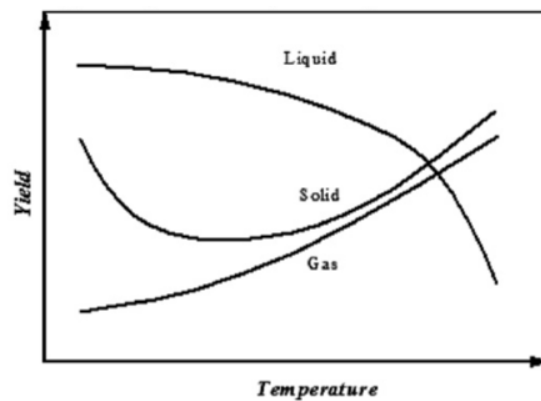


Figure 4 Solid: increase, gas: increase and liquid: decrease (Martínez et al. 2013).

Figure 4 shows a variation in all the three pyrolytic yields, such that gas portion increases while liquid fraction decreases. However, in this case, there are also secondary

reactions taking place in the solid portion of pyrolytic yields due to gas-solid contact as mentioned above.

a. Temperature effect on liquid yield

It is important to note that temperature may have a great impact on the quality of the produced pyrolytic oil. From literature, it is stated that as temperature increases, the composition of liquid fraction would alter from aliphatic compounds majority to aromatic compounds at higher temperatures (Scheirs 2006b). This result was illustrated by (Kaminsky et al. 2009), who found that the liquid fraction contained a majority of aliphatic compounds at 600°C, on the other hand, dominant aromatic compounds obtained at 700°C. At lower temperatures, it is found that olefinic acid and diolefinic hydrocarbons, which are undesirable compounds in gasoline, exist at low temperature ranges (Martínez et al. 2013).

It is important to remember that the tendency of having aromatic compounds is not only governed by temperature; but, it is linked to the existence of secondary reactions in liquid phase as well.

Some authors made their approach of having a majority of aromatic compounds by measuring the calorific values of resulted pyrolytic liquid at higher temperature values. For instance, (Li et al. 2004b) used a pilot-scale RKR reactor to find that calorific value decreased from 41.9 to 41.0 MJ/Kg when temperature changed from 450°C to 600°C.

b. Temperature effect on gas fraction

Testing two important aspects of gas fraction, which are the yield and the composition, emphasizes the effect of temperature on gas fraction. Similar to the liquid yield, the variation of gas yield production and composition results from the existence of secondary reactions such as thermal cracking (Martínez et al. 2013). Several authors that held pyrolysis tests by changing the operating temperature values stress this parameter effect. The common proposal recognized by the results is the change of simpler compounds such as hydrogen and methane gases with respect to other more complex hydrocarbons and thereby different gaseous composition and calorific values.

Some authors found that both complex compounds, for instance, CO₂, C₂H₆, C₃H₆, C₄H₆, C₄ hydrocarbons and C₅ and C₆, and calorific value decreases as temperature increases (Diez et al. 2004). Furthermore, they also stated that simpler hydrocarbons would occupy larger portion in the gas yield instead of the more dense ones. In addition, the total yield of the gas portion increases as the temperature increases. Similarly, (Napoli et al. 1997) experienced an increase in the yield of the gas as temperature increased from 380°C to 550°C. It was also discovered that carbon dioxide increased between 380°C and 450°C, while it decreased from 450°C to 550°C. Note that the major constitutes of gas yield at 550°C are CH₄ and H₂ (Napoli et al. 1997). (Galvagno et al. 2002) also confirmed these results by showing that the calorific value increased from 22 MJ/m³ to 29 MJ/m³ as temperature increased from 550°C to 680°C.

Hydrogen and methane gases have calorific values of 12.75 MJ/m³ and 39.72 MJ/m³ respectively. Therefore, according to literature, the occurrence of secondary reactions on cyclisation and hydro aromatic reactions will lead to significant CH₄, C₂, and C₃ in comparison with H₂ that will in return lead to increase calorific value of gas fraction.

In addition, CO₂ and CO concentration increases by decarboxylation and decarbonization and pyrolytic CB secondary reactions as the temperature increases from 400°C to 700°C (González et al. 2001). Both (González et al. 2001) and (Berrueco et al. 2005) confirmed the increase of calorific values due to temperature increase.

Concerning gas yield, it is found that its value increases from 20 to 29 wt. % as the temperature increases from 350°C to 550°C (Diez et al. 2004). Also, it was found that gas yield increases from 6.3wt% to 37.1 wt. % as temperature increases from 600°C to 800°C (Conesa et al. 1996).

In conclusion, temperature accompanied with secondary reactions is the main governing parameter effecting both gas yield quality and yield.

c. Temperature factor on solid fraction

As observed in Figure 2 and 3, the solid fraction is constant as temperature increases, which is classified as case I and II.

In some other cases, char (solid) fraction is considered to decrease while the temperature increases. For example, (Williams et al. 1990) testified that gasification phenomena would occur under an inert medium by which hydrocarbons constituents of char fraction might crack into more volatile chains. These results were acquired while temperature increased from 420°C to 720°C at different heating rates of 5, 20, 40 and 80°C/*min*.

However, in other cases, solid yield of pyrolysis might increase as the pyrolytic temperature increases. For instance, this case is similar to one displayed in Figure 4 takes place as a result of secondary reactions as char formation (López et al. 2010; Conesa et al. 1996; Kaminsky et al. 2009).

In the previous section it was discussed that both gas yield and composition were altered as a function of temperature and other parameters as well. Likewise, the composition variation of solid fraction is not a function of temperature only, however, tire composition and occurrence of secondary reactions can alter its quality as well. Concerning the latter one, it was confirmed by (Ucar et al. 2005) that the two types; PCT and TT showed different ash content. As a result, there was a variation in the calorific values by which PCT and TT got 34 MJ/kg and 15 MJ/kg respectively at 550°C, 650°C and 800°C (Ucar et al. 2005). In addition, it was shown that calorific value of the solid fraction decreased from 27.9 MJ/kg to 27.0 MJ/kg as temperature increased from 550°C to 700°C using FBR reactor (González et al. 2001). In a similar manner, (Li et al. 2004b) also showed a decrease in the calorific value as temperature increased from 450°C to 650°C using RKR.

In addition to the composition characteristic of char, temperature governing parameter effect on physical properties of solid fraction such as surface area and pores sizes is a debate among researchers. Some have reported that there is no influence upon increasing the temperature on both surface area and pores sizes (Fernández et al. 2012). The pyrolytic carbon black got a constant mesoporous aspect (2-50nm) and a constant change in the BET surface area, which was 68m²/g and 61m²/g at 550°C and 900°C respectively.

On the other hand, other researchers reported that temperature would increase the surface area of the CB from 46.5 m²/g at 425°C to 116.3 m²/g at 600°C in (López et al. 2010).

3. *Particle Size*

Particle size is another important governing parameter affecting pyrolysis conversion yield and composition. Similar to temperature, the particle size is function of other restraints such as heating rate, volatiles residence time and pyrolysis reaction time. Accordingly, some authors included the reverse effect of particle size on gas and oil yield, however, some others involved other behaviors such as the occurrences of secondary reactions. Concerning the latter effect, (Bouvier et al. 1987) emphasized that both particle size and pyrolysis conversion are inversely related. In addition, (Dai et al. 2001) encountered a higher conversion in a CFBR reactor at 500°C and a decrease in the pyrolytic CB from 45 wt. % to 30 wt. % with particle size of 0.8mm and 0.32 mm respectively. Furthermore, gas and liquid fractions were lower for 0.8mm. These results were confirmed by (Barbooti et al. 2004), who reported an increase in liquid yield as particle size decreases. This relation between pyrolysis yields and particle size is based on various explanations. Some researchers, for instance, (Beaumont and Schwob 1984) identified the existence of temperature gradient upon pyrolysis of large particles due to heating flux resistance. Such behavior would induce a heat transfer limitation and thus pyrolysis is held at a lower temperature. Therefore, size limitation would impose a main obstacle for heat transfer to reach the bulk structure of large particles (Barbooti et al. 2004).

As mentioned above regarding particle size limitation on heat transfer, there is a direct relation between particle size and pyrolysis time. For instance, Oyedun et al. (Oyedun et al. 2012) combined a heat transfer model with a kinetic model to find that at 500°C and 5°C/*min*, particles having radius of 10mm and 50mm had durations of 1.5h

and 2.5h respectively. Increasing the heating rate to 10°C/min decreased the pyrolysis time to 0.8h and 1.9h respectively.

Analogous to all governing parameters effecting pyrolysis, the particle size is strongly linked with the presence of secondary reactions. Islam et al. (Islam et al. 2008) found a decrease in liquid yield for the smaller particles of 2 cm³ compared to 4 cm³ sizes. Moreover, CB fraction increased for 2 cm³ particles. This behavior, opposite to the expectations concluded concerning the particle size- yield relation, is explained by the formation of secondary reactions which is presented by quick devolatilisation (Islam et al. 2008).

4. Carrier gas flow rate:

As it is mentioned above, the pyrolysis process is a thermal cracking mechanism that occurs in the absence of oxygen. This can be achieved by either vacuum system or in an inert gas medium, for instance, argon or nitrogen.

The gas flow rate contributes directly to the residence time of the gas phase inside the reactor. From fluid mechanics, there is a direct relation between the flow rate and the superficial velocity; as the flow rate increases, the superficial gas velocity increases too and therefore, the volatiles residence time will decrease.

Consequently, at higher flow rates, vapors produced are removed fast without giving them the chance to undergo secondary reactions represented by recondensation, repolymerization, char formation and further cracking (Williams et al. 1990; González et al. 2001).

This phenomenon was investigated by (Islam et al. 2008) and noticed that, the gas yield increased at the expense of both liquid and char yields at a low carrier gas flow

rate. Further cracking in the liquid fraction by secondary reactions took place. In addition, (Cunliffe and Williams 1998) stated that they experienced a higher liquid yield as the carrier gas flow rate increased which prevented secondary reactions, represented by char formation, to take place.

G. Catalysis

Catalytic pyrolysis can be conducted in the presence of heterogeneous catalysts in order to induce further polymer cracking. Any additional cracking achieved by catalysts will increase the non-condensable part of the volatile portion of the rubber and this is represented by additional gas yield. Many types of catalysts are utilized with different selectivities to certain products. In this work, only acidic catalysts and photoactive semi-conductors are discussed.

1. Acidic Catalysts

Zeolites are a class of acidic solid catalysts. They are oxide metals made up of crystalline alumina-silicates within a microporous structure (Ertl et al. 1997). Zeolite catalysts have crystalline structure that contains cages and channels, where cations, absorbed water or any other molecules are captured. Zeolites have an old history and were discovered in 1756 by Axel Frederick Cronstedt who is a Swedish mineralogist. The synthesis of zeolites passed through many stages before it invaded worldwide laboratories. The chemist Richard Barrer was first to study zeolite synthesis in 1930's and succeeded in synthesizing the first zeolite in 1948. On the other hand, there is natural zeolite derived from natural minerals, such as mordenite, silicalite, faujasite and ferrierite.

It is clear that the names of natural zeolites reflect the name of the minerals that they are made up of. (Chorkendorff and Niemantsverdriet 2003)

A famous type of synthetic zeolite, which is named according to the place that developed it, is ZSM zeolite. It stands for Zeolite Socony Mobil contributing to the Socony Mobil Company.

Zeolites are oxide metals made up of silica and alumina building units surrounded by oxygen atoms at the corner. The framework consists of SiO_4 and AlO_4 tetrahedra in different configurations to build a crystalline structure as shown in Figure 5 (Chorkendorff and Niemantsverdriet 2003).

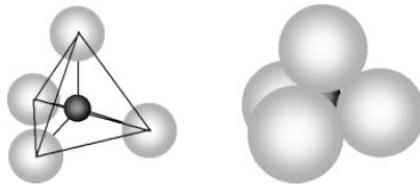


Figure 5 SiO_4 tetrahedra building unit for zeolite (Chorkendorff and Niemantsverdriet 2003)

These tetrahedral units are arranged in different architectures that produce different silicate units having four, six, eight or twelve membered rings. These building blocks bind together in a periodic structure to form a zeolite structure. Different types of zeolites with their relevant pore size and volume together with Si/Al ratio are displayed in Table 6.

Common name	3-letter code	Channels	Window or channel diameter (nm)	Pore volume (mL g ⁻¹)	Si/Al
Zeolite A	LTA	3D, Cages connected by windows, cubic	0.45	0.30	1
Zeolite X	FAU	3D, Cages connected by windows, tetragonal	0.75	0.35	1–1.5
Zeolite Y	FAU	3D, Cages connected by windows, tetragonal	0.75	0.35	≥2.5
Mordenite	MOR	1D, two straight, parallel channels	0.70; 0.65	0.20	≥5
Zeolite L	LTL	1D, one straight channel			
ZSM-5	MFI	2D, one straight, one sinusoidal, mutually perpendicular channels	0.55	0.15	≥10
Zeolite Beta	BEA	3D, two straight, one sinusoidal, perpendicular channels	0.76; 0.64	0.25	≥5

Table 6 Zeolite types composition and geometry

Zeolites have distinct structures regarding their arrangement; for instance, Beta zeolites (BEA) have superimposed porous channels. The reacting molecules will pass through the pore channels and windows, where they will react with the surface protons H⁺ and exit as new species. Zeolite beta is a rare example of an aluminosilicates with a helical pore structure. It is an intergrowth of two distinct but closely related structures, i.e., polymorphs A and B that have fully three dimensional pore systems with 12-rings. Both structures can be described based on different stacking of the same sheet component. **Figure 6** shows zeolite beta framework and channel structure.

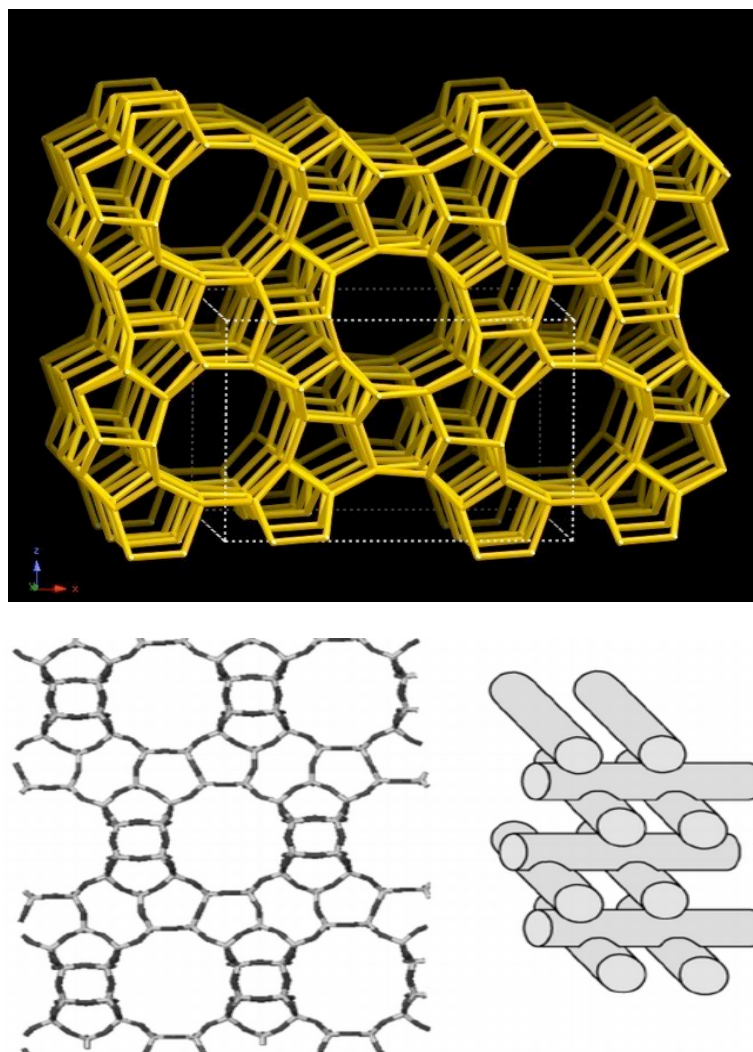


Figure 6 Hbeta zeolite framework and pore structure.

The H-type zeolite catalyst is considered to be acidic surface either having Bronsted acid property sites or Lewis acid sites. The former is due to protons attached on the oxygen atom forming -OH groups. This case occurs when an aluminum cation (Al^{3+}) replaces a silica cation (Si^{4+}) in tetrahedra structure shown in Figure 5 (Chorkendorff and Niemantsverdriet 2003). In a framework silicon tetrahedra (T position) Si has 4^+ charge connected with the coordinating oxygen atoms having 2^- charge which leads the unit to

have a neutral formal charge ($\text{SiO}_{4/2}$). However, upon replacement of Si with Al having 3^+ , the formal charge will alter from 0 to -1 ($\text{AlO}_{4/2}^-$) (Cejka et al. 2010). Therefore, in order to compensate the net charge formed, a positive cation either sodium (Na^+) or hydrogen proton (H^+) is needed to neutralize the charge. In the case of a hydrogen proton, the zeolite will be in the form of H-X where X is the zeolite type e.g. ZSM or Beta. This is known to be a Bronsted Acid site having a hydrogen proton that has a tendency to be donated. Figure 7 shows that the zeolite surface will develop a gigantic polyacid structure (Chorkendorff and Niemantsverdriet 2003). These weakly bonded hydroxyl protons located on oxygen bridges connecting tetrahedrally coordinated silicon and aluminum form Bronsted acid sites responsible for the zeolite high catalytic activity (Cejka et al. 2010).

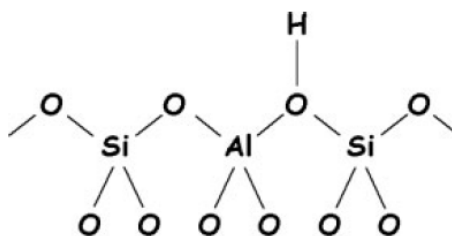


Figure 7 Bronsted Acid site of zeolite (Chorkendorff and Niemantsverdriet 2003)

In some cases, the tetrahedra position aluminum atom can be replaced by other metal such as Fe or Ga to have the form of SiOHT , where T is the replaced metal. Both, the type of the substituted metal and the bond angle of the bridge, affect the acidity strength of the bridging hydroxyl protons. In addition, the global composition framework of a zeolite has an important role influencing the acidity strength. In other words, for a

zeolite to have a higher acidic strength it should have higher mean electronegativity, therefore, lowering the existence of Al atoms (Cejka et al. 2010). Another approach is discussed in literature says that upon increasing Al atoms, hydroxyl protons will increase representing the acidic sites, however, a phenomena called proton crowding due to many Bronsted Acid sites will weaken the acidic strength.

Hydroxyl groups may occur in different manner than bridged ones due to different treatment methods. For instance, silanol groups or hydroxyl groups at extra frame aluminum atoms may form as shown in Figure 8.

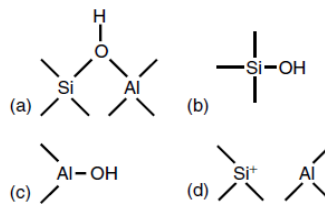


Figure 8 Examples of hydroxyl groups in zeolites (Cejka et al. 2010)

On the other hand, Lewis acid sites are formed by strong heat treatment with high temperatures above 773K. This high temperature will lead to dehydroxylation of Bronsted acid sites and formation of Lewis acid sites. In other cases, Lewis acid sites are due to extra-framework aluminum species of octa-, penta-, or tetrahedral coordination as a result of dealumination (Cejka et al. 2010). It was proposed by Scherzer et al. that AlO^+ , $Al(OH)_2^+$ and $Al(OH)$ are considered as extra-framework aluminum species in the dealuminated zeolites (Maher et al. 1971). Kuehl confirmed that $[AlO^+]$ units migrated

from zeolite framework to be cationic extra-framework species that are known to be as true Lewis acid sites (Kühl 1999; Kühl 1977).

In addition, Lewis acid sites on the extra-framework of a zeolite are located on silicon species that are positively charged in the neighborhood of tri-coordinated aluminum atoms. The tri-coordinated positively charged extra-framework silicon species have the tendency to receive electron pair and act as strong Lewis acid sites (Cejka et al. 2010). These frameworks are derived by dehydroxylation route suggested by (Gonzales et al. 1997) as shown in Figure 9.

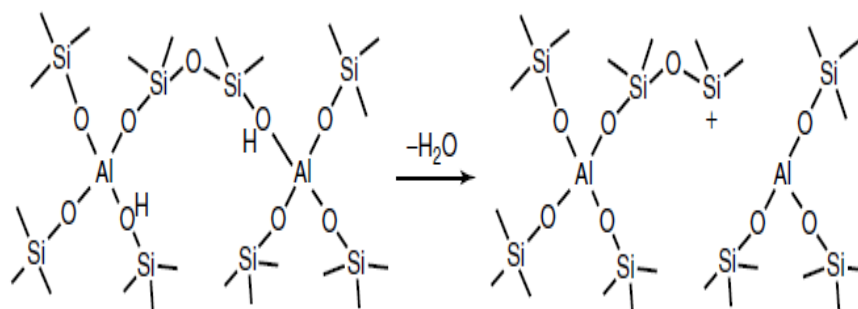
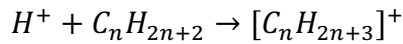


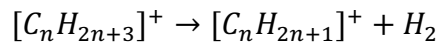
Figure 9 Formation of Lewis Acid by dehydroxylation of zeolite (Cejka et al. 2010)

The most famous industrial usage of zeolite as acid catalyst in industry is in Fluidized Catalytic Cracking known as FCC. In this unit, catalytic reactions take place to convert heavier fractions from refinery processes, for instance vacuum gas and residues, to produce middle distillates (Von Ballmoos et al. 1997). It is important to note that the catalytic cracking reactions taking place involve the existence of carbonium and carbenium ion intermediates (Chorkendorff and Niemantsverdriet 2003).

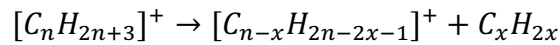
The carbonium ions are generated from alkenes in the initial protonation step,



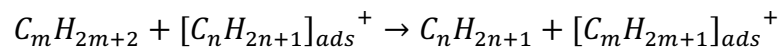
Since the carbonium ion is considered to be chemically unstable, then it is converted into carbenium ion as follows:



Meanwhile, the cracking step occurs as:



Other hydrocarbons participate in the reaction by the adsorbed carbenium ion:



In some cases, acid catalysts are altered into bifunctional catalysts in order to adjust the catalytic reactions provoked by the heterogeneous catalysts. For instance, platinum can be doped onto the zeolite in order to enhance the reforming of some hydrocarbons that are involved in the reaction. Platinum atoms can be added into the acidic surface in order to help with the reforming of straight chain alkanes and alkenes into branched and aromatic hydrocarbons (Ertl et al. 1997). It was widely reported in literature the dividing role of catalysis between acid supports and doped metal sites. The acidic sites are known to conduct both isomerization and cracking of large hydrocarbons, whereas, the metallic sites perform dehydrogenation, hydrogenation and, to some extent,

aromatization. Furthermore, cyclic hydrocarbons occur under optimal temperatures of 500°C and pressures of 5-20 bars (Chorkendorff and Niemantsverdriet 2003).

Bi-functional catalysts are used in hydrocracking units in the oil industry. These catalysts have dual functional ability dehydrogenation/ hydrogenation and acidic cracking (Cejka et al. 2010). Table 7 shows the list of different metals that can be added on different supports in their relevant hydrogenation and acidity.

	Hydrogenation function	Acidic function (support)	
Increasing	↓ Ni/Mo	Al ₂ O ₃	↓ Increasing
Hydrogenation	Ni/W	Al ₂ O ₃ /halogen	Acidity
Power	Pt/Pd	SiO ₂ /Al ₂ O ₃ Zeolites	
	(low-S conditions)		

Table 7 Metals/ acidic supported catalysts (Chorkendorff and Niemantsverdriet 2003)

2. Photoactive Catalysts

Volatile organic compounds (VOC) cause water and air pollution, particularly indoor pollution. Emissions of VOCs contribute to localized pollution problems of toxicity and odor. VOCs are involved in the depletion of ozone layer and probably lead to global warming (Kim and Hong 2002). These issues made it considerable to develop technologies for VOCs treatment. One of the most promising upcoming technologies is photocatalytic oxidation. Nevertheless, treatment of VOCs via decomposition by photocatalysts has been difficult due to low conversion and common deactivation of the

catalysts (Alberici et al. 2001; Zhang et al. 2004; Wang et al. 2005a; Marci et al. 2003; Zhang 2003). As a result, methods should be implemented to prolong catalyst life and enhance its photocatalytic activity.

There are many techniques for modification of TiO₂-based photo catalysts (Kim et al. 2005), including preparation as nano-sized particles (Maira et al. 2001) and the incorporation of transition (Litter 1999) or noble metals (Kennedy and Datye 1998; Vorontsov et al. 1999). Results have showed that the modification of TiO₂-based catalysts with metals improves the performance of photocatalytic oxidation/reduction of different organic chemicals (Tada et al. 2004; Sun et al. 2005; Hosseini et al. 2007). The interaction between metal and semiconductor creates an electron transport across the Schottky barrier from the support to the metal. This will contribute to a reduction reaction on the metal surface and prevents hole-electron recombination (Einaga et al. 2001).

Many reasons are behind making titanium dioxide as one of the most important semiconductors used. For instance, this white solid substance is known to be environmentally friendly, abundant, non-toxic, economical and versatile (Chen et al. 2010a; Kudo and Miseki 2009a; Fujishima et al. 2000; Ochiai and Fujishima 2012; Bak et al. 2002).

Historically, titanium dioxide formed the basis of applied photocatalysis under the influence of light. In 1972, Fujishima (Fujishima 1972) used n-type TiO₂ semiconductor along with UV light to perform the first successful photocatalytic water splitting experiment. In addition, hydrogen production from water splitting (Ni et al. 2007; Chen and Mao 2007a; Maeda 2011) emphasizes the importance of TiO₂ semiconductor in the sector of alternative green energy.

From literature, it is important to show that this unique performance of TiO₂ is a function of its morphological properties, crystallinity, size, and surface chemistry (Liu et al. 2014a). TiO₂ photocatalytic distinct activity is highly dependent on acquiring light waves and therefore, its optical structure is a crucial specification (Liu et al. 2014a). Therefore, this contribution of TiO₂ characteristics, in the molecular structure, on its performance pushed researchers through further structural and surface modification strategies (Wen et al. 2015a).

The heterogeneous photoactive TiO₂ catalyst relies on the occurrence of redox reactions that take place on its surface (Hu et al. 2009). Furthermore, such reactions need a suitable electronic structure and thermodynamic condition in order to be stimulated (Liu et al. 2014a; Ma et al. 2014). The molecular structure of TiO₂ forms the basis of its unique thermodynamic property, by which the band structure including the band gap and positions of both valence band (VB) and conduction band (CB) provoke light absorption capability and thus catalyst redox ability (Ma et al. 2014).

This phenomenon is true along with many typical photocatalytic processes, such as water splitting, degradation of pollutants, selective organic transformations, and CO₂ reduction for fuel generation (Wen et al. 2015a). Figure 10 shows the same logic behind the electrochemistry-taking place on TiO₂ photo catalyst surface.

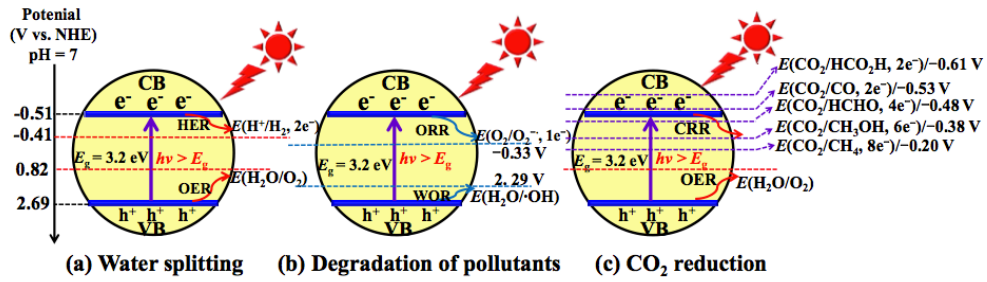
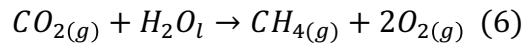
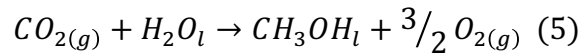
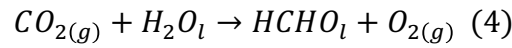
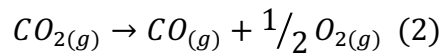
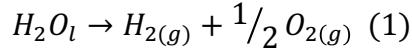


Figure 10 Similar electrochemistry for different photocatalytic processes (Wen et al. 2015a)

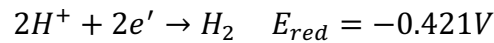
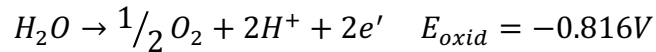
As shown in Figure 10, photocatalysis relies on light acquired from many sources, whether solar or any other source. The absorbed light must provide minimum energy equal to the energy gap between VB and CB, which is 3.2 eV. Its wavelength is calculated to be $\lambda \leq \frac{hc}{E_g} = \frac{1240}{3.2} = 387.5 \text{ nm}$ (Pasternak and Paz 2013). As a result, it is observed that due to the absorption of light electrons will be therefore transferred from valence band to reach conduction band leaving behind positive (electron acceptor) vacant sites (Pasternak and Paz 2013). Eventually, electrons arriving on the conduction band will induce a reduction half reaction, whilst the left positive holes denoted by h^+ will trigger an oxidation half reaction (Pasternak and Paz 2013).

Figure 10 (a) and (c), illustrate an oxidation reaction with a transfer of adsorbed water into oxygen by means of positively charged holes on the valence band. Similarly, in Figure 10 (b) water can be oxidized on the valence band to give hydroxyl radicals considered as reactive compounds in the degradation of contaminants (Pasternak and Paz 2013). Meanwhile, the photo generated electrons, which have left the valence band and settled on the conduction band induce reduction half reaction. For instance, reduction reactions include the reduction of O_2 to super oxides, hydrogen production and CO_2 (Pasternak and Paz 2013).

In order to understand the thermodynamic nature of redox reactions taking place on a photo catalyst, it is essential to identify the Gibbs free energy of the half-cell reactions. It was reported by Li X et al. (2014) that both water splitting and CO₂ reduction reactions are as follows:



From Figure 10 it is identified that the oxidation of H₂O into O₂ (H₂O/O₂) has a potential of -0.816V, while the reduction of H⁺ to H₂ is at -0.421V. The two half reactions are as follows:



Generally, the half-cell having the highest negative potential is reversed (to be oxidation) such that the total cell potential, $E_{cell} = E_{oxid} + E_{red}$, becomes positive. A compound with the more positive potential will oxidize the reduced form of a substance of lower (more negative) potential. As a result, the Gibbs free energy

$$\Delta G = -nfE_{cell}$$

will be negative. It is known that negative Gibbs free energy implies that the reaction is thermodynamically favorable. However, in the case of water splitting reaction, the total cell potential is $E_{cell} = -0.816 - 0.421 = -1.237V$, which will imply a positive Gibbs free energy, ΔG , which is thermodynamically an unfavorable uphill process (Wen et al. 2015a).

All the mentioned reactions do not take place spontaneously at ambient temperature, unless a catalyst such as TiO_2 is utilized. Kudo A et al. (2009) confirmed that organic oxidation of O_2 is thermodynamically favored (Kudo and Miseki 2009b). The conduction band, where the photo generated electrons are located, will serve as oxidation source (donates e^-) and the intended reaction (reduction) will be reduced by gaining this e^- . Subsequently, reduction reaction of H^+/H_2 in the water splitting reaction in Figure 10 (a) takes place by pairing the conduction band half-cell and the reaction H^+/H_2 as follows:

$$E_{CB (red)} = -0.51V$$

$$E_{H^+/H_2 (red)} = -0.41V$$

The potential value of the CB is reversed to be $+0.51V$ since it is oxidation half-cell is emitting an electron, while the H^+/H_2 reduction potential is kept at $-0.41V$. The total cell potential is then obtained at,

$$E_{cell (spontaneously induced)} = +0.1V$$

And the Gibbs free energy is negative.

However, for CO_2 reductions there are two reactions showed in Figure 10 (c) that are not favored. Even in the presence of TiO_2 photo catalyst on the conduction band having the

potential of $E_{CB, red}$ is $-0.51V$. The first reaction is reduction of CO_2/CO , which has a reduction potential of $E_{red}=-0.61V$. The conduction band potential is reversed because it is oxidized, i.e. $E_{CB}=+0.51V$. Thus, the total cell potential $E_{cell}=+0.51-0.61=-0.1V<0$, which is non-spontaneous reaction. The second reaction is reduction of CO_2/HCO_2H , which has a reduction potential of $E_{red}= -0.53V$. After reversing the conduction band potential and summing up with the reduction potential, the overall cell potential will be $E_{cell}= +0.51-0.53 = -0.02V <0$ that is still non-spontaneous reaction.

Similar logic can also be applied for the valence band where positive holes (h^+) are located. Concerning the oxidation reaction of H_2O/O_2 having a potential of $E_{red}=+0.82V$ and a valence band having a potential of $E_{VB, red}= 2.69V$. The half reaction potential for water oxidation is reversed since it is given in reduction value to be $E_{oxid}= -0.82V$, while the valence band potential is kept as it is since it will undergo reduction (electron acceptor). Therefore the total cell potential will be $E_{cell}=+2.69-0.82= +1.87V$ and thus a negative Gibbs free energy is obtained which indicates a spontaneous reaction when semiconductor TiO_2 is used.

These analysis are confirmed by Park H. et al. (2013) by reporting that CB energy level $E_{CB}=-0.51V$ is more negative than reduction potential of oxygen O_2/O^{2-} having $E_{red}= -0.33V$ (Park et al. 2013). In addition, the valence band energy level $E_{VB}=+2.29V$ is more positive than oxidation potential of H_2O , $E_{red}=+2.29V$ (to be reversed). This will prove that positively charged holes at the valence band are capable of oxidizing organic substances as well as water (Chen et al. 2010b).

a. Charge carriers

The photocatalytic activity of TiO₂ as a photo catalyst is not only related to the favorable thermodynamics properties. Many limitations that present some setbacks in the catalytic activity include recombination and light harvesting.

The photocatalytic phenomenon takes place by following certain footprints:

- Light harvesting
- Charge generation
- Charge separation
- Surface reactions which are known as oxidation and reduction reactions.

Therefore the overall efficiency of the photo catalyst is expressed by the following formula

$$\eta_c = \eta_{abs} \times \eta_{sc} \times \eta_{cmt} \times \eta_{cu}$$

η_{sc} is the solar energy conversion efficiency.

η_{abs} is the light absorption efficiency.

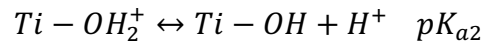
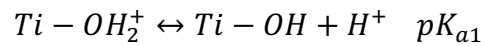
η_{cmt} is the charge migration and transport efficiency.

η_{cu} is the charge usage efficiency for photo catalysis reactions.

The efficiency of the catalyst is a function light absorption, solar energy conversion, charge migration and transport, and charge usage of photocatalyst reactions (Wen et al. 2015a).

b. Surface chemistry factor

The TiO₂ photo catalyst redox reactions take place on the catalyst surface, therefore catalyst activity is highly influenced by surface chemistry of titanium dioxide. Surface charge, a surface chemistry property, affects the photocatalytic efficiency due to the acid-base reactions occurring at the shell of TiO₂ (Park et al. 2013).



From these acid-base equilibrium reactions an important property can be calculated, which is known as zero point of charge that controls the surface charge of the catalyst:

$$pH_{zpc} = 1/2 (pK_{a1} + pK_{a2})$$

Zero point of charge is linked to the pH value at zero net proton charge in which no charge (positive) is being transferred. Measuring the zeta potential identifies the isoelectric point of suspended particles at different pH values (Wen et al. 2015a).

Zeta potential of TiO₂ powder is manipulated by the dielectric constant ϵ of the solvent where TiO₂ is dissolved in. This direct effect of altering the Zeta potential by solvent reveals strong electrostatic interaction between TiO₂ and the corresponding solvent (Wen et al. 2015a). The relation between these two parameters is clearly displayed in the following correlation:

$$ZP = 13.43 - 213.63/\epsilon$$

Thus, when TiO₂ powder is dissolved in a solvent with high dielectric constant, then it will have higher zeta potential value.

Another important specification under the surface chemistry description of the TiO₂ photo catalyst is the high hydrophilicity. This specification is elaborated by the ability of the titanium dioxide to harvest UV light and emits photo generated electrons which will alters the Ti⁴⁺ into Ti³⁺ state. Meanwhile, oxygen vacancies will be created due to positively charged holes. The resulted oxygen vacancies will act as attractive sites for water molecules that would be altered into adsorbed hydroxyl radicals (OH) in return. This will increase the surface hydrophilicity (Fujishima 1972; Liu et al. 2014b; Wang et al. 1998; Sakai et al. 2003). Both mechanisms are shown in Figure 11.

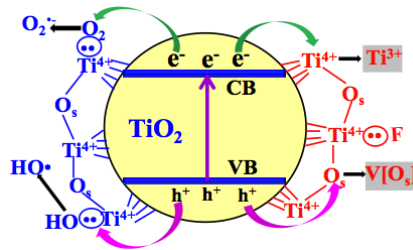


Figure 11 Surface chemistry reactions (Wen et al. 2015a)

In addition, changing the density of adsorbed hydroxyl groups can alter TiO₂ surface chemistry, which is accomplished by replacing the surface -OH groups (Lv et al. 2012; Wang et al. 2005b; Carneiro et al. 2011) at high calcination temperature (Yu et al. 2002; Yu et al. 2003b; Yu et al. 2003c). It was reported that the surface hydroxyl groups could be exchanged by sulfate ions (SO₄²⁻) through sulfuric acid (H₂SO₄) treatment. These sulfate ions will substitute the surface OH- groups at high temperatures and form a Bronsted Acid surface trait. Consequently, the photocatalytic activity will be enhanced and charge recombination will be suppressed at the same time (Lv et al. 2012; Wang et al. 2005b; Carneiro et al. 2011), as shown in Figure 12. Several examples were discussed

about the enhancement of photo activity by acidic treatment; for instance, oxidation of acetone in air was significantly improved (Jimmy et al. 2002). In addition, CH_3Br oxidation was enhanced with acidic treatment of TiO_2 by 2 folds in comparison with untreated TiO_2 catalyst (Wang et al. 2005c).

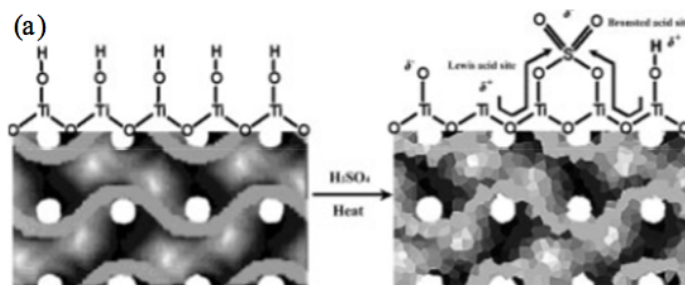


Figure 12 Acidic surface formations by sulfate ions on Titanium surface (Wang et al. 2005c)

Two outcomes for increasing the calcination temperature values: either crystallization of TiO_2 or OH groups number per TiO_2 particle increase. As a result, the photocatalytic activity of titanium dioxide would dramatically increase (Carneiro et al. 2011; Lv et al. 2011; Fan et al. 2012). On the other hand, calcination temperature elevation might result with some setbacks by decreasing the activity due to rutile formation and sintering growth of TiO_2 crystallites, which will decrease the surface area of TiO_2 (Yu et al. 2002; Yu et al. 2003a; Yu et al. 2003c; Zhou et al. 2008).

It is stated that the surrounding medium will have a great impact on the surface chemistry of the catalyst. For instance, if TiO_2 is surrounded by weak alkaline medium, there will be a huge generation of hydroxyl radicals that are considered to be very reactive compounds for organic compounds degradation (Wen et al. 2015a).

H. ENERGY ECONOMICS

According to (Daugaard and Brown 2003), pyrolysis energy demand is considered to be the heat of enthalpy due to the change from room temperature up to the pyrolysis operating temperature which is called sensible heat energy. Add to this, the phase change energy and the required reaction energies to achieve cracking of the hydrocarbons.

This energy demand can be supplied either from a separate source (e.g., auxiliary fuel, electric heating, etc.) or by burning the produced gas or the obtained solid fraction (Martínez et al. 2013).

From thermodynamics point of view, a pyrolysis process is a combination of endothermic and exothermic reactions taking place simultaneously (Collins et al. 1974; Cheung et al. 2011). Reactions that are categorized as exothermic take place initially prior to the endothermic reactions that are represented by vaporization phenomena (Yang and Roy 1996). In other words, the initial cracking reactions are considered highly exothermic to form the products that will undergo further secondary cracking reactions by endothermic vaporization (Cheung et al. 2011). The energy demands for pyrolysis are influenced mostly by endothermic pyrolysis reactions.

An important aspect that should be emphasized is that the waste tire pyrolysis process is dominated by endothermic reactions in addition to the energy needed to produce feedstock components; synthetic rubber, natural rubber and carbon black (Laird et al. 2009). However, regardless of all other demands, reaction pyrolysis (endothermic or volatilization) is considered the most demanding (Gomez et al. 2009). An expected energy recovery efficiency of 75-82% is calculated by performing a net energy balance on the process (US Department of Energy Report 1983).

Energy assessments and calorific energy values were reported by several authors. For instance, (Aguado et al. 2005) estimated a reaction enthalpy energy demand of 267.6 kJ/kg. In addition, (Cheung et al. 2011) calculated a reaction enthalpy of 646 kJ/kg at 20°C/min and at 510°C. Furthermore, (Yang and Roy 1996) mentioned that Natural Rubber and Synthetic Rubber volatilization reaction by a temperature raise from 30 to 510°C had an enthalpy change of 870 kJ/kg and 550 kJ/kg, respectively. On the other hand, the heat generation from a waste tire is, on average, 33MJ/kg (G. Ferrer, The economics of Tire Remanufacturing 2011).

Pyrolysis reaction is discretized into thermodynamic phases relevant to sequential temperature intervals. Pyrolysis complex process is a combination of endothermic and exothermic reactions.

Temperature was elevated from 25°C to 590°C, where sensible and latent heat energies take place to the rubber material pieces and rubber products as well. The thermodynamics is divided as follows:

Between 25°C & 300°C:

Sensible heat takes place to the rubber materials before starting primary reactions.

Between 300°C & 450°C:

Heat of reaction takes place representing the exothermic energy emitted from bond breaking of polymers constituting the rubber material.

Between 450°C & 510°C:

Heat of vaporization endothermic energy takes place due to the start of phase change of pyrolytic products representing the secondary reactions and further cracking.

Between 510°C & 590°C:

Sensible heat occurs for the present pyrolytic gases and carbonaceous solids produced (see Appendix A.1).

I. ENVIRONMENTAL ASPECTS

From an environmental perspective, pyrolysis has always been a great interest for researchers. Several authors asserted that waste tire pyrolysis is considered to be a cleaner process in comparison with other thermal processes such as incineration (Aylón et al. 2010; Galvagno et al. 2002; Aylón et al. 2005; Murillo et al. 2006a). This is due to fewer emissions to the environment in addition to the ability of recovery of solid and liquid from the material that the feedstock is made up of. Consequently, the pyrolysis products can be utilized in further applications as new fuel products. Another advantage of waste tire pyrolysis is that there are fewer amounts of gases produced in comparison with combustion (Sinn et al. 1976). Therefore, less gas cleaning systems are needed.

Concerning air emissions quality, hazardous traces such as dioxins, dibenzofurans and thermal NO_x are largely minimized during pyrolysis (Malkow 2004). This was confirmed by (Bennett 1993), who stated that there is no such emissions from pyrolysis units. The main basis for less toxic Dioxins and Furans is the absence of oxygen during the process, which prevents the probability of partial oxidation of the rubber feedstock (Lloyd 2006). However, minor VOC emissions due to leakage of pipe joints, shafts and pumps are not uncommon (Lloyd 2006).

CO₂ gas emissions are considered as one of the most important critical points in pyrolysis processes. According to the International Energy Agency (2009) (International Energy Agency 2009), less CO₂ emissions per unit of energy are produced from the utilization of pyrolysis products in comparison with direct combustion of waste tire. This is due to the existence of fossil originated carbon black in the char portion (International Energy Agency 2009). Table 8 shows a comparison between CO₂ emissions of waste tire

pyrolysis and of other fossil fuels used in power generation (International Energy Agency 2009).

Fuel	gCO₂/kW h	Times
Crude oil	353.76	2.59
Gas/Diesel oil	266.64	1.95
LPG	227.04	1.66
Anthracite	353.76	2.59
Coking coal	340.56	2.49
Sub-bituminous coal	345.84	2.53
Lignite	364.32	2.67
Peat	381.48	2.79
Natural gas	201.96	1.48
Volatiles released in WT pyrolysis	136.51	1.00

Table 8 CO₂ emissions from combustion of fossil fuels and volatiles released in waste tire pyrolysis (International Energy Agency 2009)

PAH's (Polycyclic Aromatic Hydrocarbons) are aromatic compounds produced due to the interaction of solids products during the combustion of coal, tobacco, oil, gasoline and other fossil fuels. It is important to investigate the quantities of PAH's released during waste tire pyrolysis. In fact, less PAH's emissions are registered during waste tire pyrolysis due to the absence of solids in the produced volatile fraction. According to (Herlan 1978), PAHs are prone to deposition as unburnt fractions if found in small amounts in a particular fuel. In the waste tire pyrolysis case, since carbon black solids are removed then there would be less PAHs emissions.

During pyrolysis, the separation of inorganic hazardous elements, such as sulfur and zinc is not a serious issue in comparison to other waste processing techniques. In fact, most sulfur quantities contained in the rubber tire feedstock are deposited in the solid

fraction product (70%), while the rest is divided between gas and liquid fractions, which will therefore have low sulfur contents (Rezaiyan and Cheremisinoff 2005; Unapumnuk et al. 2008). Regarding zinc, the pyrolysis temperature is considered too low for volatilizing zinc which has a high boiling point of 901°C (Conesa et al. 2004).

To sum it up, from economic and environmental point of views, rubber tire pyrolysis is considered a feasible waste minimization technology if markets for the obtained products are made available. (Murillo et al. 2006b) stated that the economic sustainability of waste pyrolysis is directly related to the possible usage of the three products (solid, liquid and gas). Hence, waste rubber pyrolysis products' composition and yield should be improved and optimized by utilizing new techniques, for instance, inclusion of heterogeneous catalysts in order to alter the composition of components in the derived fuels.

J. RESEARCH OBJECTIVE

Pyrolysis products' yields and composition are highly dependent on operating conditions and the type of the reactor used. Nevertheless, it is clear that the gas yield wt. % has always been the lowest among the three products. It is noticed that pyrolytic oil is considered to be a dirty oil since it is rich in complex aromatics, which are difficult to be directly utilized in further applications. Hence, the aim of this research is to optimize the pyrolytic gas yield at the expense of oil yield by developing active novel catalysts. Ultimately, this should result in a cleaner pyrolytic oil with simpler hydrocarbons, i.e. smaller carbon number. Active heterogeneous catalysts should be designed with the ability to withstand harsh operating conditions and deactivation.

On the other hand, the application of solar energy is exploited for the catalytic pyrolysis to maximize the process energy efficiency and completely cut its dependence on fossil fuel or auxiliary electrical energy. Photo catalysts will be designed to maximize gas yield and improve liquid product composition.

CHAPTER III

METHODOLOGY

Several steps will be executed simultaneously and in parallel to help achieve the research objectives. These include,

- Experimental setups for thermal and solar pyrolysis will be prepared and operated under inert gas.
- Suitable catalysts will be designed to enable further cracking of condensable compounds and therefore, it is expected to increase the yield of the gas fraction (non-condensable).
- Catalyst synthesis will focus on two types; acidic and photoactive catalysts. In addition, the catalyst surface should be very reactive to complex long chain sticky hydrocarbon compounds.
- Catalyst behavior can be predicted by implementing several characterization techniques. For instance, an important factor is the surface area of the synthesized catalysts measured using the BET isotherm method in addition to both pore size and volume.
- Furthermore, SEM, EDX and XRD techniques will be carried out in order to investigate the surface morphology, structure and composition.
- The produced fuels yields will be calculated, and pyrolytic oil compositions analyzed using the GC-MS equipment.

Both solar and thermal pyrolysis experiments will be conducted with different synthesized catalysts and catalyst to rubber ratios to determine the most active synthesized heterogeneous catalyst.

CHAPTER IV

CATALYST PREPARATION

Several catalysts were synthesized in this work having different support material either acidic or semi-conductor material. Different active metals can be doped on the support surface to enhance catalytic activity in addition to change some specifications. Therefore, two supports were synthesized; titanium dioxide and H-B Zeolite. Afterwards, both supports were incapacitated with noble metals, palladium, platinum and bismuth. Catalyst synthesis was done following different procedures depending on the metal type and the combination used. This section is divided into two main parts and according to the type of support used.

A. Synthesis Methods

1. Hbeta zeolite Support

Hbeta zeolite is a well-known acidic heterogeneous catalyst used in the industry. It has been under intensive research in the past decades. As mentioned earlier it possesses Bronsted acid and Lewis acid framework characteristics. Our scope is to utilize this acidic catalyst in order to crack pyrolytic products and increase gas yield. The zeolite catalytic performance can be enhanced even more via doping with noble metals to induce additional reaction mechanisms.

Throughout this research, Hbeta zeolite was used as a catalyst, in addition, to doping with palladium and/or platinum noble metals.

a. Hbeta zeolite preparation

i. Materials

Silica dioxide (Aerosil 2000, fumed, silica content: 99.8%, particle: 0.014 μ m, surface area: 200m²/gram) was purchased from Sigma Aldrich. Concerning the alumina source, aluminum isopropoxide (220418-1 KG,>98%) was purchased from Sigma Aldrich. Tetraethyl ammonium hydroxide TEAOH (40% in water, 86633-100mL) is purchased from Sigma Aldrich.

ii. Procedure

H-B Zeolite (synthesized) was synthesized by preparation of zeolite precursor. 4.1 grams of SiO₂ were weighed and placed in a small beaker. 14.4 grams of TEAOH solution 25wt. % was prepared from 40wt. % TEAOH solution and then poured on SiO₂ in the beaker while mixing. See **Appendix A.1** for sample calculations. In addition, 0.3 grams of aluminum isopropoxide was added. Afterwards, 3.6 grams of deionized water is then added over the mixture under continuous stirring at room temperature for 2 hours. The composition of the prepared zeolite precursor has a molar ratio of 96.53SiO₂: 34.55TEAOH: 1.0Al₂O₃: 1130H₂O (Li et al. 2009).

Afterwards, hydrothermal synthesis process is applied for the prepared zeolite precursor by pouring the precursor solution in the stainless steel Teflon crucibles that were tightly closed. Crystallization of the zeolite was done in an oven furnace at 155 degrees for 3 days. After crystallization, a filtration apparatus filtered the sample while washing it until the pH dropped below a value of 8 (Li et al. 2009). The sample was then dried at 120 degrees for 12 hours and calcined at 550 degrees for 8 hours (Li et al. 2009). The crystallization process is conducted for not less than three days. A strict temperature

with suitable crystallization time would result in a perfect zeolite structure at the surface (Li et al. 2009).

b. Pd (0.25wt. %) / Hb zeolite

i. Materials

Palladium active metal was obtained from palladium nitrate hydrate Pd (NO₃)₂.xH₂O (Sigma Aldrich). The zeolite support surface is composed of alumina and silica materials. SiO₂ (Aerosil 2000, fumed, silica content: 99.8%, particle: 0.014um, surface area: 200m²/gram) and aluminum isopropoxide (>98%) was purchased from Sigma Aldrich. Tetraethyl ammonium hydroxide TEOH (40% in water) is purchased from Sigma Aldrich.

ii. Procedure

Pd (0.25%wt.)-Hbeta Zeolite was prepared by physical mixing of palladium with SiO₂, (25%wt) TEOH solution and deionized water under strong mixing. Same procedure is then followed as H-B Zeolite preparation. Crystallization was performed in furnace in the same manner with hydrothermal procedure followed by drying at 120 degrees for 12 hours and calcination at 550 degrees for 8 hours (Li et al. 2009).

c. Pt (0.25wt. %) / Hb zeolite

i. Materials

The platinum source of active noble metal is from potassium tetrachloroplatinate K₂PtCl₄ (Sigma Aldrich).

The zeolite support that consists of Silica and Alumina that are supplied from SiO₂ (Sigma Aldrich, Aerosil 200, fumed, Silica content: 99.8%, particle: 0.014um, surface area: 200m²/gram) and aluminum isopropoxide (Sigma Aldrich, Inc., KG>98%). In addition, TEAOH (tetraethyl ammonium hydroxide (Sigma Aldrich, 40% in water).

ii. Procedure

Pt (0.25%wt.)-H-B Zeolite was prepared by physical mixing of platinum with SiO₂, (25%wt) TEAOH solution, aluminum isopropoxide solution and deionized water under strong mixing. Same procedure is then followed as H-B Zeolite preparation. Crystallization was performed in furnace in the same manner with hydrothermal procedure followed by drying at 120 degrees for 12 hours and calcination at 550 degrees for 8 hours (Li et al. 2009).

d. Pt (0.5mol%)-Pd (0.5mol %) /Hb zeolite

i. Materials

This catalyst is considered having bimetallic active sites based on zeolite support. The two active noble metals platinum and palladium are derived from potassium tetra-chloroplatinate K₂PtCl₄ (Sigma Aldrich) and palladium nitrate hydrate Pd (NO₃)₂. xH₂O (Sigma Aldrich) respectively. In addition, SiO₂ (Sigma Aldrich, Aerosil 200, fumed, Silica content: 99.8%, particle: 0.014um, surface area: 200m²/gram), aluminum isopropoxide (Sigma Aldrich, Inc., >98%) and TEAOH (tetraethyl ammonium hydroxide (Sigma Aldrich, 40% in water) are the chemicals used to synthesize the zeolite support surface.

ii. Procedure

Pt (0.5% mol.)-Pd (0.5% mol.)/H-B Zeolite was prepared by physical mixing of platinum and palladium precursors with SiO₂, (25%wt), aluminum isopropoxide solution, and TEAOH solution and deionized water under strong mixing. Same procedure is then followed as H-B Zeolite preparation. Crystallization was performed in furnace in the same manner with hydrothermal procedure followed by drying at 120 degrees for 12 hours and calcination at 550 degrees for 8 hours (Li et al. 2009).

2. *Titanium dioxide Support*

Titanium oxide is a well-known semi-conductor powder used as catalyst in many environmental applications. This white powder is considered as mentioned in our literature review as a photoactive catalyst that relies on light harvesting to gather energy from either UV light or visible light. In this experimental work, we synthesized 3 types of noble metals doped on titanium oxide surfaces in order to investigate to which extent photo activity can be enhanced.

a. Pd (0.25wt. %) /TiO₂

i. Materials

Palladium nitrate hydrate Pd (NO₃)₂. xH₂O (Sigma Aldrich) is used as Palladium source for active metal. Semi-conductor titanium dioxide TiO₂ source was derived from pure anatase TiO₂ purchased from Sigma Aldrich.

ii. Procedure

Palladium based on titanium dioxide heterogeneous catalyst is prepared by wet impregnation method.

Palladium nitrate $\text{Pd}(\text{NO}_3)_2 \cdot x\text{H}_2\text{O}$ was added to deionized water in a small beaker and stirred well to have palladium nitrate solution. Meanwhile, pure anatase TiO_2 was mixed with small amount of distilled water just to be able to mix with the impregnated palladium precursor. Afterwards, both solutions were mixed together under heated stirring to evaporate water. The cake is calcined at 723K (425 degrees) for 2 hours. Stoichiometric calculations are shown in Appendix.1

b. Pt (0.25wt. %) /TiO₂

i. Materials

Potassium tetrachloroplatinate K_2PtCl_4 (Sigma Aldrich) is used as Platinum noble metal source for catalyst synthesis. The semi-conductor titanium dioxide source used is pure anatase.

ii. Procedure

The heterogeneous catalyst consisting of active metal platinum based on TiO_2 support is synthesized by pore impregnation method. Potassium tetrachloroplatinate K_2PtCl_4 is added to deionized water in a small beaker and stirred well to have potassium tetrachloroplatinate solution. At the same time, pure anatase TiO_2 is mixed with distilled water as well. Afterwards, both solutions are mixed together under heated stirring to evaporate water and get rid of spectator ions. The cake acquired is calcined at 723K for 2 hours (see stoichiometric calculations in Appendix A.1)

c. Pt (0.5mol%)-Pd (0.5mol %) /TiO₂

i. Materials

Potassium tetrachloroplatinate solid chunks K₂PtCl₄ (Sigma Aldrich) and palladium chloride PdCl₂ solution (Sigma Aldrich, form: liquid, 5wt. % in 10wt. % HCL) are used as platinum and palladium metals sources respectively. Regarding the semiconductor TiO₂, titanium (IV) isopropoxide (TIP). (Sigma Aldrich, form; liquid, 97% purity) was used. In addition, ethanol is used for the isopropoxide solution.

ii. Procedure

Pt-Pd/TiO₂ catalyst is prepared by sol-gel method. Titanium (IV) Isopropoxide (TIP) is added to ethanol in a beaker while stirring for 5 minutes at 500 rpm. After that, deionized water of 5.71cm³ is added at a rate of 0.5cm³/min to the alkoxide solution in the beaker. At this point, a white thick precipitation was formed. It was then peptized for 2 hours to have a clear solution. A specific amount of K₂PtCl₄ is added into the solution followed by addition of PdCl₂ solution. Then, mixing is done for a duration of 2 hours in order to homogenize to solution. The solutions are then placed in the centrifuge at 2000 rpm for 5 minutes. The obtained heavy cake part is dried at 70 degrees for 48 hours before calcining at 450 degrees for 3 hours. See Appendix A.1 for calculations.

d. SiO₂ (5wt. %) /TiO₂/ Bi₂O₃ (5wt. %)

i. Materials

Silica dioxide (Aerosil 2000, fumed, silica content: 99.8%, particle: 0.014 μ m, surface area: 200m²/gram) was purchased from Sigma Aldrich. Bismuth (III) nitrate pentahydrate (Sigma Aldrich, reagent grade 98%,). Titanium oxide semi-conductor prepared by Titanium (IV) oxysulfate (Sigma Aldrich, > 29% Ti (as TiO₂) basis, technical, form: Solid powder). Ammonium hydroxide solution ~ 25% (Sigma Aldrich, 30501-2.5L, form: liquid).

ii. Procedure

A certain amount of TiOSO₄ is dissolved in deionized water to have an aqueous solution. Meanwhile, silica dioxide was weighed and placed in a beaker and stirred with distilled water. Afterwards, a specific amount of bismuth nitrate hydrate was prepared in order to be mixed with SiO₂ precursor. Finally, the prepared mixture is added to titanium oxysulfate. While mixing at 300 rpm, concentrated ammonia hydroxide was added dropwise in order to adjust the pH at a value of 10. Mixing is done for a duration of 5 hours at a temperature of 70°C. The produced cake is rinsed with deionized water and then sent for drying at 100°C for 3 hours followed by calcination at a temperature of 600°C for 3 hours.

B. Synthesis Stoichiometric Calculations

1. *Hb zeolite support*

a. Hb zeolite

Sample calculation for synthesized H-B Zeolite catalyst

We need to mix 14.4 grams of 25%wt. TEAOH.

$$m_{TEAOH} = \frac{25}{100} \times 14.4 = 3.6 \text{ grams pure TEAOH}$$

$$m_{H_2O} = 10.8 \text{ grams}$$

Available TEAOH:

To get 3.6 grams of TEAPH from a 40% *bottle* then;

$$m_{solution} \times \frac{40}{100} = 3.6 \text{ grams}$$

$$m_{solution} = \frac{3.6}{0.40} = 9 \text{ grams}$$

So from 9 grams of TEAOH (40%) solution we got 3.6 grams of TEAOH and 5.4 grams of water.

To reach a weight fraction of 25%, we added water until we have a total mass of 14.4 grams, by which 5.4 grams of water is added to the solution.

b. Pd (0.25wt. %) / Hb zeolite

The active metal palladium represents 0.25wt. % of the total powder solids used in the support.

$$\frac{0.25}{100} \times 4.4 = 0.011 \text{ grams Pd}$$

$$M_{Pd(NO_3)_2 \cdot xH_2O} = 230.43 \text{ gmol}^{-1}$$

$$n_{Pd} = \frac{0.011}{M_{Pd}} = \frac{0.011}{106.42} = 1.03364 \times 10^{-4} \text{ moles}$$

Therefore,

$$n_{Pd(NO_3)_2 \cdot xH_2O} = 1.03364 \times 10^{-4} \text{ moles}$$

Thus,

$$m_{Pd(NO_3)_2 \cdot xH_2O} = 1.03364 \times 10^{-4} \text{ moles} \times 230.43 \text{ gmol}^{-1} = 0.023818 \text{ grams}$$

c. Pt (0.25wt. %) / Hb zeolite

The active metal platinum represents 0.25wt. % of the total powder solids used in the zeolite support.

Platinum source: K_2PtCl_4

$$\frac{0.25}{100} \times 4.4 = 0.011 \text{ grams Pt}$$

$$M_{K_2PtCl_4} = 415.09 \text{ gmol}^{-1}$$

$$M_{Pt} = 195.09 \text{ gmol}^{-1}$$

$$n_{Pt} = \frac{0.011}{195.09} = 5.6384 \times 10^{-5} \text{ moles}$$

$$n_{Pt} = n_{K_2PtCl_4} = 5.6384 \times 10^{-5} \text{ moles}$$

$$m_{K_2PtCl_4} = 5.6384 \times 10^{-5} \text{ moles} \times 415.99 \text{ gmol}^{-1} = 0.0234045 \text{ grams}$$

d. Pt (0.5mol%)-Pd (0.5mol %) /Hb zeolite

This catalyst can be written in weight % because weight of powder solids used in zeolite is known instead of molecular mass. Therefore, Pt (0.66wt. %)-Pd (1.2106wt. %) / H-B (synthesized).

Mass of total powder

$$m_{SiO_2} = 4.1 \text{ grams}$$

$$m_{((CH_3)_2CHO)_3Al} = 0.3 \text{ grams}$$

$$m_{total} = 4.4 \text{ grams}$$

Platinum source: K_2PtCl_4

$$\frac{0.66}{100} \times 4.4 = 0.02904 \text{ grams Pt}$$

$$M_{K_2PtCl_4} = 415.09 \text{ gmol}^{-1}$$

$$M_{Pt} = 195.09 \text{ gmol}^{-1}$$

$$n_{Pt} = \frac{0.02904}{195.09} = 1.4885 \times 10^{-4} \text{ moles}$$

$$n_{Pt} = n_{K_2PtCl_4} = 1.4885 \times 10^{-4} \text{ moles}$$

$$m_{K_2PtCl_4} = 1.4885 \times 10^{-4} \times 415.09 = 0.0617879 \text{ grams}$$

Palladium source: $Pd(NO_3)_2 \cdot xH_2O$

$$m_{Pd} = \frac{1.2106}{100} \times 4.4 = 0.0532664 \text{ grams}$$

$$M_{Pd} = 106.42 \text{ gmol}^{-1}$$

$$M_{Pd(NO_3)_2 \cdot xH_2O} = 230.43 \text{ gmol}^{-1}$$

$$n_{Pd} = \frac{0.0532664}{106.42} = 5.0053 \times 10^{-4} \text{ moles}$$

$$n_{Pd(NO_3)_2 \cdot xH_2O} = n_{Pd} = 5.0053 \times 10^{-4} \text{ moles}$$

$$m_{Pd(NO_3)_2 \cdot xH_2O} = 5.0053 \times 10^{-4} \times 230.43 = 0.115337 \text{ grams}$$

2. *Titanium dioxide Support*

a. Pd (0.25wt. %) /TiO₂

Sample calculation for monometallic on TiO₂ semi-conductor catalyst

$$m_{sample} = 5 \text{ grams}$$

$$m_{Pd} = \frac{0.25}{100} \times 5 \text{ grams} = 0.0125 \text{ grams}$$

$$n_{Pd} = \frac{0.0125}{106.42} = 1.17459 \times 10^{-4} \text{ mols}$$

Then,

$$n_{Pd(NO_3)_2} = 1.17459 \times 10^{-4} \text{ mols}$$

Therefore,

$$m_{Pd(NO_3)_2 \cdot xH_2O} = 1.17459 \times 10^{-4} \times 230.43 = 0.027066 \text{ grams}$$

Rest of the sample:

$$m_{TiO_2} = 5 - 0.0125 = 4.9875 \text{ grams}$$

b. Pt (0.25wt. %) /TiO₂

Sample calculation for monometallic on TiO₂ semi-conductor catalyst

$$m_{\text{sample}} = 5 \text{ grams}$$

$$m_{\text{Pt}} = \frac{0.25}{100} \times 5 \text{ grams} = 0.0125 \text{ grams}$$

$$n_{\text{Pt}} = \frac{0.0125 \text{ grams}}{195.09 \text{ g} \cdot \text{mol}^{-1}} = 6.40729 \times 10^{-5} \text{ mols}$$

Then,

$$n_{\text{K}_2\text{PtCl}_4} = n_{\text{Pt}} = 6.40729 \times 10^{-5} \text{ mols}$$

Therefore,

$$m_{\text{K}_2\text{PtCl}_4} = 6.40729 \times 10^{-5} \text{ mol} \times 415.09 \text{ g/mol} = 0.026596 \text{ grams}$$

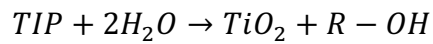
Rest of the sample:

$$m_{\text{TiO}_2} = 5 - 0.0125 = 4.9875 \text{ grams}$$

c. Pt (0.5mol%)-Pd (0.5mol %) /TiO₂

Bimetallic noble metals supported on semi-conductor TiO₂ catalyst calculations

as follows:



$$n_{\text{TIP}} = n_{\text{TiO}_2} = 1$$

Let $m_{\text{TiO}_2} = 5 \text{ grams}$

But $M_{\text{TiO}_2} = 79.87 \text{ g} \cdot \text{mol}^{-1}$

Then

$$n_{\text{TiO}_2} = 0.062601 \text{ moles}$$

Now, $M_{TIP} = 284.22 \text{ g.mol}^{-1}$

$$m_{TIP} = 0.062601 \text{ moles} \times 284.22 \text{ g.mol}^{-1} = 17.792 \text{ grams}$$

Now, $\frac{n_{H_2O}}{n_{TIP}} = 12$

Therefore,

$$n_{H_2O} = 0.7512 \text{ moles} \rightarrow 13.529 \text{ grams}$$

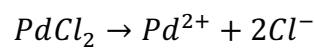
Titanium dioxide consists of 99 mole% of the total catalyst sample:

$$n_{total \text{ catalyst}} = \frac{0.062601}{0.99} = 0.0632323 \text{ moles.}$$

0.5 mol% metals:

$$n_{Pt} = n_{Pd} = 3.1616 \times 10^{-4} \text{ moles}$$

Palladium source:



$$n_{PdCl_2} = n_{Pd} = 3.1616 \times 10^{-4} \text{ moles}$$

$$M_{PdCl_2} = 177.33 \text{ gmol}^{-1}$$

$$m_{PdCl_2} = 0.056064 \text{ grams}$$

But solution of $PdCl_2$ is:

5wt. % $PdCl_2$

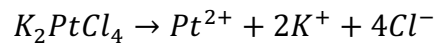
10wt. % HCl

85wt. % H₂O

Therefore, we should use:

$$m_{\text{solution}} = \frac{0.056064}{0.05} = 1.12133 \text{ grams PdCl}_2 \text{ solution}$$

Platinum source:



$$n_{Pt} = n_{K_2PtCl_4} = 1 = 3.1616 \times 10^{-4} \text{ moles}$$

$$M_{K_2PtCl_4} = 415.09 \text{ gmol}^{-1}$$

$$m_{K_2PtCl_4} = 0.131239 \text{ grams}$$

d. SiO₂ (5wt. %) / TiO₂ / Bi₂O₃ (5wt. %)

The preparation of a heterogeneous catalyst made up of three components goes as follows

Source of SiO₂ is fumed silica:

$$M_{SiO_2} = 60.08$$

Silica dioxide represent 5% wt, of the total sample,

$$m_{\text{sample}} = 5 \text{ grams}$$

Then,

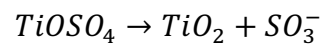
$$m_{SiO_2} = \frac{5}{100} \times 5 = 0.25 \text{ grams}$$

Bismuth constitute of 2.5% wt. of the total catalyst sample,

$$m_{Bi_2O_3} = \frac{2.5}{100} \times 5 = 0.125 \text{ grams}$$

$$m_{TiO_2} = 5 - (0.25 + 0.125) = 4.625 \text{ grams}$$

Mass needed of titanium oxysulfate



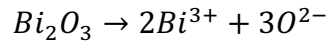
$$\frac{n_{TiOSO_4}}{1} = \frac{n_{TiO_2}}{1}$$

$$n_{TiO_2} = 0.0579 \text{ moles} = n_{TiOSO_4}$$

Therefore,

$$m_{TiOSO_4} = 0.0579 \text{ moles} \times 159.92 = 9.2608 \text{ grams}$$

As for the bismuth source:



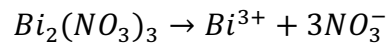
$$\frac{n_{Bi_2O_3}}{1} = \frac{n_{Bi^{3+}}}{2}$$

$$n_{Bi_2O_3} = 2.682 \times 10^{-4} \text{ moles}$$

Then,

$$n_{Bi^{3+}} = 2(2.682 \times 10^{-4}) = 5.3652 \times 10^{-4} \text{ moles}$$

Source of bismuth is $Bi(NO_3)_3$



$$n_{Bi(NO_3)_3} = n_{Bi^{3+}} = 5.3652 \times 10^{-4} \text{ moles}$$

$$m_{Bi(NO_3)_3} = 5.3652 \times 10^{-4} \times 465.96 = 0.2603 \text{ grams}$$

$$m_{Bi(NO_3)_3} = 0.2603 \text{ grams}$$

CHAPTER V

EXPERIMENTAL

A. Thermal Pyrolysis

An electrical furnace with a model number: OTF-1200X-R-II shown in Figure 13 is used as a heater for thermal catalytic pyrolysis experiments. The electrical furnace has a temperature controller that enables the selection of specific heating rate segments and a certain steady temperature for a preselected duration of time.



Figure 13 Electric furnace unit

Inside the furnace there are two adjacent heating compartments that are controlled separately by two similar temperature controllers. Figure 14 shows the experimental setup of the furnace where a large quartz cylinder is placed coaxially inside the circular heating sections.



Figure 14 Thermal furnace heating compartments

Figure 15 shows the quartz tube reactor, having an inner diameter of 0.7 cm and a length of 120 cm, which is placed inside the large quartz cylinder.

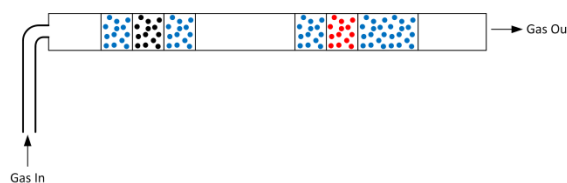


Figure 15 Fixed bed reactor (FBR): rubber pieces (black), cotton glass (blue), and catalyst (red)

Thermal pyrolysis runs were conducted with the 9 synthesized catalysts at fixed carrier gas and operating temperature. Carrier gases used was nitrogen inert gas; it was supplied from gas bottles and through small rubber tubes connected to the inlet of the reactor quartz tube. The outlet was connected to another tube that is taking the effluent gases to the snorkel.

Several runs were done using different catalysts. The rubber pieces and the catalyst used were placed at the inlet side of the carrier gas (left heating compartment) and the outlet part (right heating compartment) respectively. The two positions were separated by a fixed distance and each material (catalyst & rubber) was surrounded by cotton glass as shown in Figure 15. The outlet part of the quartz tube was filled with cotton in order to collect the condensable part of the volatile compounds flowing with the carrier gas. In addition to that, the wet tissue was placed at the end part of the quartz tube in order to cool it down so that the pyrolytic oil would condensate.

The two furnace compartments were set at a temperature of 640°C (inside reactor temperature of 590°C), which is the outer temperature (between the insulation and the quartz cylinder). The controller was given a ramp time of 10 minutes to reach the set point. The second segment given for the controller was time duration of 30 minutes at an isothermal temperature of 640°C.

During the furnace start-up phase, the small diameter quartz tube reactor was placed in a way that the rubber pieces on the first half distance were outside the furnace, while the catalyst half was inside. The catalyst was given time duration of 20 minutes at high temperature accompanied with UV light of radiations in order to be extremely active. After the catalyst activation stage, the quartz tube reactor was pushed into the furnace so that the rubber pieces part and the catalyst were at the center of the first and second heating sections respectively; the tube was placed inside for a pyrolysis time for 15 minutes. Gas flow was fixed at a constant rate of 0.0572 l/min by the help of a pressure regulator connected to the gas bottle.

B. Solar Pyrolysis

The solar unit is the same unit used by (Zeaiter et al. 2015) to reach high-temperatures by concentrating solar radiations with a Fresnel lens integrated with an automated system that tracks the sun. The solar system, which is shown in Figure 16, has a Fresnel lens fixed on a wooden frame (91cm high and 69cm wide with a focal length of 66 cm); the Fresnel lens can withstand high temperatures up to 977 °C.

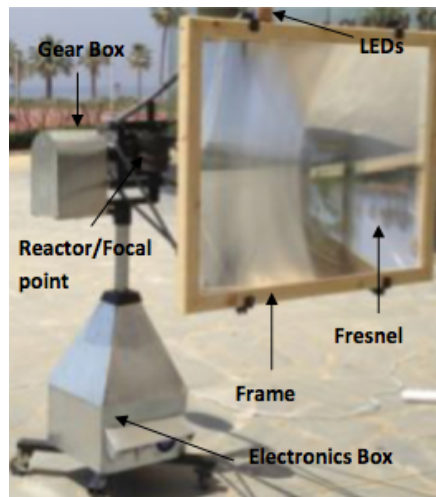


Figure 16 Automated solar unit (Zeaiter et al. 2015)

In solar pyrolysis experiments, the same configuration of fixed bed reactor is used as the one used in the thermal pyrolysis shown in Figure 15 , however, a smaller quartz tube is utilized instead of the long quartz tube. For all types of used catalysts, the same procedure is followed for placing the catalyst powder and shredded rubber pieces in the catalytic fixed bed reactor. First of all, a quantity of shredded rubber pieces (2mm

average) is inserted in the quartz tube reactor and held with cotton glass on both sides, while the catalyst lies at a distance of approximately 5 cm from the rubber charge.

Afterwards, the reactor is placed at the focal point of the solar unit and purged with slightly pressurized nitrogen. A small beaker of water was used to check the flow of carrier gas during the process of “catalyst activation”. This process is kept for 15 minutes elapsed time under a temperature approximated at 550-570 °C in order to activate the catalyst at high temperatures. Hukseflux L1-19 pyrometer was used to determine the solar irradiation of the sun during the experiment. A Thermocouple was used to determine the temperature at the focal point of the solar irradiation at the reactor position.

Shredded rubber pieces are weighed according to a certain ratio with the catalyst weight for each run test and placed in the quartz reactor.

Once the “catalyst activation” stage was done the quartz reactor was displaced such that the rubber position is exactly under the focal point of radiation. At this point, the “Pyrolysis” test was being started with a constant gas flow rate of 0.02862 l/min. Each reaction test run lasted for 15 minutes at a temperature ranging between 550-570 °C and irradiation intensity ranging between 950-1100W/m².

C. Gas Yield Calculation

After each thermal pyrolysis run, the quartz reactor was weighed using a weighing balance in order to infer the quantity of the non-condensable gas produced.

$$\Delta m = m_{\text{reactor before pyrolysis}} - m_{\text{reactor after pyrolysis}}$$

$$\% \text{ Gas Yield} = \frac{\Delta m}{m_{\text{added rubber}}} \times 100$$

CHAPTER VI

CATALYST CHARACTERIZATION

Characterization of the heterogeneous catalysts is considered to be one of the most important catalysis subjects. The characterization of a catalyst enables researchers and industrial designers to visualize several important properties of any catalyst before being utilized. In other words, characterization gives the ability to predict the behavior of the newly designed catalyst. Several techniques are considered during characterization such as BET isotherm analysis, SEM, EDX, and XRD. In general, a good catalyst is considered to have a high surface area with extended pores. In the case of a heterogeneous catalyst, the catalytic reaction takes place at the solid-gas interface, therefore a catalyst with a bigger surface area is expected to have higher catalytic conversion rate. Furthermore, a heterogeneous catalyst has a porous rough surface which is a critical property that influences catalytic activity. Some catalysts have fine pores by which the surface of these pores provides the area needed for a high reaction rate whereas others have large pores. Hence, the variety of pore sizes and lengths would affect the composition of the generated products (Fogler 1999).

A. BET Isotherm

In order to identify the surface area of synthesized and commercial catalysts used throughout the pyrolysis experiments, BET analysis is executed to determine the monolayer area per gram of the catalyst surface in addition to the pore size and volume. Catalyst samples were placed in the calibrated BET quartz cells and exposed to degassing

prior to BET analysis. The aim of degassing is to get rid of all the undesired volatiles and organic compounds that might be stuck on the catalyst surface and the BET cell walls. Afterwards, the cells containing are placed in the analysis column, and the BET adsorption-desorption steps start to take place while the cells are immersed in liquid nitrogen to maintain low temperature of 75K. The outcomes of BET isotherm analysis are the single point and multi-point surface areas accompanied with the pore size and the volume of the catalyst. In addition to that, BET analysis gives the isotherm adsorption / desorption both related to the coverage proportion versus P/P_0 data during pressurizing and vacuuming with nitrogen gas.

The most common isotherm type is known to be type II isotherm shown in Figure 17. It can be seen that a sub-monolayer will start forming up to pressure values at point B. From this point, the plateau part of the curve represents the formation of the monolayer, and beyond the plateau, there will be an uncontrolled formation of capillary condensation when all pores are filled with gas (Chorkendorff and Niemantsverdriet 2003).

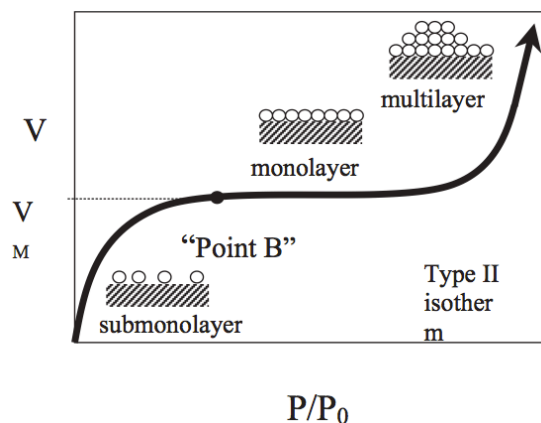


Figure 17 Type II BET isotherm (Chorkendorff and Niemantsverdriet 2003)

B. XRD Analysis

X-Ray diffraction (XRD) is a technique that relies on the scattering of x-ray emissions by the atoms that makeup a solid compound (catalyst in our case). This phenomenon enables us to determine the lattice structure of the catalyst and the arrangement of the framework.

The analysis results of XRD tests show the intensity of x-ray diffraction at certain diffraction angles (2Θ); these peaks would give an image about the lattice arrangement and phase identification. From the pattern of the diffraction angles, we can form an idea about the miller indices of crystal geometry e.g. cubic, tetragonal and orthorhombic.

An XRD analysis is performed at a specific incident x-ray wavelength lambda (λ).

C. SEM Analysis

Scanning electron microscopy is a technique that uses an electron beam released by an electron gun. A primary electron beam is sent to the surface of the sample and thus generating several beams of backscattered electrons, secondary electrons in addition to X-rays, photons, and diffracted electrons that are slightly off-angle from the primary beam. SEM has an X-ray detector and an electron detector that enable it to quantify the yield of the backscattered and secondary electrons as a function of beam's position. Backscattered electrons are due to deeper parts of the sample, which give information about the composition of the sample. The secondary electrons that originate from the surface of the sample are due to low energies (5-50eV) (Chorkendorff and Niemantsverdriet 2003).

It is important to note that some areas in the SEM image are expected to be brighter than other regions; this is due to orientation of the surface, because the bright parts are the ones facing the detector (Chorkendorff and Niemantsverdriet 2003).

We performed SEM imaging for all the synthesized catalysts in order to see if the morphology complies with the ones mentioned in literature.

D. EDX Analysis

This method of characterization is done using the same facility of the SEM; this machine involves an additional detector (other than the electron detector), which is the X-ray detector. Therefore, it is known as Energy Dispersive X-ray. The emitted X-rays represent a relevant identification of the elements where the point is under analysis; this would give the chemical composition of any selected point or region under analysis (Chorkendorff and Niemantsverdriet 2003).

CHAPTER VII

RESULTS AND DISCUSSION

A. Characterization

1. *BET Isotherm Analysis*

BET analysis used Nova 2200 instrument With Nitrogen gas as an adsorbate gas for surface area analysis. Prior to the BET analysis stage, the catalyst sample -weighing around 0.5 grams- is placed in the BET quartz cells which was connected to the degassing station for a period of 3 hours in order to remove any undesired volatile gases that might be stuck on the surface layer of the catalyst powder. This degassing process was conducted while the cell was jacketed with a heating mantle temperature of 150°C. Afterwards, the testing points were loaded using installed software and 88 points were selected for analysis: 49 adsorption points and 39 desorption points. The results for each catalyst include surface area, pore size, and volume. These are accompanied with the adsorption / desorption curves in order to analyze the isotherm type of the adsorption that took place on the relevant catalyst surface.

All BET results for each synthesized catalyst are summarized in Table 9 below.

Catalyst	Surface Area (m²/g)	Pore Size (nm)	Pore Volume (cc/g)
Hbeta zeolite	434	2.956	6.273e-2
Pd/Hbeta zeolite	449	3.688	1.810e-01
Pt/Hbeta zeolite	284	27.74	1.087e+00
Pt-Pd/Hbeta zeolite	155	318.26	1.802e+00
TiO ₂	39.5	2.948	1.745e-01
Pd/ TiO ₂	48.9	3.642	2.190e-01
Pt/ TiO ₂	57.48	2.95	1.973e-01
Pt-Pd/ TiO ₂	130.9	5.116	3.149e-01
Bi ₂ O ₃ / SiO ₂ / TiO ₂	85.5	3.558	4.442e-01

Table 9 BET isotherm analysis results: Surface area (m²/g), pore size (nm), and pore volume (cc/g)

In addition to the data listed in Table 9, Figure 18 -Figure 21 show the BET surface adsorption/desorption curve for all the catalysts that are based on Hbeta zeolite support.

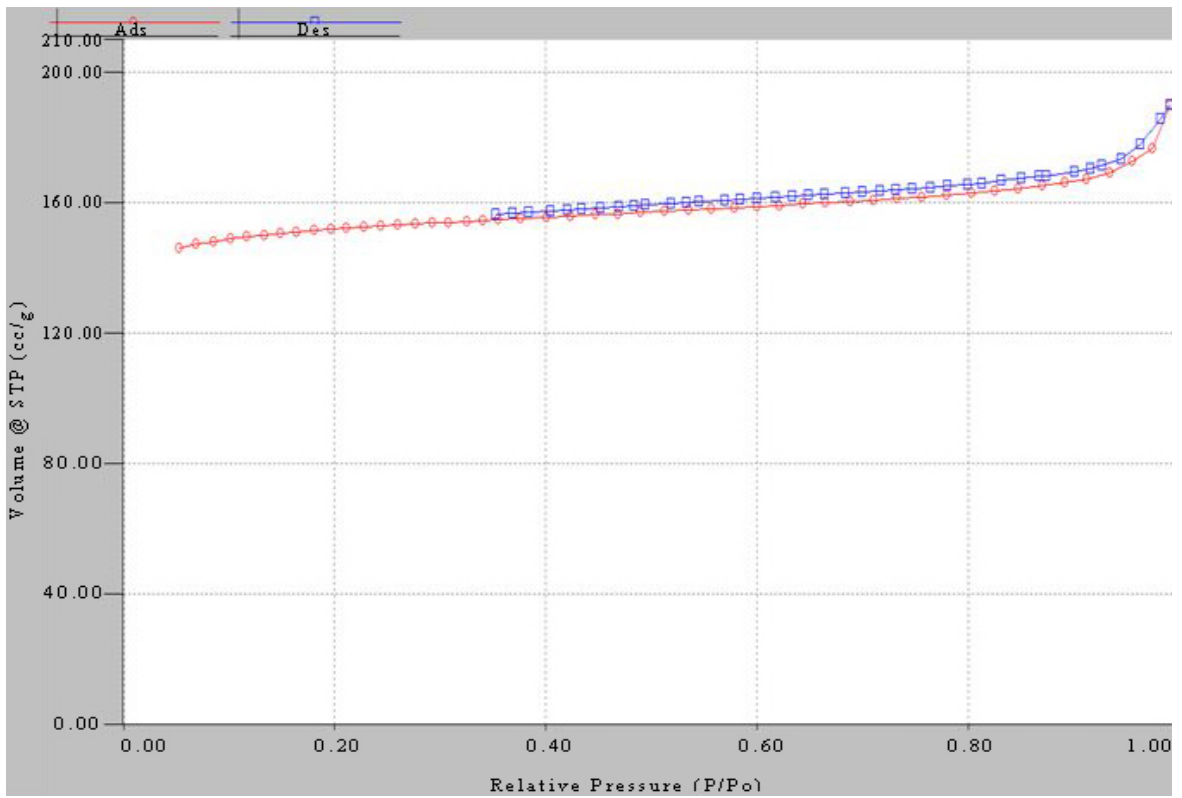


Figure 18 Hbeta zeolite BET adsorption/desorption curve

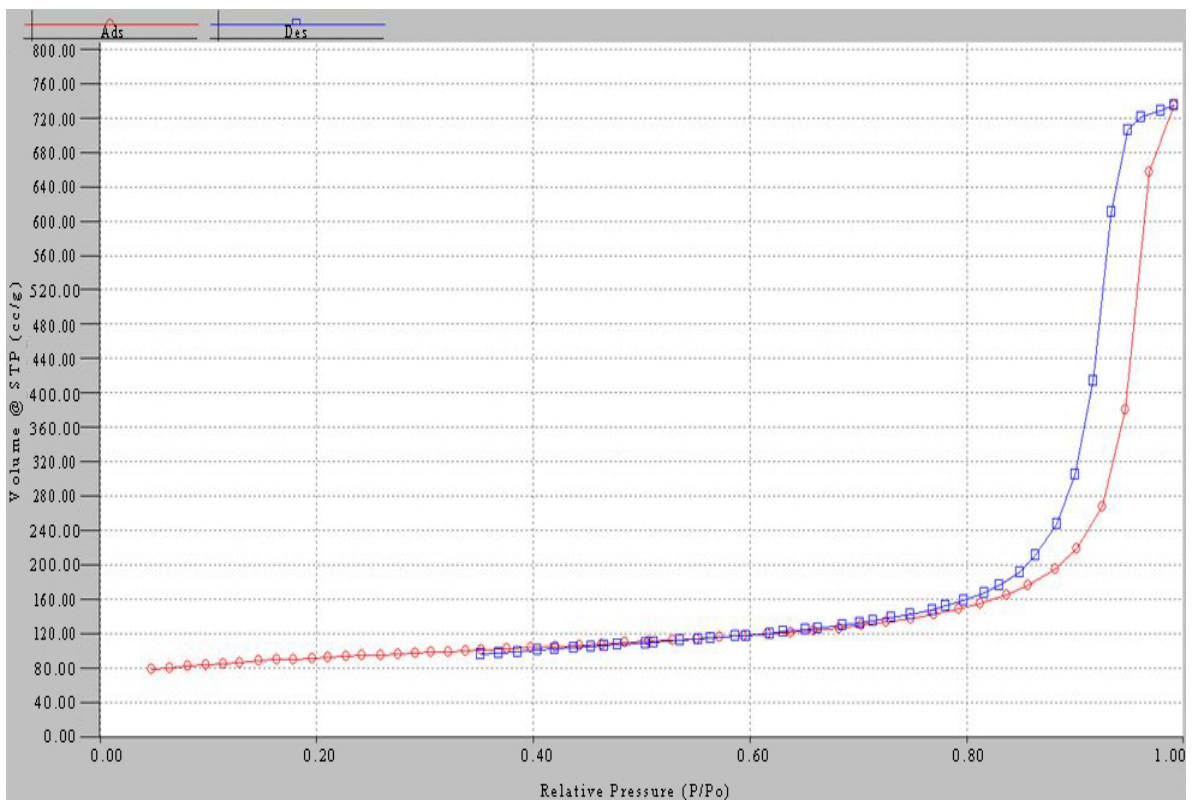


Figure 19 Pt/Hbeta zeolite BET adsorption/desorption curve

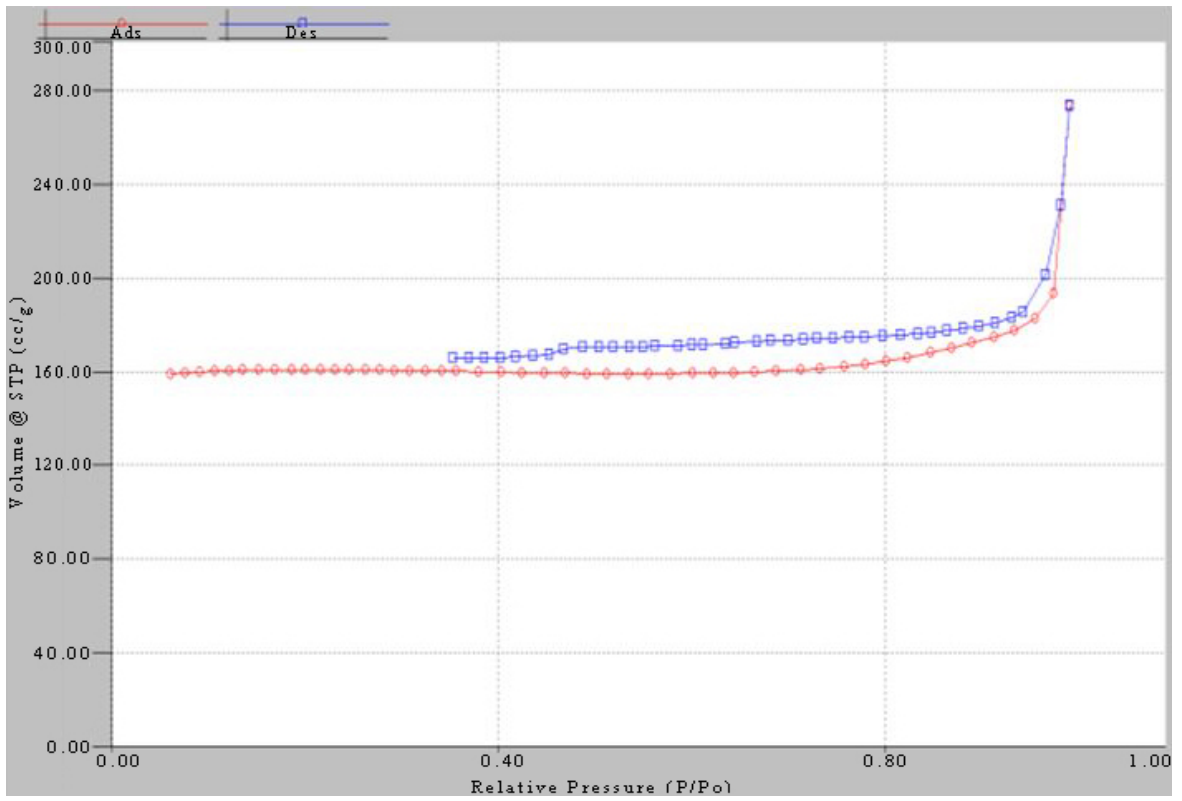


Figure 20 Pd/Hbeta zeolite BET adsorption/desorption curve

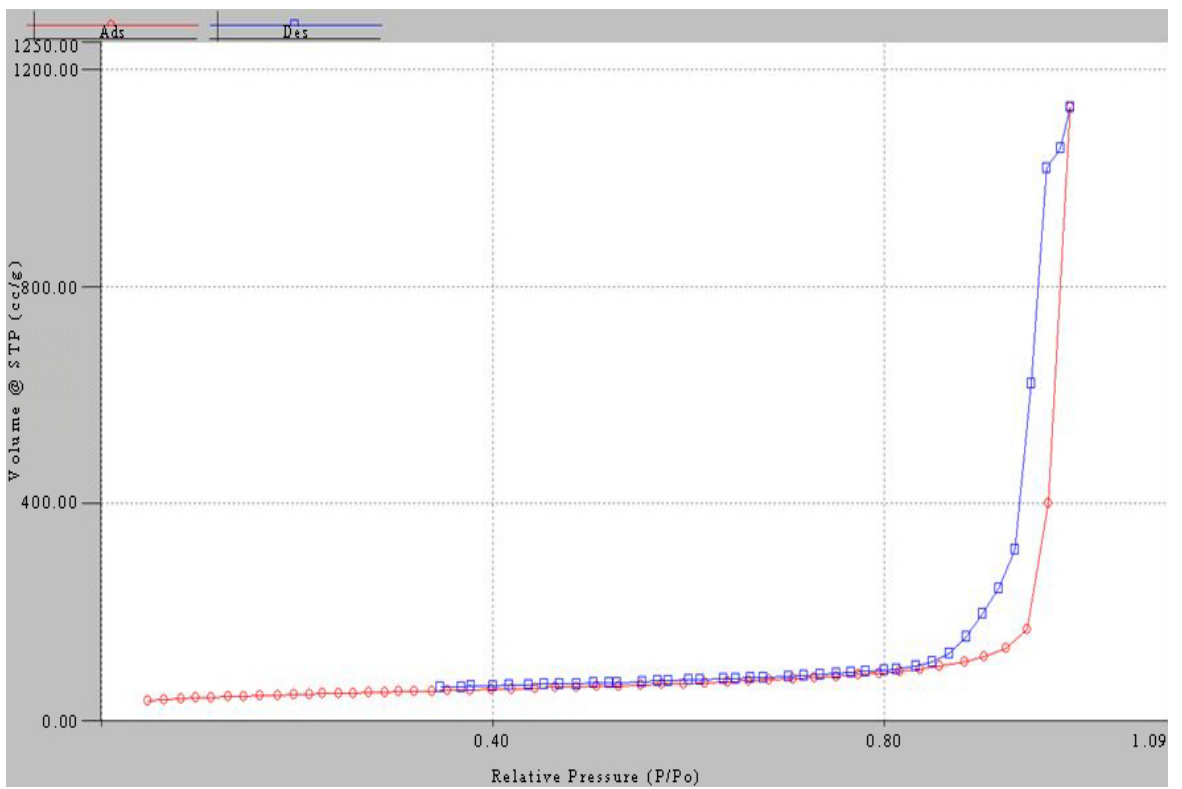


Figure 21 Pt-Pd/Hbeta zeolite BET adsorption/desorption curve

Similar BET isotherm curves are generated for TiO₂ based catalysts which are shown in Figure 22- Figure 26.

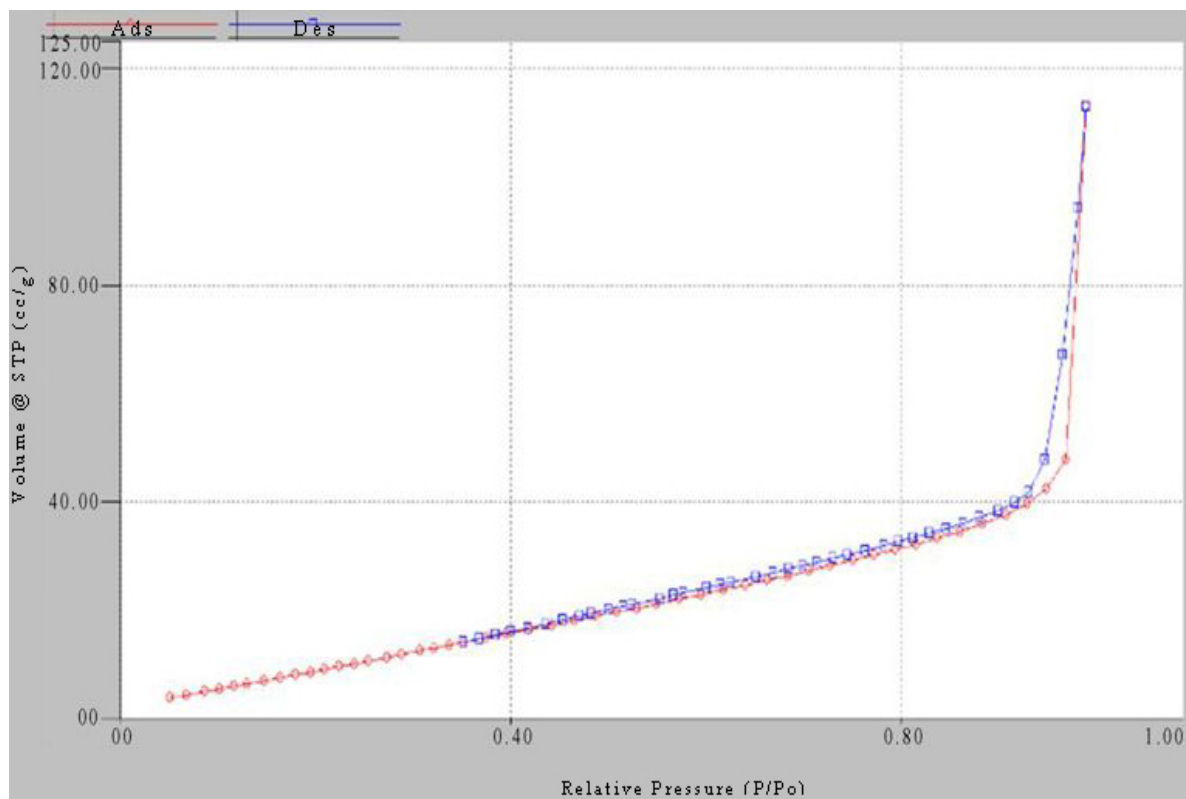


Figure 22 TiO₂ semi-conductor BET adsorption/desorption curve

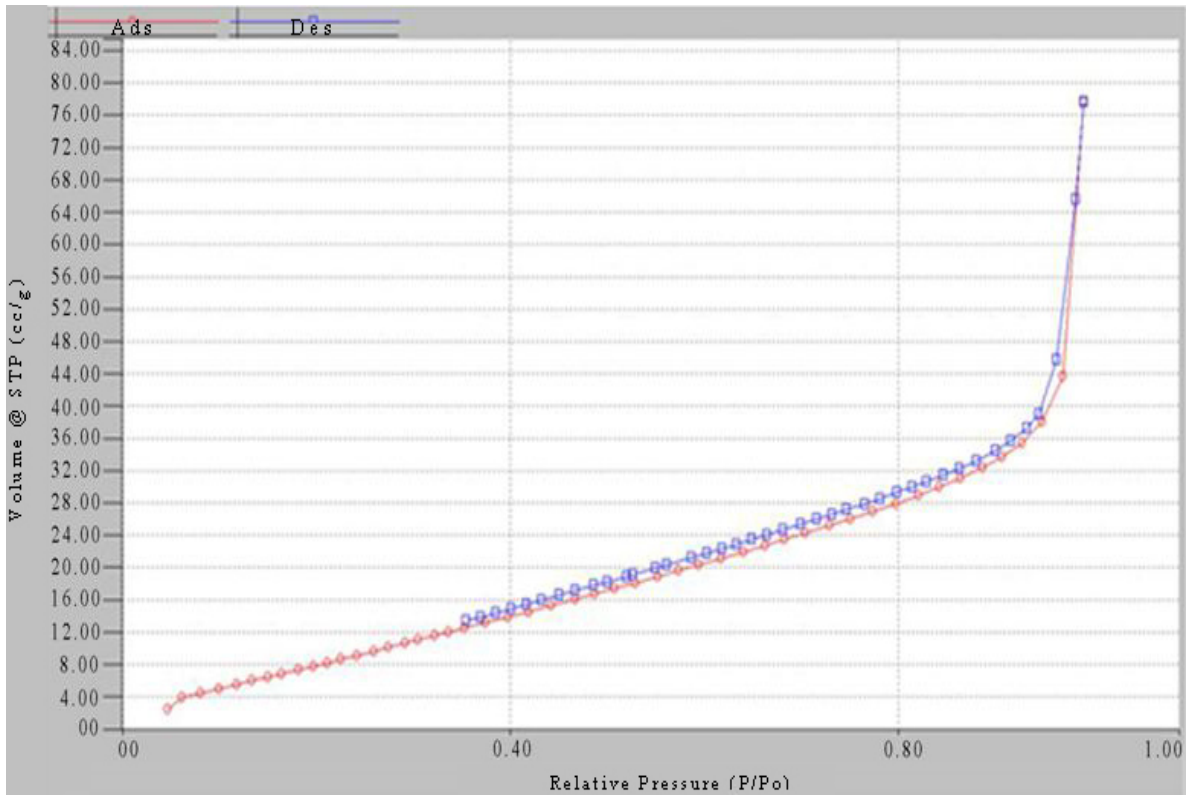


Figure 23 Pd/TiO₂ semi-conductor BET adsorption/desorption curve

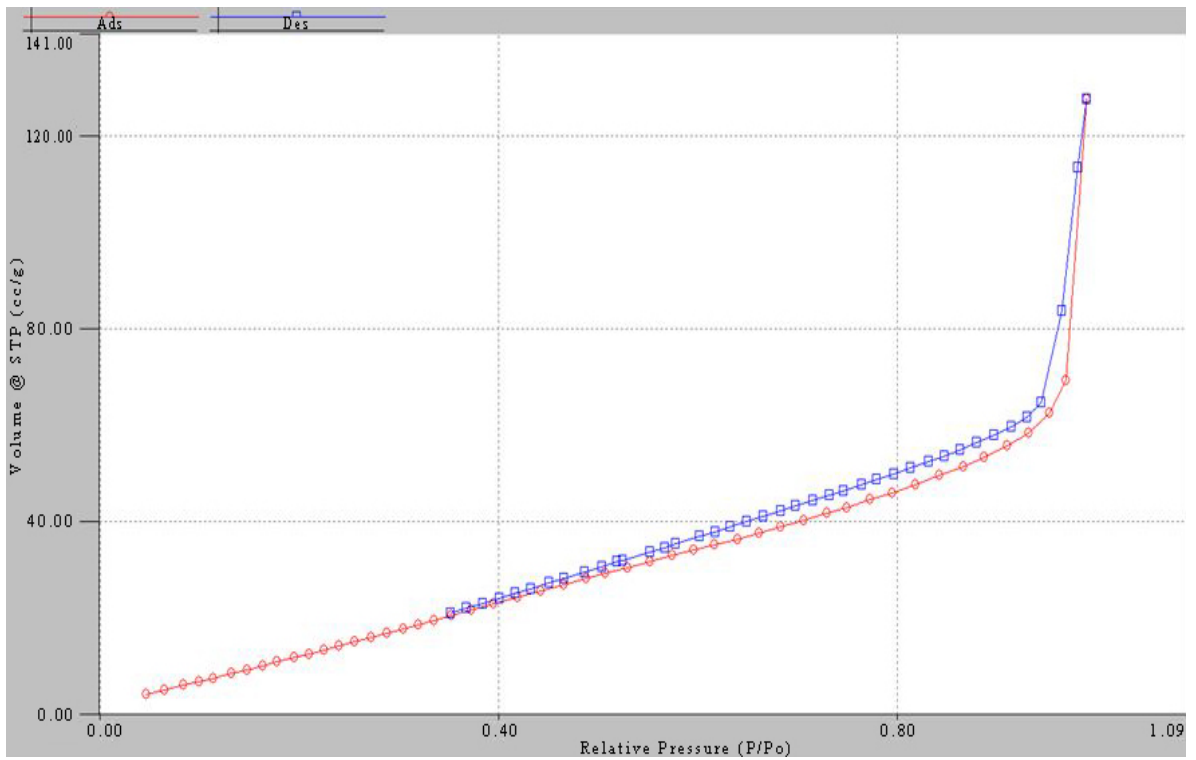


Figure 24 Pt/TiO₂ semi-conductor BET adsorption/desorption curve

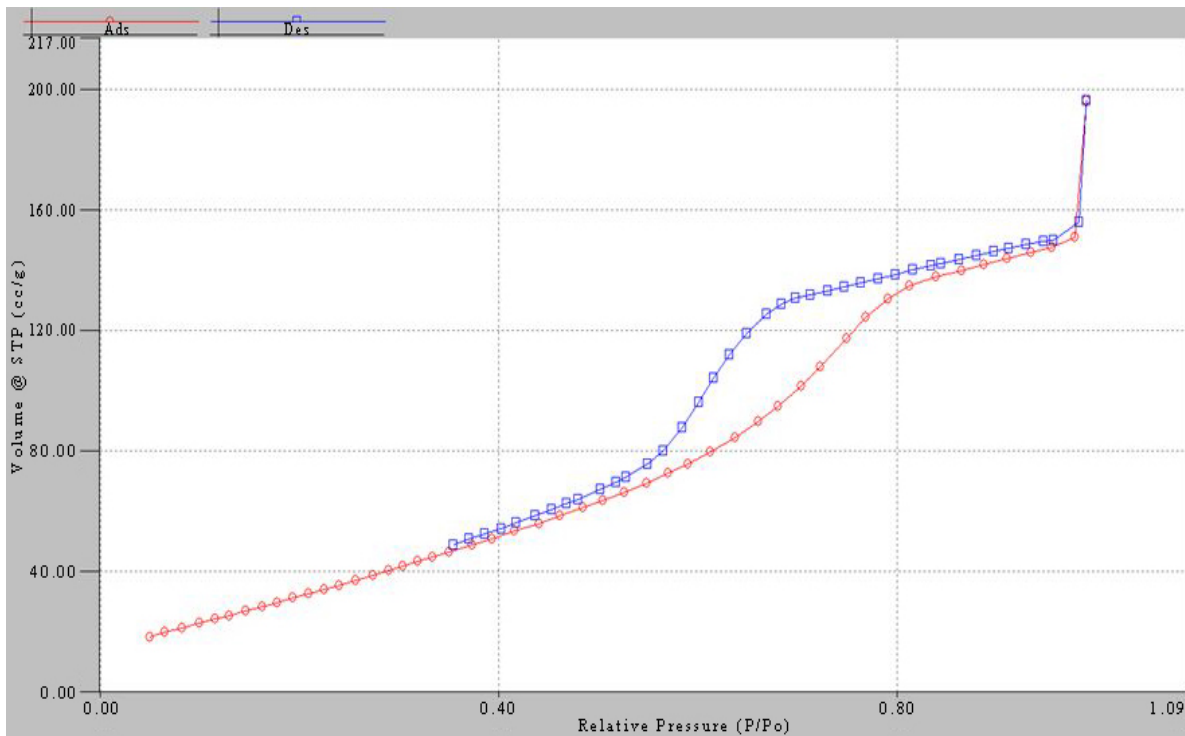


Figure 25 Pt-Pd/TiO₂ semi-conductor BET adsorption/desorption curve

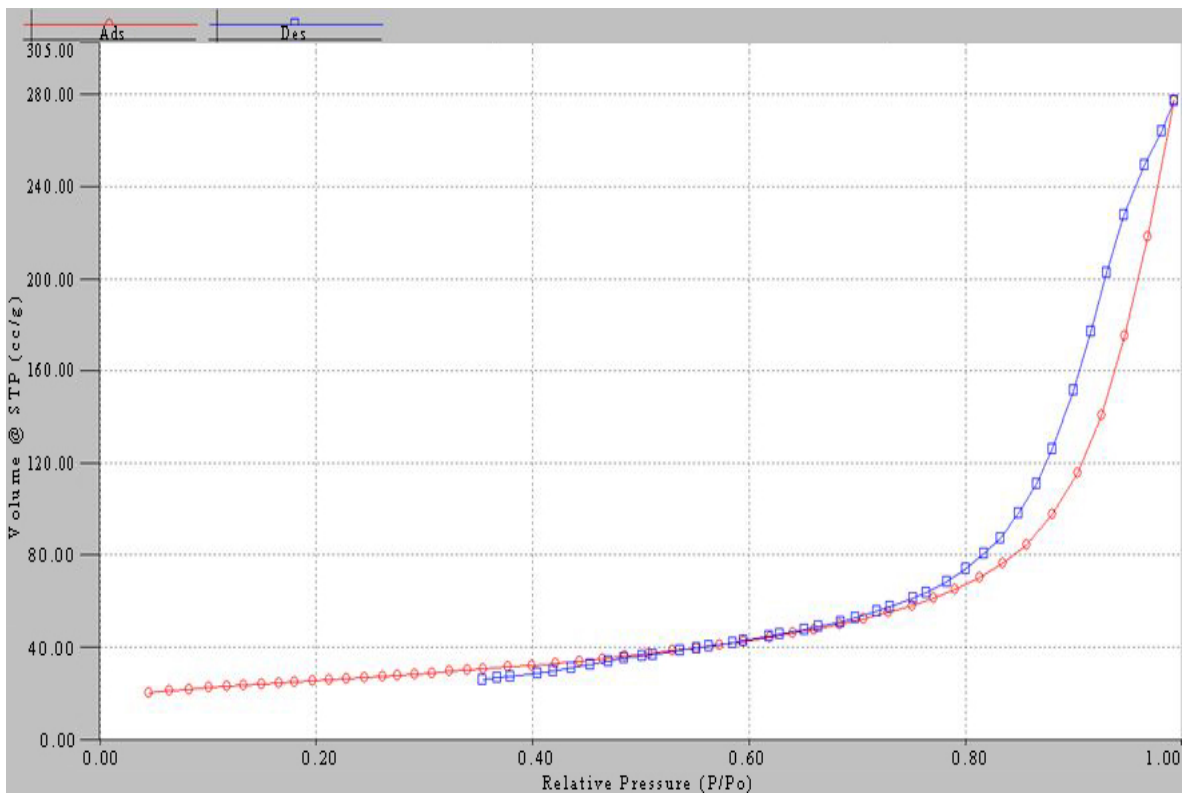


Figure 26 SiO₂/TiO₂/ Bi₂O₃ BET adsorption/desorption curve

In the BET analysis for Hbeta zeolite based catalysts: Hbeta zeolite, Pt/Hbeta zeolite, Pd/Hbeta zeolite, and bimetallic Pd-Pt/Hbeta zeolite (listed in Table 9), the results show that the surface area of synthesized Hbeta zeolite exceeds 400 m²/grams. It is noticed that the addition of a palladium on the zeolite surface resulted in an increase in the surface area to 450 m²/grams. Doping with palladium apparently did not decrease the surface area of the active sites of the catalyst. On the other hand, doping with platinum and bimetallic platinum/ palladium decreased the surface area to 284 m²/grams and 155m²/grams respectively. From the periodic table, we can see that platinum is bigger atom than palladium, for the Vander Waals radius of palladium and platinum is 163 Pico meter and 175 Pico meter, respectively. It is proposed that the larger atom, platinum, will reside on the surface rather than in the pores and thereby it will decrease the surface area. This hypothesis was confirmed by the invariability of the surface area after doping palladium on Hbeta zeolite surface. Furthermore, with palladium doping, it was noticed that both pore size and pore volume experienced a slight increase from 2.956 nm to 3.688 nm and from 6.273e-2 cc/g to 1.810e-01 cc/g respectively. However, when platinum was used, the pore size increased from 2.956 nm to 27.74 nm, approximately 9 folds. This is most probably due to the synergetic effect between platinum metal and the zeolite acidic surface, such that there might be a strong repulsion between platinum and the hydrogen protons at the extra-framework of the zeolite. This can be explained in the same manner for the enlarged pores (318.26 nm) resulting from doping both platinum and palladium metals (Table 9). Moreover, it is noticed that upon doping both metals, the pore size increased 107 times in comparison with doping Hbeta zeolite alone. This complies with the fact that states the repulsion effect of bimetals is larger than their size effect.

Analyzing adsorption/ desorption curves in Figure 18 - Figure 26 give an idea about the adsorption isotherms of the tested catalysts. The curve of desorption (in blue) is slightly distant from the adsorption curve (in red) in a way that an inflection point exists at smaller pressure values; this is called the hysteresis effect (Chorkendorff and Niemantsverdriet 2003). This phenomenon shown in Figure 27 is a sign of the need of a lower pressure for the removal of gas from the pores than the one needed for the gas entering the pores due to capillary forces. A very close match between our isotherm results and isotherm IV was observed.

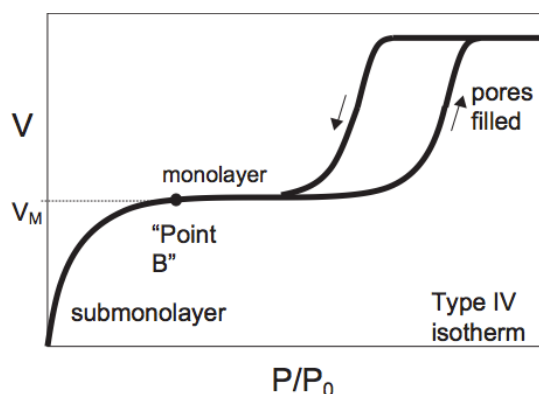


Figure 27 BET Type IV adsorption/desorption isotherm (Chorkendorff and Niemantsverdriet 2003)

As for the semi-conductor TiO_2 support catalyst, the surface area did not exceed $130 \text{ m}^2/\text{grams}$ for bimetallic $\text{Pt-Pd}/\text{TiO}_2$, and was below $100 \text{ m}^2/\text{grams}$ for both Pd/TiO_2 and Pt/TiO_2 : 48.9 and $57.48 \text{ m}^2/\text{grams}$, respectively. In addition, the tri-metallic catalyst $\text{Bi}_2\text{O}_3/\text{SiO}_2/\text{TiO}_2$ had a surface area of $85.5 \text{ m}^2/\text{grams}$.

It is clear that after doping noble metals on the semi-conductor surface, the pore size changed slightly unlike the case of the Hbeta zeolite surface. After palladium inclusion

onto TiO₂, the pore size increased slightly from 2.948 nm to 3.642 nm. As for the bimetallic addition, the pore size increased from 2.948 nm to 5.116 nm (Table 9). Despite the fact that there was an increase in the pore size in the bimetallic case, it is considered that there was no effective repulsion phenomenon with TiO₂ surface in comparison with Hbeta zeolite.

Regarding the surface area change of the TiO₂ catalyst, it is shown in Table 9 that the surface area did not change after doping platinum or palladium but only slightly. However, the surface area increased from 39.5 m²/grams to 130.9 m²/grams after doping bimetallic platinum and palladium; this can be a sign of introducing new pores to the surface of the TiO₂ support. The surface roughness might have also changed; this will be discussed later on in the XRD analysis (broadness of the peak).

2. XRD Analysis

The X-ray diffraction patterns were recorded by D8 Advance by Brucker with AVINCI design diffractometer using Cu ($\lambda = 0.15418$ nm); the software used is Diffrac.Eva and Diffrac. measurement. center. The X-ray tube was operated at 40 kV and 40 mA. The average X-ray emission time per increment is 3 seconds with an increment of 0.02. The starting and ending angles averaged between 5 and 85.

The graphs show the intensity versus angle theta (2θ). XRD results for every catalyst used are accompanied with library matches from literature of same compounds constituting the catalyst. The broadness and the peak's place were investigated in order to know if the catalyst framework has the suitable arrangement and configuration.

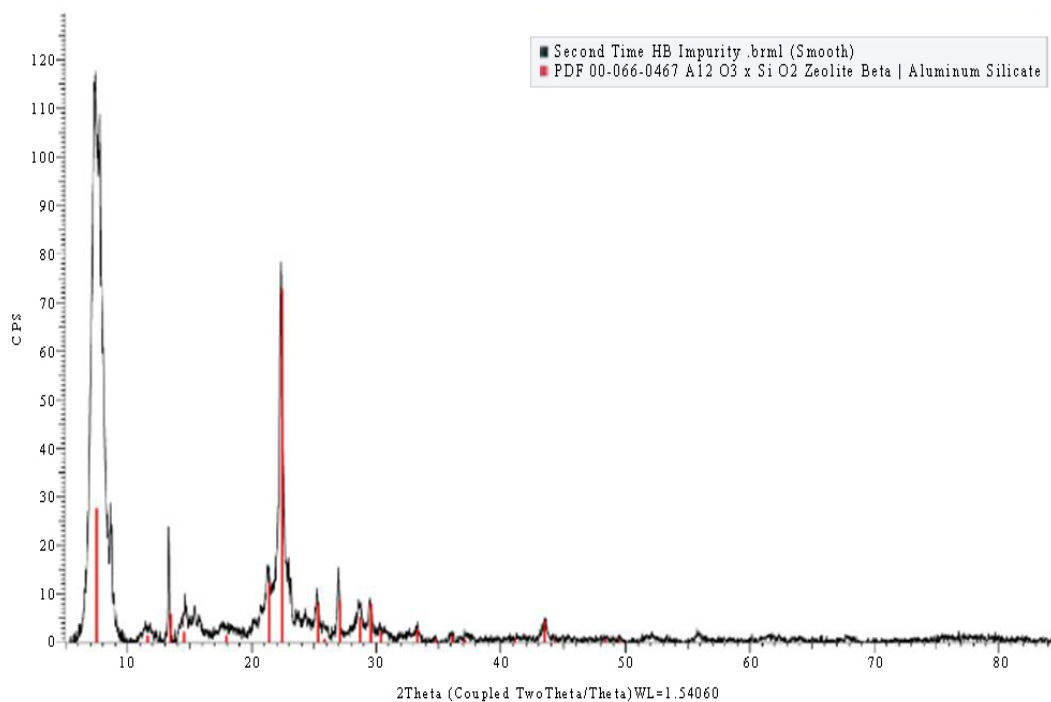


Figure 28 Hbeta zeolite catalyst XRD results at 2θ, WL=1.54060

The resulting peaks shown in Figure 28 where the corresponding catalysts are in black, while the red peaks correspond for the library matches of the $\text{Al}_2\text{O}_3 \cdot \text{SiO}_2$ Hbeta compound.

XRD is also performed on the noble metals doped on zeolite support catalysts; the results are shown in Figure 29 - Figure 31.

Commander Sample ID (Coupled TwoTheta/Theta)

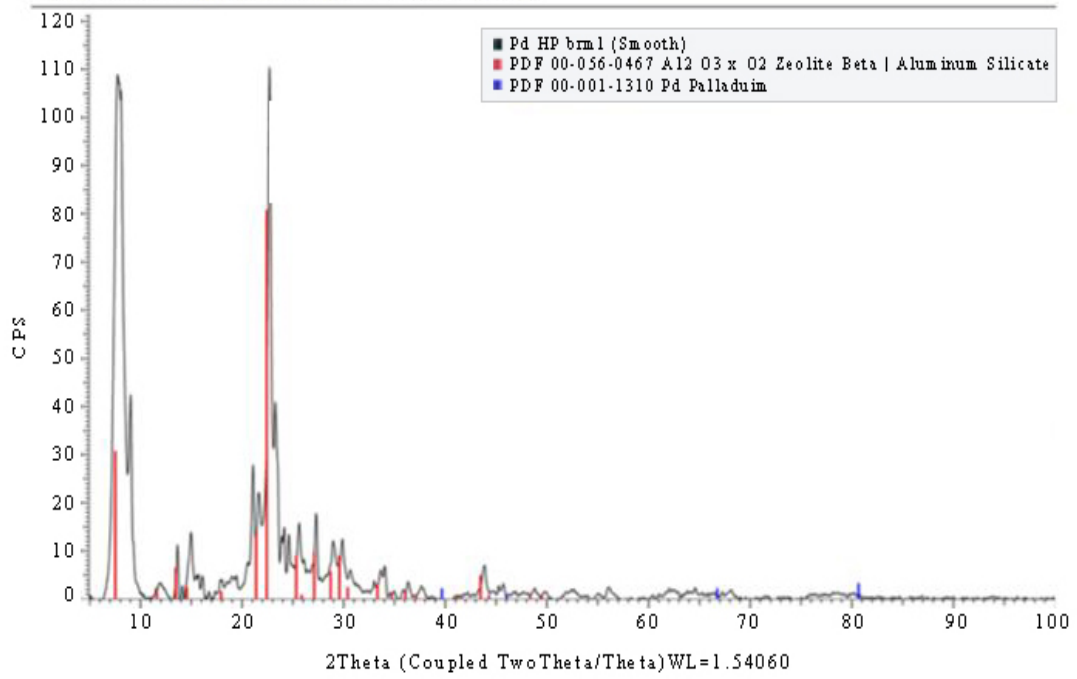


Figure 29 Pd/Hbeta zeolite XRD results at 2θ, WL=1.54060

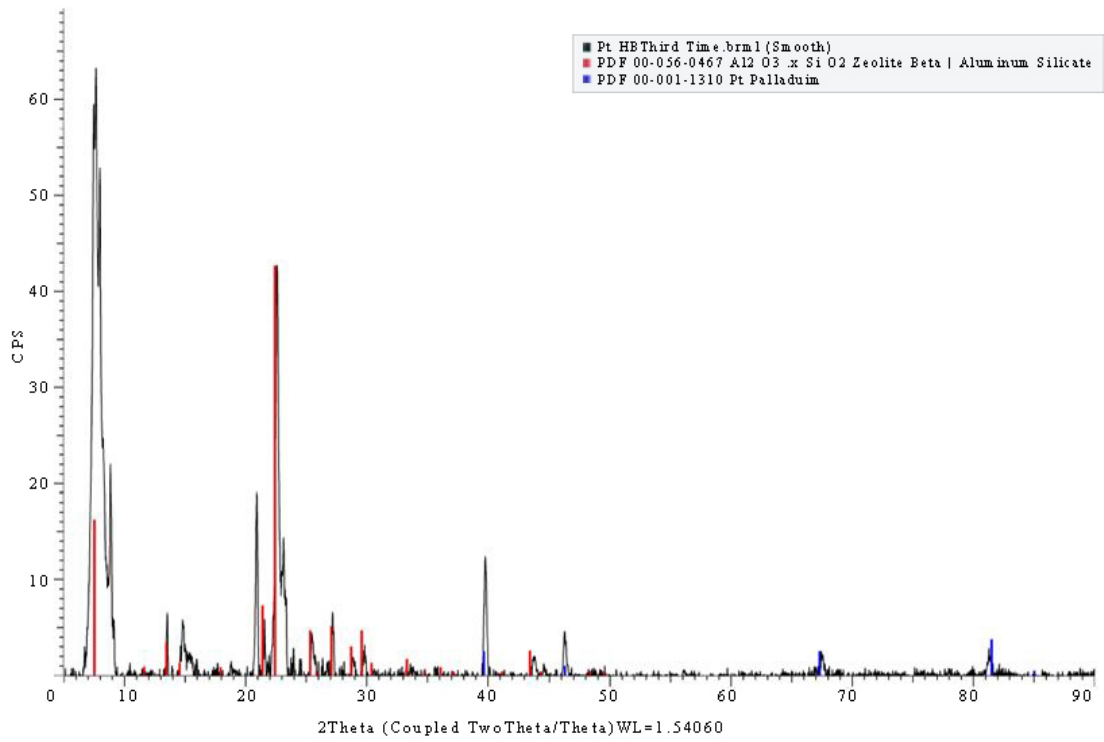


Figure 30 Pt/Hbeta zeolite XRD results at 2θ , WL=1.54060

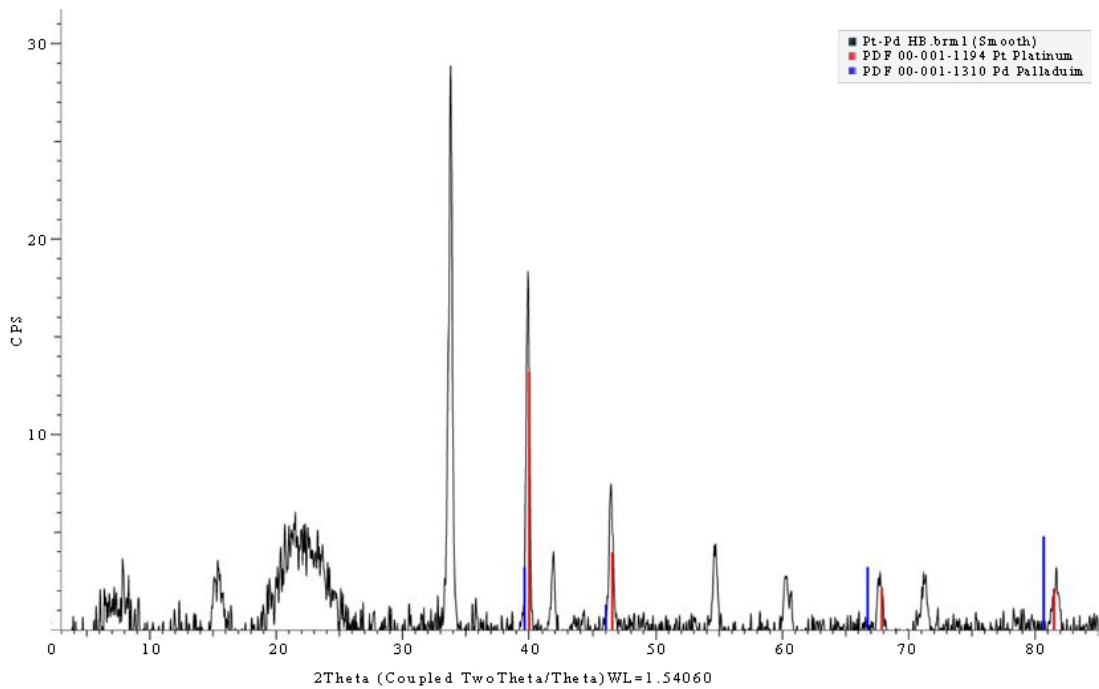


Figure 31 Pt-Pd/Hbeta zeolite XRD results at 2θ , WL=1.54060

Similarly, XRD tests are performed on TiO₂ bare semi-conductor catalyst and with noble metals. The results are shown in Figure 32- Figure 36.

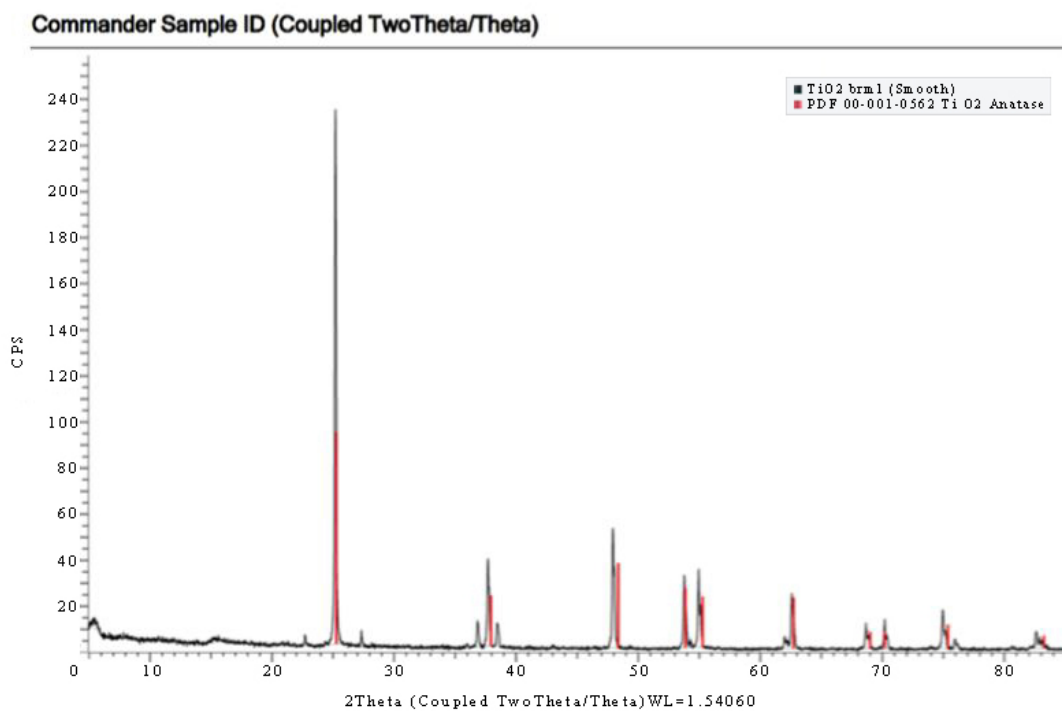


Figure 32 TiO₂ semi-conductor pure anatase XRD results at 2θ, WL=1.54060

Commander Sample ID (Coupled TwoTheta/Theta)

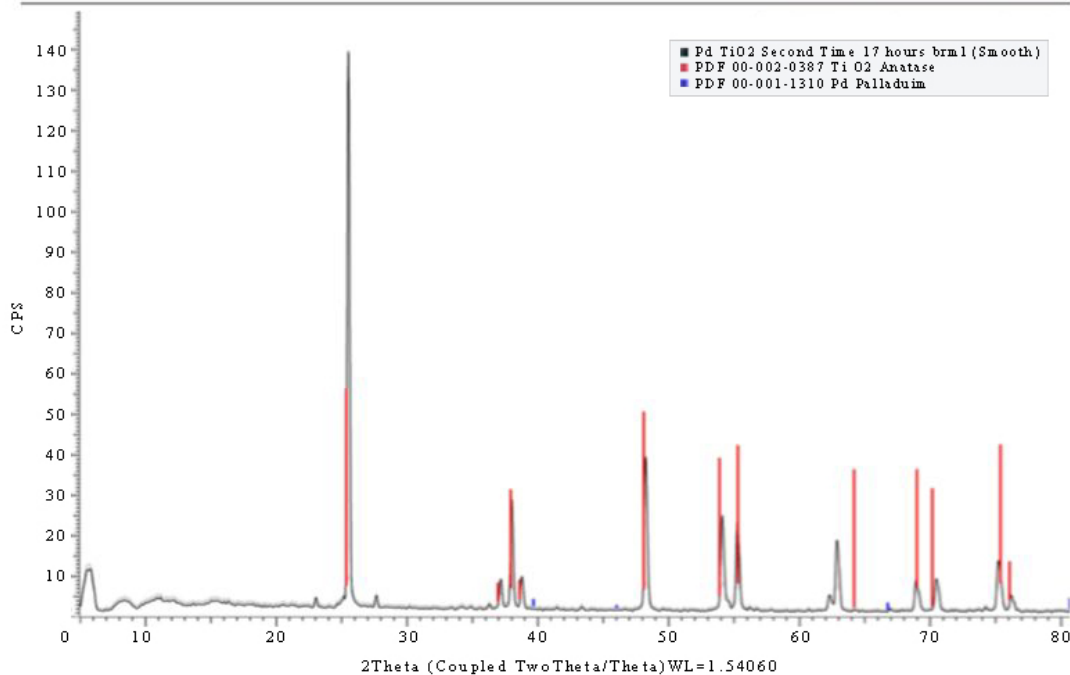


Figure 33 Pd/TiO₂ semi-conductor XRD results at 2θ, WL=1.54060

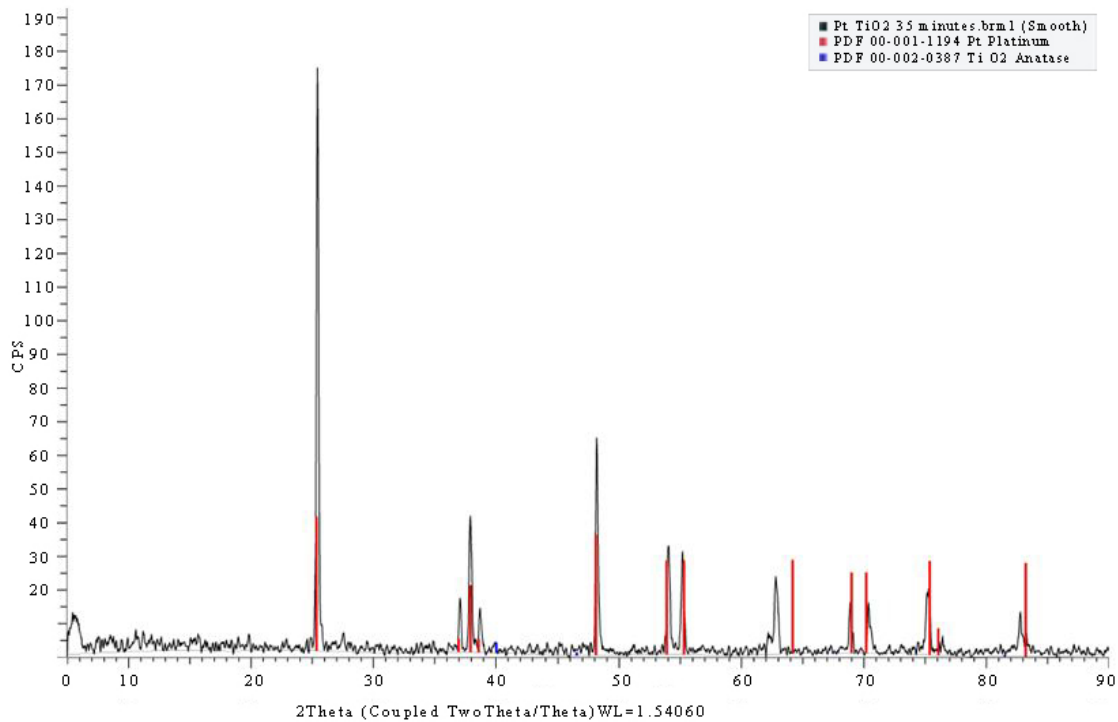


Figure 34 Pt/TiO₂ semi-conductor XRD results at 2θ, WL=1.54060

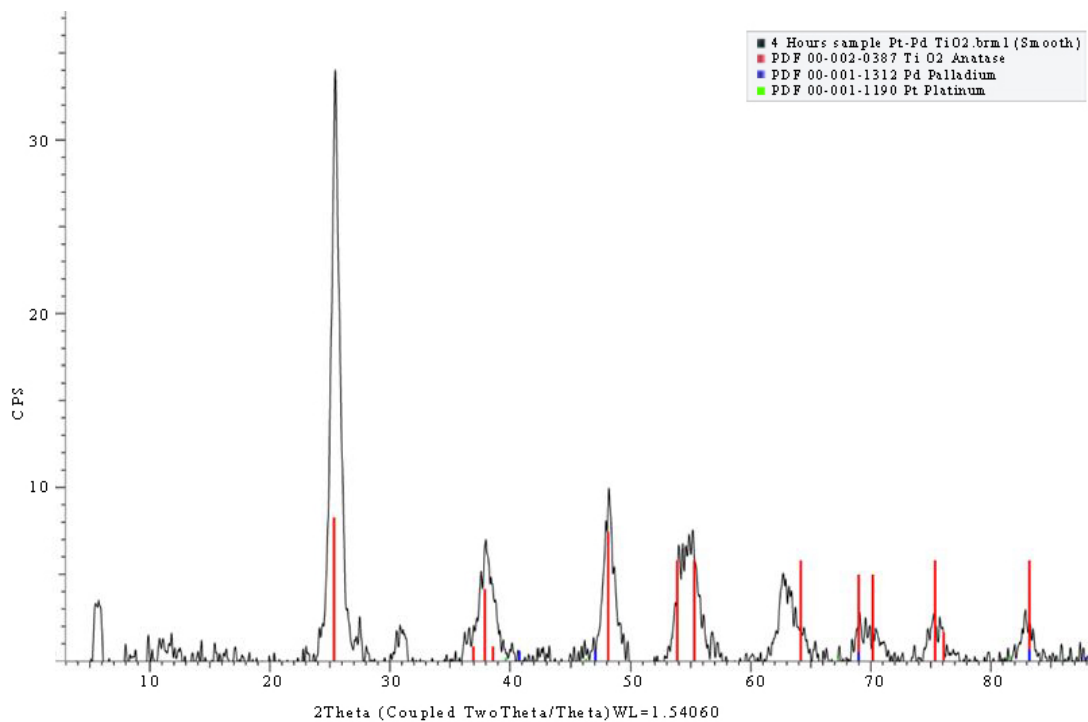


Figure 35 Pt-Pd/TiO₂ semi-conductor XRD results at 2θ, WL=1.54060

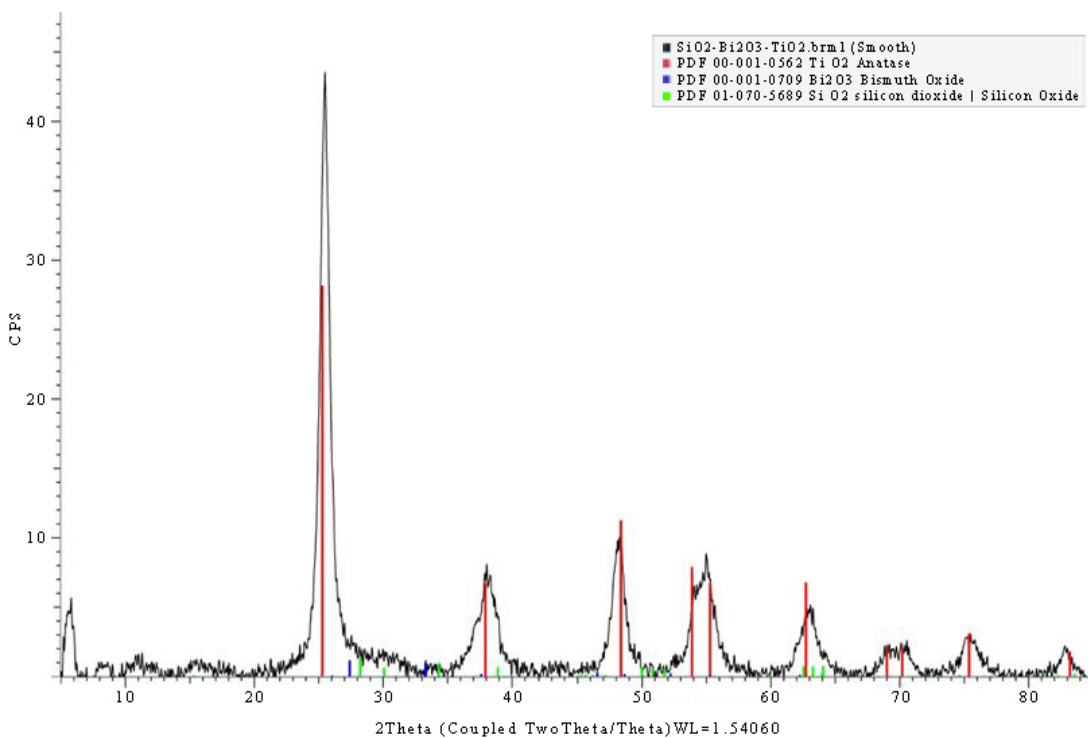


Figure 36 SiO₂/TiO₂/Bi₂O₃ XRD results at 2θ, WL=1.54060

The XRD analysis of the synthesized catalysts gives an idea about the surface nature or the framework behavior after doping noble metals onto the bare catalyst support. The bare Hbeta zeolite surface XRD results shown in Figure 28 display a great confirmation between the sample and the $\text{Al}_2\text{O}_3\cdot\text{SiO}_2$ compound that this zeolite is made up of. The XRD pattern is identical to the one by which the surface has developed the Beta configuration instead of ZSM-5 (Li et al. 2009).

Doping palladium metal onto Hbeta zeolite surface did not change the peaks of the zeolite composition significantly, so only small shifts of the peaks are noticed. Regarding the palladium inclusion, there were no clear peaks matching with the blue peaks (Figure 29) -representing the library peaks of palladium- and this can be explained by either the small quantities of the added palladium metal or by its high dispersion. Palladium might be residing inside the pores, which agrees with the BET analysis. Concerning platinum metal, zeolite compounds, and alumina silica oxide structure, they are still having a good validation with the red peaks of the zeolite library shown in Figure 30. Unlike palladium, platinum shows three peaks at angles $2\Theta = 39.5^\circ$, $2\Theta = 67.5^\circ$ and $2\Theta = 81.5^\circ$, on which all of them meet with the blue peaks of platinum in the library. The bimetallic platinum and palladium addition on Hbeta zeolite surface is demonstrated in Figure 31 which expresses the existence of broader peaks than those acquired from the single metal (either platinum or palladium) at angles $2\Theta = 22^\circ$ and $2\Theta = 23^\circ$. The XRD results concerned with the bimetallic zeolite complex catalyst have such kind of peaks with noticeable noise and can be explained by an induced disturbance of the framework of Hbeta zeolite pore rings that is in accordance with the high escalation of pore size shown in Table 9 (318.26nm). This disturbance can be explained also due to the layered

structure, which bimetallic Pt-Pd/Hbeta zeolite has as shown later in SEM image (Figure 40)

Concerning TiO₂ catalyst supports, the pure anatase bare catalyst is presented in Figure 32. The results noticeably match with literature at high intensity peaks of $2\theta = 25^\circ$, $2\theta = 38^\circ$, $2\theta = 48^\circ$. After doping palladium metal on TiO₂, the structure of TiO₂ did not change (Figure 33). It is noticed that, again, palladium is not having any peaks matching with blue palladium peaks from the library. This is similar to what took place when doping palladium on Hbeta zeolite; due to the high dispersive characteristic of palladium. In the case of platinum doped on TiO₂, the TiO₂ anatase framework did not change, while platinum was still appearing with a small peak at $2\theta = 39.5^\circ$, as shown in Figure 34, which is similar to the peak that was detected in the Pt/Hbeta zeolite but with less significant intensity.

On the subject of bimetallic Pt/Pd on TiO₂, Figure 35 shows that the XRD peaks, which are matching with the red peaks of TiO₂ anatase, are broader than the previous anatase peaks shown in Figure 32 - Figure 34. This kind of broad peaks in XRD is a significant outcome of a non-uniform strain of the framework of the powder catalyst. So it is clear that doping both metals on TiO₂ eventually disturbed the framework of the catalyst; this disturbance might be due to slight repulsion forces. This is somehow noticed in the BET results in Table 9 where the addition of both metals increased the pore size from 2.948 nm to 5.116 nm. It is observed that as per the addition of bimetallic Pt and Pd in both cases; Hbeta zeolite and TiO₂ supports, the XRD peaks widened. So this gives a clearer idea about the increase of the pore size and the catalyst pores.

Figure 36 shows a high matching between the XRD peaks of the anatase TiO₂ and the red peaks of the anatase TiO₂ in the library. In addition, it is observed that the tri-

metallic catalyst has a slightly broad peaks matching with all the relevant metals involved in the library. This disturbance will be investigated by SEM imaging in the following section.

3. SEM Analysis

This characterization technique is also applied on the synthesized catalysts in order to test the morphology of the catalyst's surface. An attempt was done to apply the microscopic imaging with the same working distance and voltage intensity, however, the contrast differed between samples catalysts, therefore, appropriate working distance, scanning speed, and detector were used to get the best image of the catalyst surface. In SEM images the areas which have higher contrast are those that correspond to the particles that are facing the detector.

Figure 37 -Figure 40 show the microscope images for the Hbeta zeolite based catalysts. The SE detector of the SEM machine gives clear images for the catalyst surface. However, the magnification scale and working distance were different in order to get the optimal clear image for each one. Since SEM is based on an electron beam that is sent to the surface, the working distance is adjusted carefully because the electron beam can interfere with the metals that constitute the catalyst.

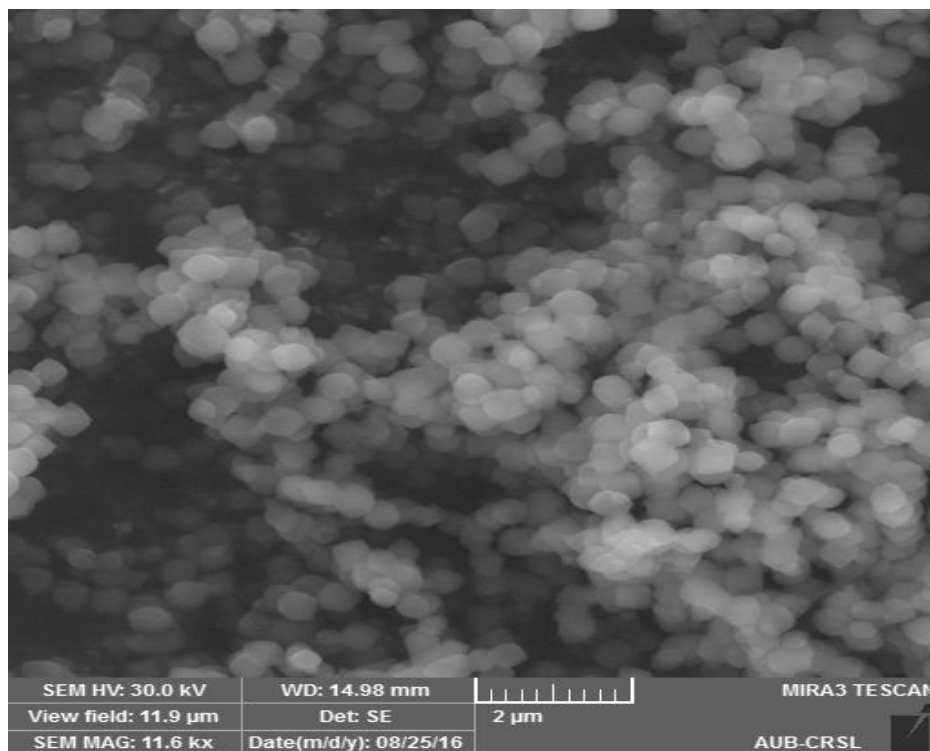


Figure 37(SEM) Scanning electron microscope image for Hbeta zeolite

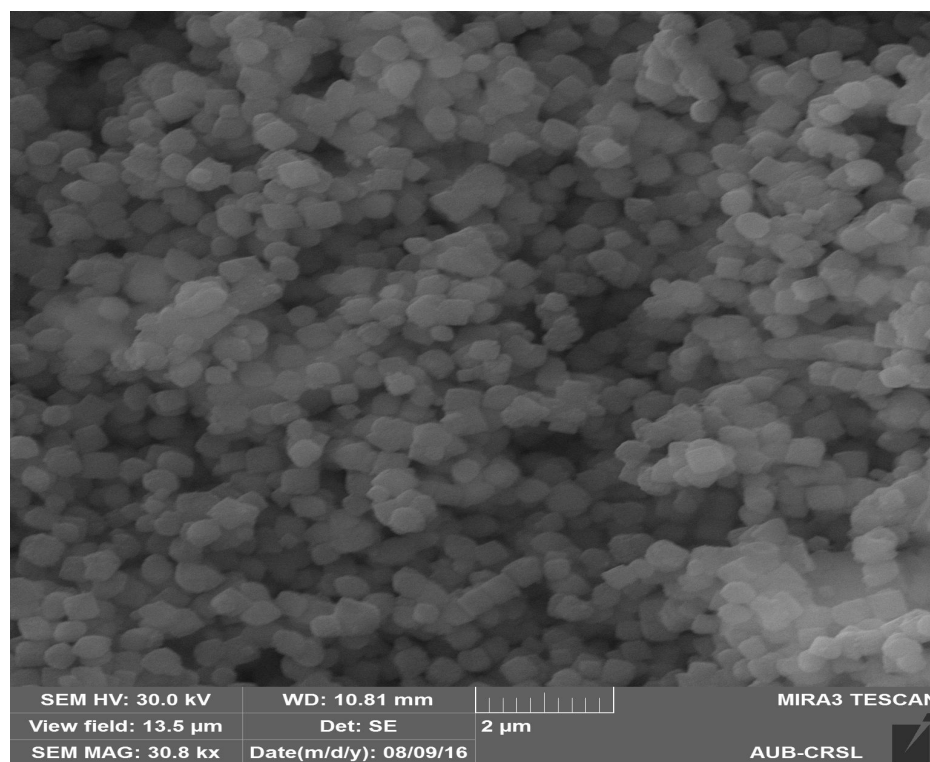


Figure 38 (SEM) Scanning electron microscope image for Pd/Hbeta zeolite

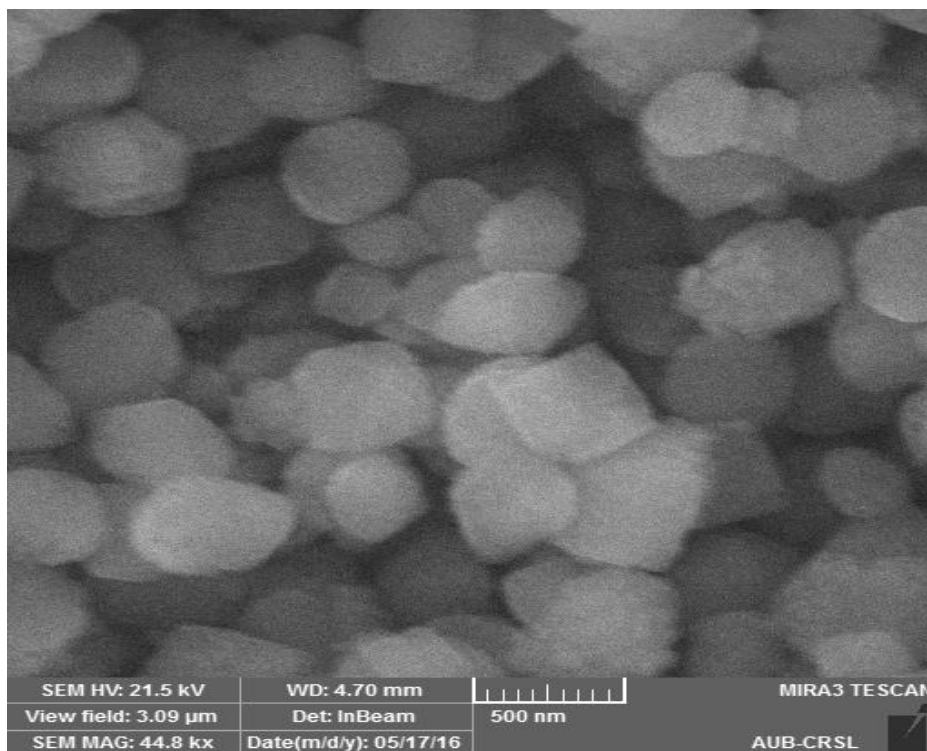


Figure 39 (SEM) Scanning electron microscope image for Pt/Hbeta zeolite

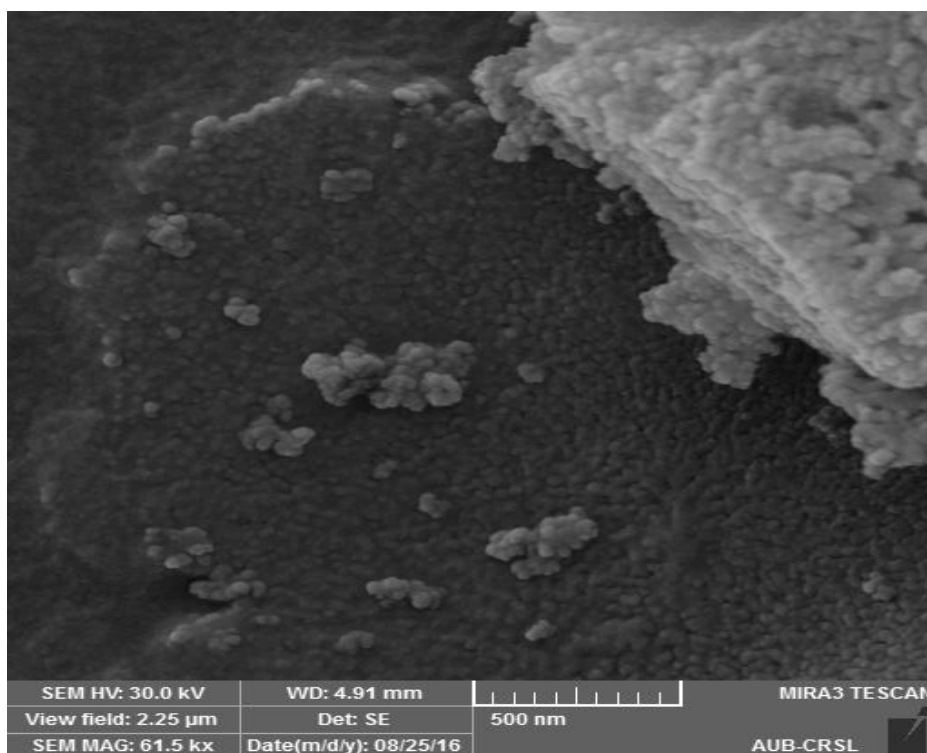


Figure 40 (SEM) Scanning electron microscope image for Pt-Pd/Hbeta zeolite

Figure 41 - Figure 45 show the SEM images for the catalysts that are based TiO₂ support. Similarly, these images were executed by the SE detector of SEM machine that gives clear contrast for the catalysts at close working distance of an average of 10mm.

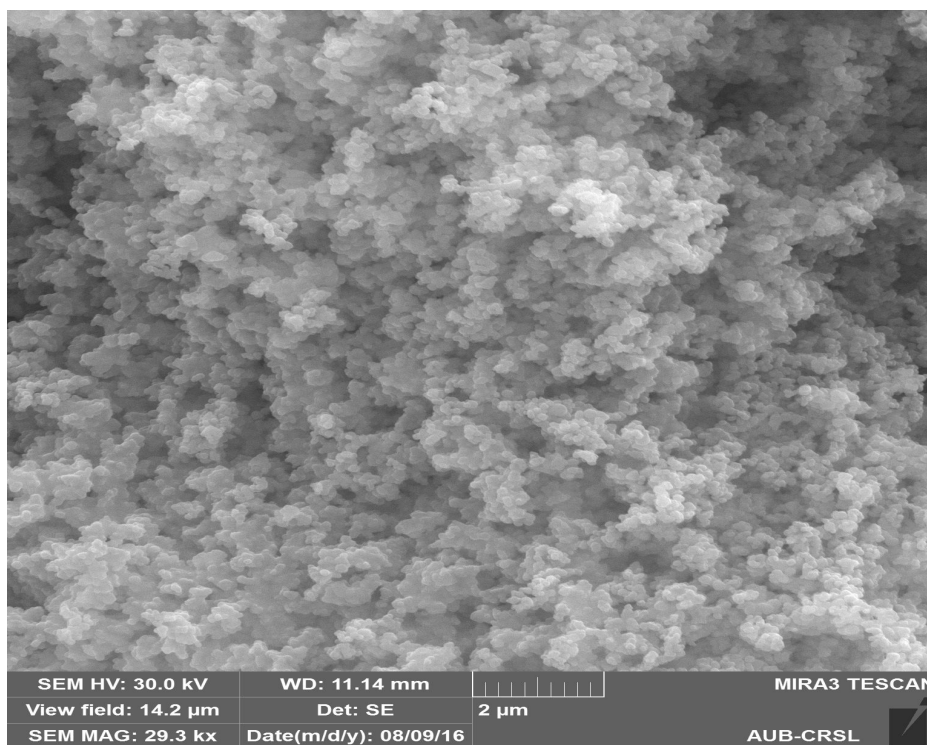


Figure 41 (SEM) Scanning electron microscope image for TiO₂ semi-conductor

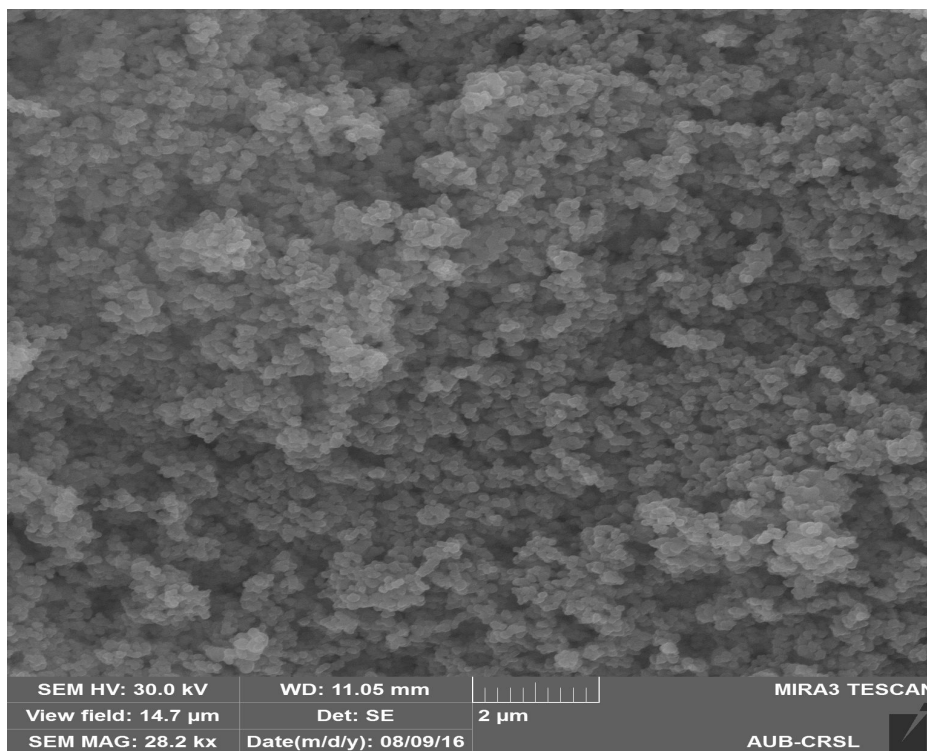


Figure 42 (SEM) Scanning electron microscope image for Pd/TiO₂ semi-conductor

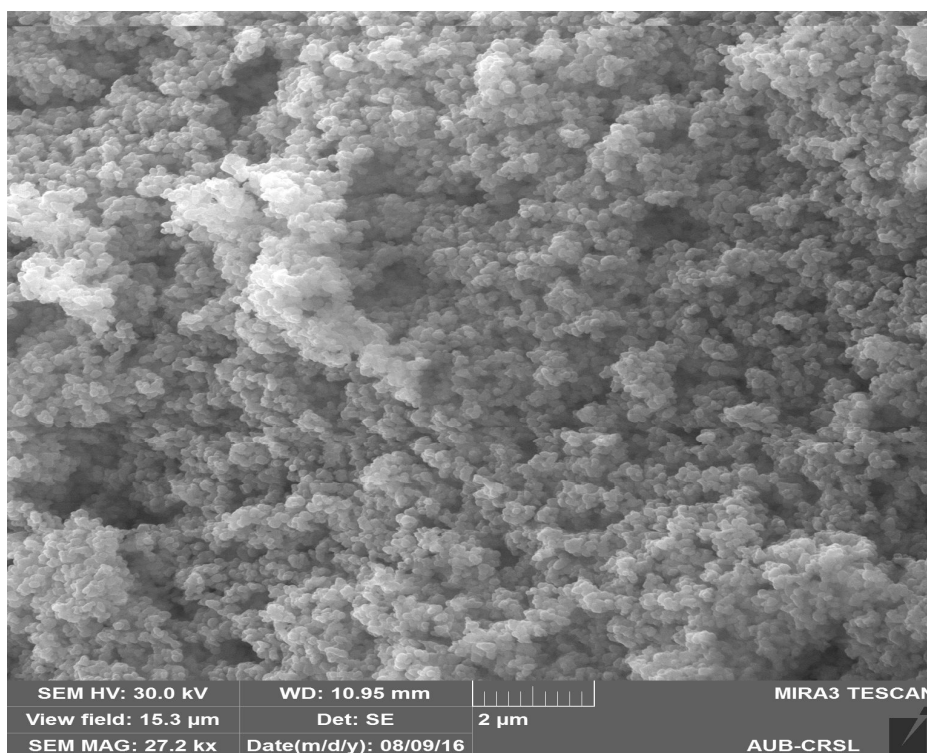


Figure 43 (SEM) Scanning electron microscope image for Pt/TiO₂ semi-conductor

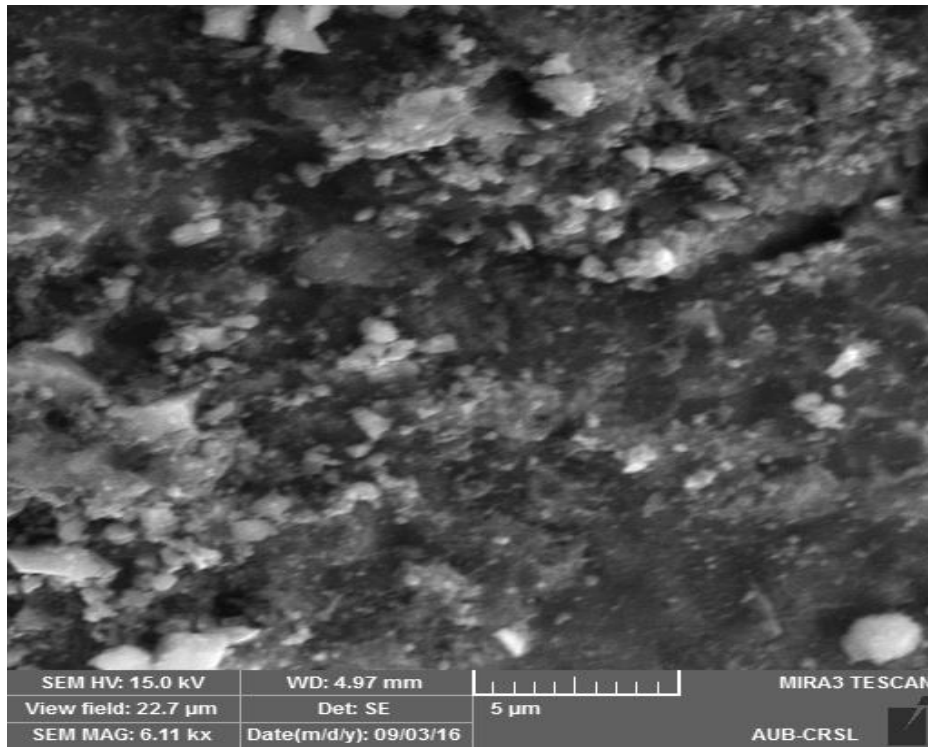


Figure 44 (SEM) Scanning electron microscope image for Pd-Pt/TiO₂ semi-conductor

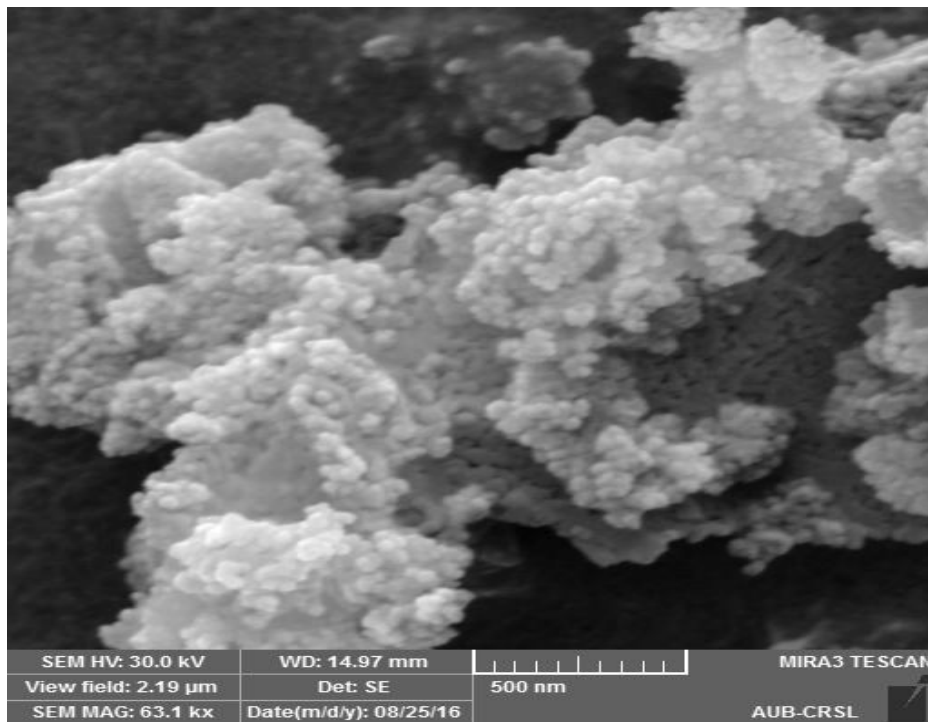


Figure 45 (SEM) Scanning electron microscope image for Bi₂O₃/SiO₂/TiO₂

In relation to the SEM images, it is clear from Figure 37 and Figure 38 that doping palladium metal on Hbeta zeolite did not change the framework of the zeolite, and the tetrahedral structure is still the same. The estimated particle size of Pt/Hbeta zeolite (Figure 39) is 0.4545 μm while that of Pd/Hbeta zeolite (Figure 38) is around 0.6 μm . This increase in the particle's size confirms with the increase of the surface area between Pt/Hbeta zeolite (284 m^2/g) and Pd/Hbeta zeolite (449 m^2/g).

In Figure 40, the SEM image for the bimetallic Hbeta zeolite shows that there are two layers above each other. It might be asserted that this specification is causing a lower gas conversion in comparison with a singular metal doping on Hbeta zeolite. As we mentioned previously, that this layered structure caused crystalline structure disturbance inclusion.

Concerning the TiO_2 bare anatase catalyst, the particle size is detected by SEM at a working distance of 11.14 mm and a magnification of 29.3 kx to be around 0.206 μm (Figure 41). After the inclusion of the palladium noble metal, the morphology in Figure 42 expresses that the particles are still somehow circular in shape with a slight increase in size: 0.2142 μm at working distance of 11.05 mm and a magnification of 28.2 kx. The SEM image of platinum active metal on semi-conductor TiO_2 is shown in Figure 43; it is estimated from the image scale that the particle size is around 0.20 μm . As for the bimetallic TiO_2 catalyst, particle size is measured to be 1 μm (Figure 44). In the case of semi-conductor TiO_2 support, the particles' sizes were too close to each other only in the case of single metal doping, which is consistent with the close values of their surface areas (49 m^2/g and 57 m^2/g). On the other hand, the bimetallic TiO_2 catalyst, having a larger particle's size of 1 μm (Figure 44), meets with the larger surface area: 131 m^2/g .

It is observed that the surface imaging for the bimetallic Pt-Pd/TiO₂ catalyst (Figure 44) didn't show any layered structure, unlike the case of the bimetallic Pt-Pd/Hbeta catalyst (Figure 40). This is in good agreement with the XRD characterization results that gave wider crystalline peaks for the bimetallic Pt-Pd/Hbeta (Figure 31) in comparison to Pt-Pd/TiO₂ (Figure 35). This is due to the layered structure of the bimetallic Hbeta.

In Figure 45, the SEM image for the tri-metallic catalyst shows a layered structure as well, similar to the case of the bimetallic Pt-Pd/Hbeta catalyst. This is illustrated by the broad peaks of its crystalline structure framework shown in Figure 36.

4. EDX analysis

The X-ray detector of the SEM machine enables us to detect the composition of the target point/region selected on the catalyst's surface. The outcome of this analysis is highlighted in several graphs showing the peaks of the elements that interfered with the X-rays. In addition the analysis generates a table of the elements that were detected with their relevant composition and percentages that correspond to the selected point.

Figure 46 shows the peaks of the elements corresponding to the selected spectrum on the surface of the catalyst. In addition, Table 10 shows both the weight % and the atomic % as well for the same selected spectrum.

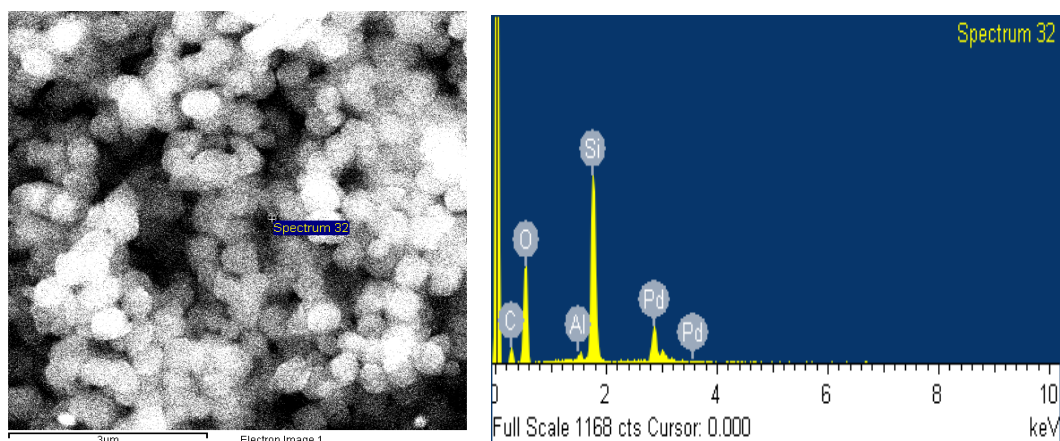


Figure 46 (EDX) Energy dispersive x-ray spectrum for Pd/Hbeta zeolite catalyst

Element	Weight %	Atomic %
C K	15.08	22.67
O K	56.51	63.79
Al K	0.54	0.36
Si K	17.85	11.48
Pd L	10.03	1.70
Totals	100.00	

Table 10 Composition analysis for the selected spectrum on point 32

Figure 47 shows the elements detected for spectrum 6 selected on the surface of Pt/Hbeta zeolite catalyst. Table 11 shows the composition of spectrum 6 with the corresponding weight and atomic percentages of the elements.

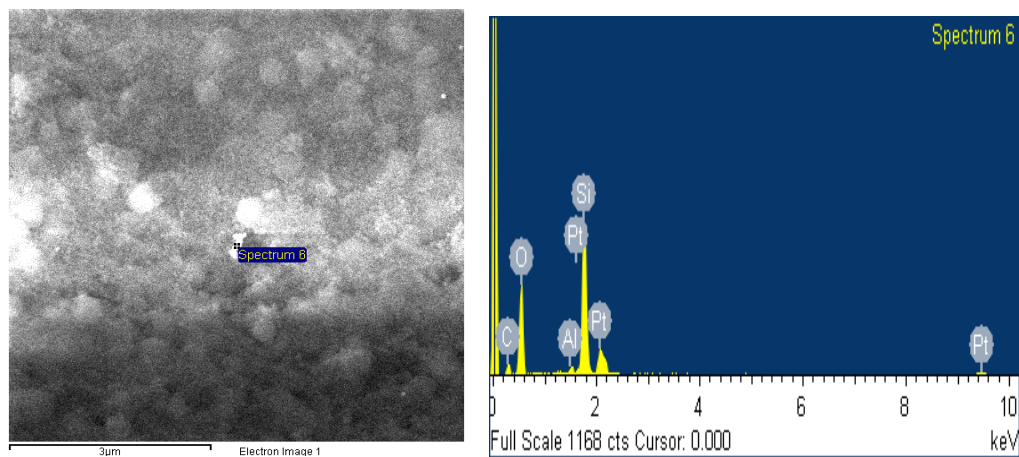


Figure 47 (EDX) Energy dispersive x-ray spectrum for Pt/Hbeta zeolite catalyst

Element	Weight %	Atomic %
C K	14.09	22.68
O K	50.94	61.55
Al K	0.77	0.55
Si K	20.08	13.82
Pd L	14.11	1.40
Totals	100.00	

Table 11 Composition analysis for the selected spectrum on point 6

The bimetallic zeolite support catalyst Pt-Pd/Hbeta zeolite was examined in order to investigate the existence of the noble metals doped onto its surface. Figure 48 shows the peaks of elements platinum and palladium doped on the zeolite surface made up of alumina and silica oxides groups. In addition,

Table 12 shows the composition of these metals and support components at spectrum point 4.

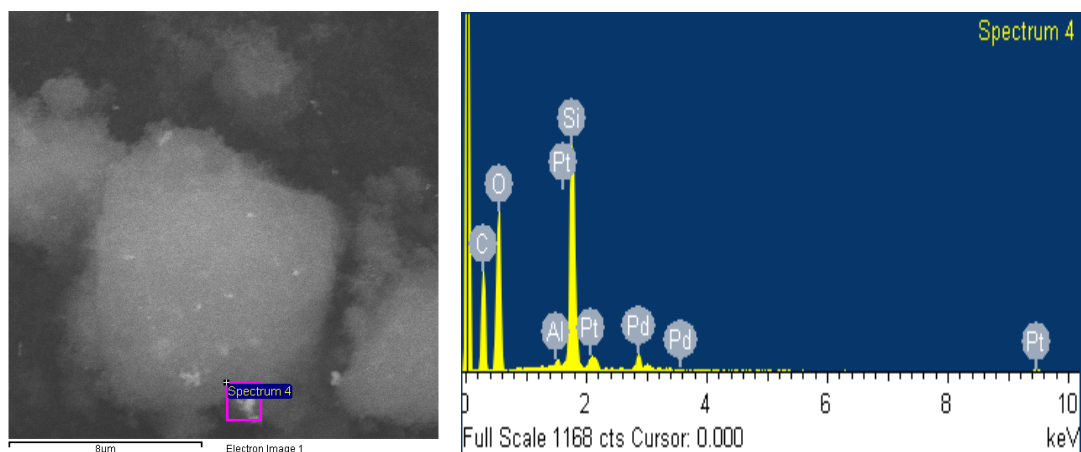


Figure 48 (EDX) Energy dispersive x-ray spectrum for Pt-Pd/Hbeta zeolite catalyst

Element	Weight %	Atomic %
C K	37.34	48.21
O K	46.42	44.99
Al K	0.32	0.18
Si K	11.00	6.07
Pd L	2.31	0.34
Pt M	2.61	0.21
Totals	100.0	

Table 12 Composition analysis for the selected spectrum on point 4

As for TiO₂ semi-conductor support, EDX was done for Pt/TiO₂ shown in Figure 49 accompanied with composition analysis in

Table 13. The peaks are displayed at point spectrum 8; the detected elements Pt, Ti and O are shown with their relevant composition in the

Table 13.

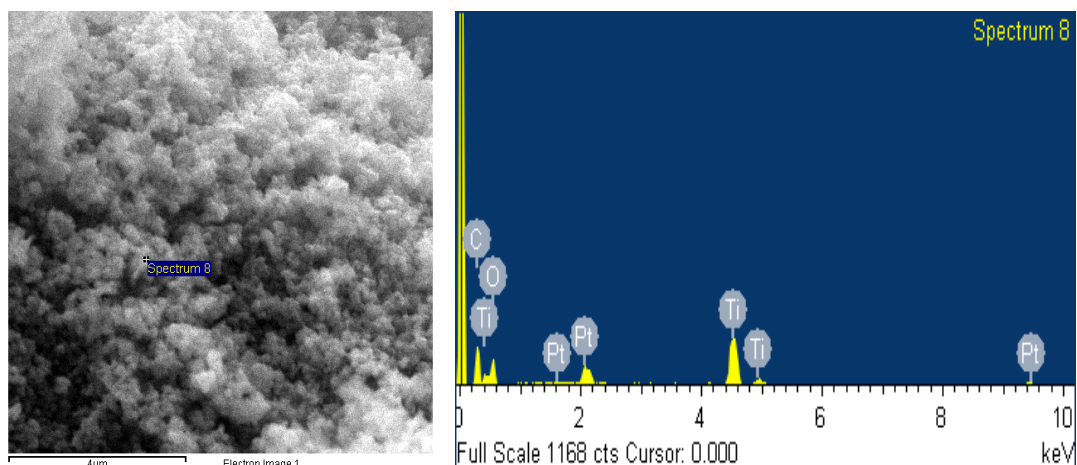


Figure 49 (EDX) Energy dispersive x-ray spectrum for Pt/TiO₂ semi-conductor catalyst

Element	Weight %	Atomic %
C K	30.86	48.41
O K	34.93	41.14
Ti K	24.08	9.47
Pt M	10.12	0.98
Totals	100.0	

Table 13 Composition analysis for the selected spectrum on point 8

The second noble metal doped on TiO₂ surface was palladium which was investigated by the EDX characterization technique as well. Figure 50 shows the peaks detected by EDX for the region selected by spectrum 1. Similarly Table 14 shows the composition for the same spectrum as Figure 50; the detected peaks correspond to elements: Ti, O, and C (the absence of palladium metal was noted).

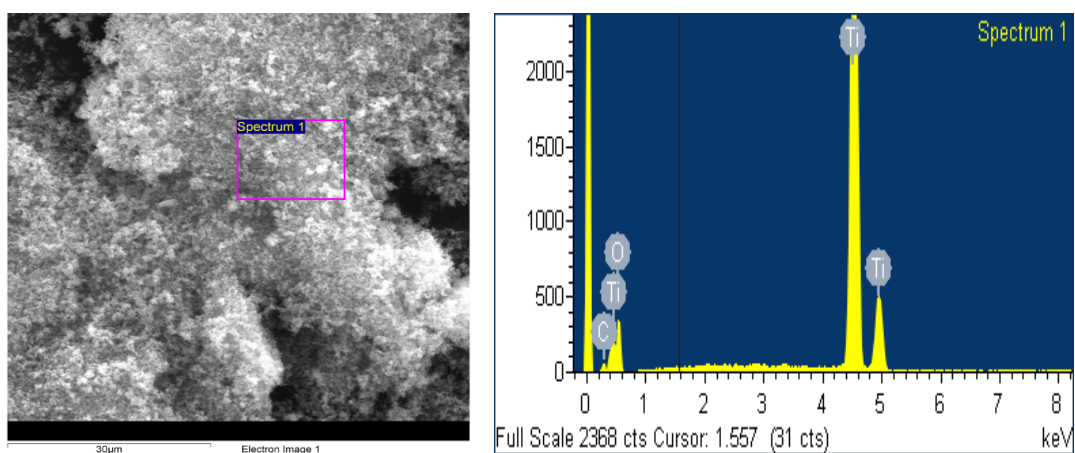


Figure 50 (EDX) Energy dispersive x-ray spectrum for Pd/TiO₂ semi-conductor catalyst

Element	Weight %	Atomic %
C K	3.64	7.09
O K	46.98	68.76
Ti K	49.39	24.35
Totals	100.00	

Table 14 Composition analysis for the selected spectrum on point 1

A similar investigation was done for the bimetallic catalyst Pt-Pd/TiO₂. Both existing elements' peaks and compositions are shown in Figure 51 and Table 15 respectively.

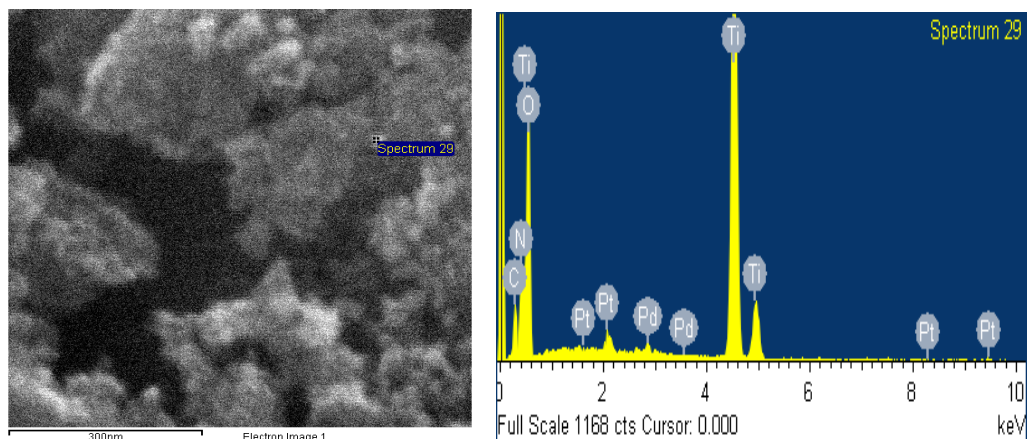


Figure 51 (EDX) Energy dispersive x-ray spectrum for Pt-Pd/TiO₂ semi-conductor catalyst

Element	Weight %	Atomic %
C K	8.22	14.57
O K	52.99	44.99
Ti K	35.74	15.89
Pd L	1.14	0.23
Pt M	1.91	0.21
Totals	100.0	

Table 15 Composition analysis for the selected spectrum on point 29

As for the 3 component catalysts Bi₂O₃/SiO₂/TiO₂, an EDX composition analysis shown in Table 16 was performed for a square region spectrum 1 instead of point (Figure 52) in order to capture all possible elements.

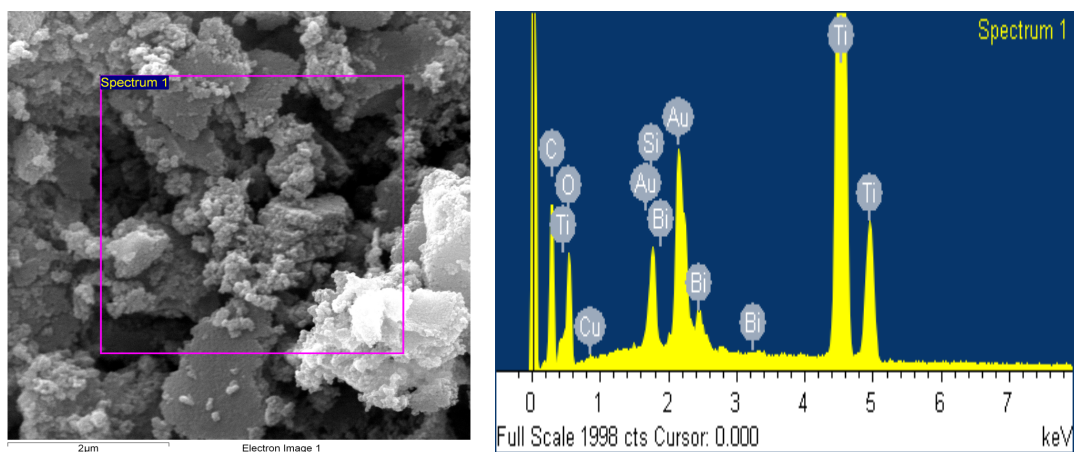


Figure 52 (EDX) Energy dispersive x-ray spectrum for $\text{Bi}_2\text{O}_3/\text{SiO}_2/\text{TiO}_2$ catalyst

Element	Weight %	Atomic %
C K	26.40	46.02
O K	28.89	37.83
Si K	1.81	1.35
Ti K	30.69	13.42
Cu K	0.35	0.12
Au L	9.65	1.03
Bi L	2.21	0.22
Total	100.00	

Table 16 Composition analysis for the selected spectrum region 1

From EDX analysis, it was not easy to detect the existence of noble metals doped on either Hbeta zeolite or TiO_2 supports; this is due to the low loading ratio of the metals. However, the support composition silica and alumina constituting the Hbeta zeolite and titanium oxide gave highest peaks. For example, silica (Si) was detected at 1.8 Kev and alumina (Al) at 1.5 Kev (

Figure 46 -Figure 48). The titanium oxide supported catalysts appeared to have high peaks of titanium (Ti) at 0.4, 4.3 & 5 Kev, oxygen (O) was detected at 0.5 Kev for all catalysts used including both Hb zeolite and semi-conductor TiO₂ supports, and carbon (C) peak was detected at 0.3 Kev (Figure 49 - Figure 51). The existence of the carbon element was due to the carbon tape used to deposit the sample catalyst over the pin in order to be placed under the electron gun.

It is noticed that the noble metals platinum and palladium appeared at the same voltage intensity for all the catalysts combinations. Platinum (Pt) peak appeared at 1.6 and 2.1 Kev, while palladium (Pd) appeared at higher electron intensity: 2.9 Kev and 3.6 Kev. Figure 52, shows the peaks of the elements of Bi₂O₃/SiO₂/TiO₂ catalyst. Gold (Au) is detected due to gold plating performed to the sample before EDX analysis.

B. Pyrolysis Results

The aim is to maximize the pyrolytic gas yield among other pyrolysis products like oil, and carbon black (Figure 53). The difference in the weight of the quartz tube before and after the pyrolysis, represents the non-condensable portion of the waste rubber which the gas product.

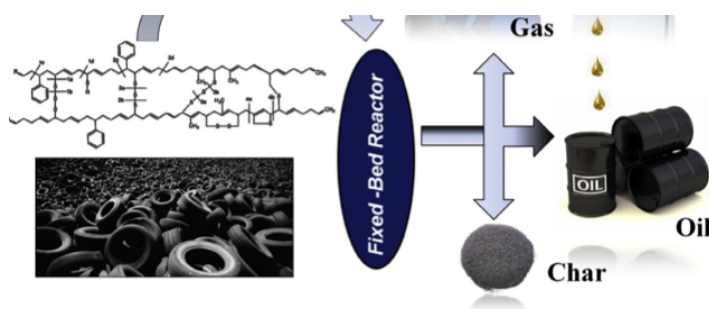


Figure 53 Pyrolysis products: Pyrolytic gas, pyrolytic oil, and carbon black (char) (Ahoor and Zandi-Atashbar 2014)

The gas yield results were collected under consistent pyrolysis operating conditions. All other results under experimental error -such as carrier gas instability or cotton/ catalyst displacement- were discarded and not included in this study.

1. Thermal Pyrolysis

The inert carrier gas used in thermal pyrolysis was nitrogen with a constant flow of 0.0572 l/min. The quartz tube reactor was filled with the same amount of cotton glass between test runs, in order to create constant operating conditions for the condensation of pyrolytic oil. In addition, a fixed distance was preserved between the rubber pieces and

catalyst to allow only vapor to travel to the catalyst and prevent clogging the catalyst with solid carbon (unvaporized portion).

The Hbeta zeolite support and TiO₂ semi-conductor support catalysts were tested with the same rubber-to-catalyst ratio of 0.02862 l/min; the results are listed in Table 17 below.

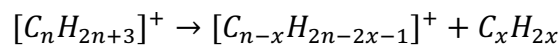
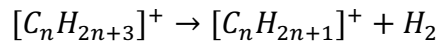
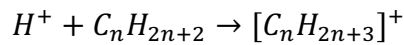
Catalyst	% Gas / N₂
Hbeta zeolite	27.89
Pd/ Hbeta zeolite	37.02
Pt/ Hbeta zeolite	36.43
Pt-Pd/ Hbeta zeolite	26.19
TiO ₂	21.21
Pd/ TiO ₂	37.48
Pt/ TiO ₂	24.39
Pt-Pd/ TiO ₂	35.52
Bi ₂ O ₃ / SiO ₂ / TiO ₂	29.8

Table 17 Thermal pyrolysis gas yield results in the presence of nitrogen carrier gas

In the thermal pyrolysis runs shown in Table 17, the bare catalyst Hbeta zeolite gave a gas yield of **27.89%**. In the absence of heterogeneous catalysts (blank experiment); the gas yield was just **20.33%**. The phenomenon of catalytic cracking caused by Hbeta zeolite is due to the acidic reactivity characteristic of zeolite surfaces. Zeolites have reactive surfaces due to the incorporation of Al³⁺ ions on sites where the Si⁴⁺ ions reside, in addition to the micro pores crystalline structure which offers zeolites the ability to react

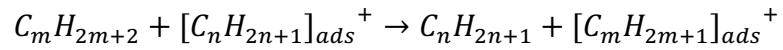
selectively, as shown in Figure 54. This unique characteristic of zeolite in addition to the acidity caused an increase in the gas yield from 20.33% to 27.89%.

The acidic reactivity of zeolite relies on the existence of Bronsted acid extra frame work hydroxyl groups (H^+) (Chorkendorff and Niemantsverdriet 2003). Long chain hydrocarbons are produced from rubber pieces upon attaining high pyrolysis temperatures; once the rubber polymers start to crack, they will flow from the inlet of the quartz fixed bed reactor (Figure 15) crossing through the catalyst (red color). The passage of the gas through the powder catalyst particles provided sufficient contact between the pyrolytic gas and the high surface area of the Hbeta zeolite ($434 \text{ m}^2/\text{g}$). The interference between the hydrogen protons (Bronsted acid site) and the adsorbed hydrocarbon chain was ensured. Therefore, intermediate cations formation and cracking started to take place by beta-scission mechanism as described,



In the presence of Hbeta zeolite the gas yield was not very high and did not exceed 30%. This can be explained by the presence of secondary reactions that took place due to contact between gas and solid. These include polymer recombination, condensation, or carbonaceous reactions. Consequently, the interaction between the

primary reaction cations' intermediates and other new hydrocarbons possibly went as follows:



These results comply with what was concluded by Li X and his team (Li et al. 2009): that long chain normal paraffins including WAX are decomposed into gasoline range hydrocarbons (C₄-C₁₂) via cracking, in addition to the isomerization into Iso-Paraffins on zeolite catalysts (Li et al. 2009).

Zhao T. et al. developed a two-stage reactor having Fischer Tropsch Synthesis catalyst (Fe, Ru, Co) and Hbeta zeolite in the first and second reactors, respectively. It was discovered that the carbon number dropped down after the gas passage was complete in the second reactor (Bouchy et al. 2009). This confirms zeolite's ability to crack down the long-chain normal paraffins hydrocarbons without allowing the cyclic compounds to enter its porous surface.

Furthermore, the synthesized Hbeta zeolite had relatively small pores as reported by BET characterization. This probably hindered the diffusion of complex chain hydrocarbons produced by pyrolysis' primary and secondary reactions.

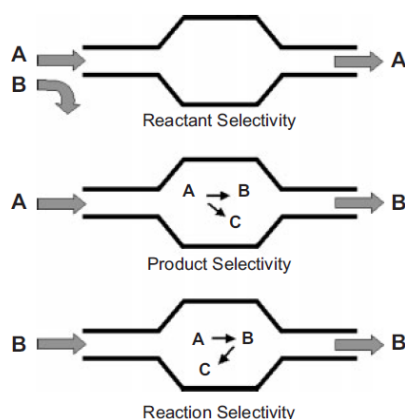


Figure 54 Examples about zeolite selectivity (Chorkendorff and Niemantsverdriet 2003)

Doping Hbeta with palladium metal increased the gas yield to 37.02% (an increase of 32.7%). This higher gas yield production was the result of the synergetic effect between the noble metal and the acidic surface. R. Suarez Paris et al. (2015) investigated the hydro conversion of paraffinic wax over palladium catalyst supported on silica-alumina surfaces. WAX hydro conversion took place via hydrogenation and dehydrogenation on the metal site and isomerization-cracking on the acidic site of heterogeneous bifunctional catalysts. Reaction mechanisms take place by (1) dehydrogenation of an n-paraffin into olefin on the metal site, (2) transformation of olefin to an alkylcarbenium ion by protonation on the acidic site, (3) cracking by beta-scission of the carbenium ion in addition to the skeletal rearrangement on the acidic site, (4) deprotonation of the resulting ion(s) on the acid site, and (5) final hydrogenation of the olefins on the metal site (Weitkamp 2012; Bouchy et al. 2009). Therefore, the metallic sites of palladium increased the catalytic activity by dehydrogenation/hydrogenation to produce olefins that will be cracked and isomerized on the acidic sites.

The cause of the effect of this metal/ acid synergy results in two hypotheses:

1. Increase in hydrogen due to the dehydrogenation reaction initiated by the palladium metallic site (Weitkamp 2012; Bouchy et al. 2009), which in return enhanced hydrocracking reactions that took place on the acidic sites of the zeolite surface. It was mentioned by (Li X. et al 2009), who developed encapsulated Hbeta zeolite enwrapped Co-Al₂O₃ catalyst, that inside the Hbeta zeolite shell, large carbon numbers were cracked down to lighter hydrocarbons and isomerized into Iso-Paraffins by the acidic sites in presence of hydrogen (Feller et al. 2004; Chen et al. 1983).
2. The presence of metallic site palladium (Pd) provoked the dehydrogenation-hydrogenation mechanisms (Weitkamp 2012; Bouchy et al. 2009) and therefore, carbenium ions were produced from olefins production due to hydrogen release, which was adsorbed afterwards on the acidic site ready for beta-scission and isomerization. However, in the absence of metallic site, hydrocarbon chain exhibited dehydrogenation directly on the acidic surface prior to transformation into a carbenium ion. In this case, paraffins experienced hydrogen removal with its lone pair electrons that is binding to the Lewis acid sites of zeolite surface. Hence, the metallic sites assisted the acidic surface initiate hydrogen via this hydrogen exchange steps.

One can argue that in the absence of the metallic site, i.e. absence of dehydrogenation-hydrogenation step done by metal; complex hydrocarbons might not be able to enter the micro pores of the zeolite, which could lead to a lower gas yield. It was mentioned by Aguado et al (2006) that the thermal degradation of hydrocarbons takes place by radical chain reaction pathway consisting of hydrogen transfer steps along with progressive breaking of the hydrocarbon polymer backbone chain. Therefore, palladium metal doped on zeolite might have helped in increasing the gas yield via hydrocarbon adsorption on the metallic site to be protonated by the neighboring acidic support surface

prior to entering the acidic zeolite pore capillaries. Therefore, the produced reactive carbon ion (methyl radical) radicals interfere with other long chains which eventually crack and enter easily into the zeolite pores.

Also from a pore geometry perspective, it is noticed from BET analysis that both pore size and volume increased when palladium was doped on Hbeta zeolite. As shown in Table 9 the pore size went from 2.956 nm to 3.688 nm; i.e. an increase of 24.7%. This is in strong evidence that the pore geometry played a major role in increasing the gas yield by permitting additional amount of complex molecules to enter the catalyst's pores as shown in Figure 54.

Platinum is known for being used in combination with acid catalysts like Hbeta zeolites in the petrochemical industry in fluid catalytic cracking units (FCC). Therefore, it was expected that the gas yield under Pt/Hbeta zeolite will be higher than bare Hbeta zeolite. The cracking property of platinum is highlighted with a gas yield of 36.43% (Table 17). It is revealed (in Table 9) that the surface area decreased from 449 m²/g to 284 m²/g, while the pore size increased from 3.688 nm to 27.74 nm. Even though the surface area decreased, the gas yield remained approximately equal for both Pt and Pd doped Hbeta zeolites. It can be concluded that the larger pore cavity compensated for the lesser external surface area. Moreover, it can be concluded that the catalytic cracking reactions in the presence of Pt/Hbeta zeolite also occurred by the same dehydrogenation-hydrogenation mechanism of Pd/Hbeta zeolite. However, doping palladium metal on Hbeta resulted in a slightly higher gas yield than that attained in the presence of platinum. This minor difference in the gas yield (37.02% versus 36.43%) was analyzed further with the BET results, which confirmed that palladium atoms had a higher dispersion than platinum atoms on the zeolite surface. This is due to the larger size of platinum atoms

compared to palladium. In addition, the difference between the performances of both metals can be investigated from another perspective: the mass transfer difference. As mentioned in the BET analysis section, Pd/Hbeta has a narrower pore size than Pt/Hbeta, therefore, longer residence time would be exhibited for the compounds that enter the catalyst cages.

Regarding the bimetallic Hbeta zeolite catalyst (Pt-Pd/Hbeta zeolite), pyrolytic gas yield decreased from high 30% to 26.2%, which is too close to the conversion of bare Hbeta zeolite (27.8%). This low gas yield can be due to a sharp drop in the surface area to 155 m²/g (Table 9). There is also the probability that the platinum metal (larger atom) covered the palladium metal (smaller atom) and formed a layered structure as shown in Figure 40.

The semi-conductor catalyst was tested separately and in combination with noble metals. Titanium dioxide was used as a separate actual catalyst that is active in hydrocarbon selective oxidation processes (Wainwright and Foster 1979); for instance, TiO₂ was recognized as a heterogeneous catalyst used in fuel processing because of its high thermal and mechanical stability (Kraeutler and Bard 1978; Eschemann et al. 2014). Not only does TiO₂ possess redox abilities, but Lewis Acidity properties as well (Kraeutler and Bard 1978; Eschemann et al. 2014). The gas yield of TiO₂ reached only 21.21% (Table 17) which is slightly higher than the gas yield of the blank experiment (20.33%). Consequently, TiO₂ was not capable of cracking the complex long chain hydrocarbons at similar rates of Hbeta.

The surface chemistry of titanium dioxide surfaces was studied by many researchers. It was reported by Gianmario Marta (2000) that exposed cations Ti⁴⁺ correspond to Lewis acid sites that are coordinated with O²⁻ ligands, which are considered

a Lewis base. Gianmario utilized IR spectra in order to investigate Lewis acid sites on TiO₂ surface, and it was found that there was a band at 2212 cm⁻¹ that was assigned to adsorption of probe CO on more acidic Ti⁴⁺ ions of high Lewis acidity located on edges, steps and corners. The strength of Lewis acidity is relevant to both the number and the geometric arrangement of oxygen anions coordinated to the cationic centers. High Lewis acid sites related to TiO₂ are exposed on (001) and (010) surface planes of P25 sample tested, while weaker Lewis acid are located on larger roundish TiO₂ Merck particles. It was concluded that Lewis acidity strength is not related to the coordination of center cations with surrounding, but it has to do with the geometric arrangement of O²⁻ ligands (Martra 2000).

Again, once palladium was added (on TiO₂), the gas yield jumped to 37.48%. Table 9, shows that the surface area is bit higher than bare TiO₂ and the pore size is wider (48.9m²/g, 3.642 nm). So it can be concluded that palladium interfered with the geometry of TiO₂, thereby influenced the Lewis acidity of center cations Ti⁴⁺. In addition, this shows that the existence of palladium metal plays a major role in hydrogenation-dehydrogenation of hydrocarbons chains accompanied with Lewis acidity of Ti⁴⁺. On the other hand, platinum metal showed a different effect when the gas yield slightly increased to 24.39% (Table 17). It can be seen from Table 9 that the pore size decreased to 2.95 nm when platinum was added to TiO₂ such that platinum could not manipulate any change in the titanium dioxide geometry and therefore, Lewis acidity was somehow close to that of bare TiO₂.

There is a large difference in the gas yield between Pd/TiO₂ case and Pt/TiO₂ case: 37.48% and 24.39%, respectively. This is linked to the smaller pore size of Pt/TiO₂ in comparison with Pd/TiO₂ (**Table 9**), which prevented reactants from reaching the noble

metal Pt residing inside the TiO₂ structure (keep in mind that both Pt and Pd metals were residing within the support structure).

Afterwards, it was interesting to investigate the effect of doping both platinum and palladium as a bimetallic TiO₂ composite catalyst. Pt-Pd/TiO₂ gave 35.52% gas yield which was still less than that of Pd/TiO₂. It can be noticed that the bimetallic Pt-Pd/TiO₂ produced a higher gas yield than Pt-Pd/Hbeta (26.19%) due to the absence of layered framework (Figure 44). Also it can be concluded that once palladium is introduced in Pt-Pd/TiO₂, the gas yield increased to the mid-30s. Whereas the presence of platinum metal along with palladium did not allow the gas yield to reach a higher yield equal to that of a separate palladium metal (37.48%) (Table 17). The presence of the platinum metal doped on TiO₂ seems to be enhancing polymer recombination and thereby preventing the occurrence of volatile non-condensable hydrocarbons. Hence, it is clear that palladium is again interfering with surface geometry of TiO₂ anatase, while platinum could be exerting a retarding effect on the activity of TiO₂ that is related to Lewis acidity.

The last catalyst utilized is the tri-metallic Bi₂O₃/SiO₂/TiO₂ and it yielded a pyrolytic gas of approximately 30% (Table 17). This catalyst is constituted of TiO₂ anatase in addition to the existence of SiO₂ that has introduced Si⁴⁺ cations which act as additional Lewis acid sites. In addition, this catalyst has dual photo-activity due to semiconductor TiO₂ and noble metal bismuth. In comparison with Hbeta based catalysts, the tri-metallic catalyst gave a gas yield of 29.8 wt. % higher than Pt-Pd/Hbeta and bare Hbeta zeolite (26.19% and 27.89% respectively). However, the tri-metallic gas yield (of 29.8%) is still lower than those produced with Pt/Hbeta and Pd/Hbeta (at 36.43% and 37.02%, respectively). Similarly, a comparison is made against TiO₂ based catalysts (Table 17). The tri-metallic catalyst showed a higher gas yield than both TiO₂ bare and Pt/TiO₂ (at

21.21% and 24.39% respectively). On the other hand, the gas yield of the tri-metallic catalyst is still less than the gas yield of both bimetallic Pt-Pd/TiO₂ and Pd/TiO₂ (at 35.52% and 37.48%, respectively). Even though the tri-metallic catalyst has both Lewis acidity and noble metal activity, its gas yield increased to intermediate levels only. This is again due to its layered structure as shown in the SEM image (Figure 45).

2. Solar Pyrolysis

The solar experiments were aimed towards investigating the catalytic activity of all the synthesized catalysts under solar irradiations (UV and visible light). Similarly, carrier gas flow was fixed at a constant value with consistent cotton glass quantity and the same separating distance between the catalyst and rubber. Table 18 shows the pyrolytic gas yield results for all the utilized catalysts.

Catalyst	% Gas
Hbeta zeolite	25.62
Pd/Hbeta zeolite	30.36
Pt/Hbeta zeolite	24.13
Pt-Pd/Hbeta zeolite	28.65
TiO ₂	27.72
Pd/TiO ₂	40.94
Pt/TiO ₂	28.25
Pt-Pd/TiO ₂	39.45
BiO ₂ /SiO ₂ /TiO ₂	32.16

Table 18 Solar pyrolysis gas yield results in the presence of nitrogen carrier gas

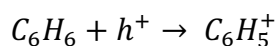
The solar energy received from the sun is collected by using a Fresnel lens (Zeaiter et al. 2015) (Figure 16 Automated solar unit). During the various test runs, we tried to be consistent by adding the same amount of cotton glass and preserving same distance in between the contents (as mentioned before). Solar pyrolysis was also conducted in presence of nitrogen gas with a constant flow rate of 0.02862 l/min.

Solar pyrolysis was conducted in order to examine the effect of the photo activity in addition to the high temperatures due to concentrated solar radiations. Both Hbeta zeolite supported catalysts and semi-conductor TiO₂ based catalysts were tested.

The bare catalyst TiO₂ gave a gas yield of 27.72% (Table 18), while it attained only 21.21% in the thermal pyrolysis runs (Table 17). This gas yield jumped by a factor of 30.7% from thermal to solar conditions where visible light is abundant. This is a clear evidence of the photocatalytic activity of semi-conductor TiO₂ in addition to the Lewis acidity that was mentioned before. It is revealed in literature that titanium dioxide is a major participant in many electrochemical and photo electrochemical applications. In addition to that, TiO₂ is utilized in photo electrolytic cells as well as solar applications, which exploit solar radiations (Wen et al. 2015a).

According to the mentioned information in the photo catalysis section, the titanium dioxide semi-conductor surface will exhibit an electron jump between valence band and conduction band when UV visible light is absorbed, which will leave a positively charged hole. Usually, photo active reactions involve hydroxyl radicals intermediate (OH[·]) that is considered highly reactive species and a major participant in the sequence reaction. However, other reactions are initiated directly by straight oxidation via positively charged holes at the valence band (Xu et al. 2008). In addition, Fox and Dulay (Fox and Dulay 1993) stated that upon hole (positively charged) reaction with an

organic molecule, there will be cation radicals forming a carbenium ion followed by the cracking step at high temperatures.



The direct reaction between the positive hole and a cyclic hydrocarbon, such as benzene, was studied by Hennezel et al. (d'Hennezel et al. 1998). They found that degradation of benzene takes place via direct hole oxidation to produce positive cation.

There are some factors that act as retarding effects on the photo activity of TiO₂ photo catalyst. Catalyst charge recombination also known as electron – hole recombination is known to be a major setback in TiO₂ usage. This phenomenon takes place when there is an absence of an electron donor at the positively charged hole or an electron acceptor at the conduction band; such an action is considered to be an energy waste step (Haque et al. 2012). In addition to that, it is well known that TiO₂ photo catalyst relies on electron excitation from valence band to conduction band that need a threshold energy supplied by UV and visible light harvesting. Therefore, low visible light absorption represents a major disadvantage for photo activity efficiency. Hence, extensive research has been done to focus on increasing the exploitation of visible light by shifting their onset response to visible light range. Metal doping was one of the successful methods that are employed in photoactive fields (Chen and Mao 2007).

Alternatively, it was decided to dope noble metals in order to investigate their effect on preventing electron-hole recombination and therefore, increase the photo catalytic activity. Palladium, platinum and bimetallic doping were applied on TiO₂.

The first composite catalyst used is Pd/TiO₂. It is noticed that the gas yield jumped from 27.27% with TiO₂ to 40.95% with Pd/TiO₂ (Table 18). This is a clear evidence of the enhanced photocatalytic activity that palladium has caused. The increase in catalytic activity can be due to two reasons: the first is that the binding energy of TiO_{2p3/2} shifted to lower values and the second reason is that the TiO₂ spectra changed in the visible light region. J.B. Zhong et al. (2009) investigated the effect of palladium caused on TiO₂ by using UV-vis diffuse reflectance spectra and XPS (Ti2p) spectra as characterization techniques. They discovered -by using the former- that upon doping Pd metal, more visible light is absorbed than bare TiO₂. As a result, Pd/TiO₂ will be excited not only with UV light, but also with visible light. In addition, they found that E_b (Ti_{2p3/2}) of TiO₂ is 459.2 eV and E_b (Ti_{2p1/2}) is 464.3 eV and therefore, the binding energy difference is $\Delta E_b = E_b(Ti_{2p1/2}) - E_b(Ti_{2p3/2}) = 5.72 eV$ (Zhong et al. 2009). The binding energy shifted to a lower value for Pd (0.25%)/TiO₂ to 0.7 eV indicating stronger interaction. Pd/TiO₂ gave 40.94% and 37.48% gas yields in solar and thermal pyrolysis, respectively. This is a clear indication regarding the presence of integrated Lewis acidity and redox ability in Pd/TiO₂ under high temperatures in addition to excess visible light. Concerning the platinum metal, the gas yield was at 28.25% which is not considered to be a significant improvement in comparison to 27.72% for bare TiO₂ (Table 18). It is clear that platinum metal did not interfere with Ti2p spectra and binding energies.

The presence of palladium metal in the bimetallic catalyst Pt-Pd/TiO₂ increased the photo catalytic activity of TiO₂ catalyst by shifting the semi-conductor absorption into visible light range, which is clear by the high gas yield percentage of 39.45 % (Table 18). It is also noticed from Figure 44 that there is an absence of a layered structure that would hinder the activity of the palladium metal.

The tri-metallic catalyst $\text{Bi}_2\text{O}_3/\text{SiO}_2/\text{TiO}_2$ gave a gas yield of approximately 30% (Table 18). The photo catalytic activity of this catalyst was explained by C. Ren et al. (2015) using benzene degradation as substrate to detect the catalytic activity. They conveyed the enhanced photo activity to the band edge position by which the conduction band of p- Bi_2O_3 is lower than bare catalyst TiO_2 conduction band. In such situation, the Bi_2O_3 is acting as electron sink for the emitted electrons from Ti_{3d} conduction band. Consequently, the positively charged holes will move oppositely from the valence band of Bi_2O_3 to the valence band of TiO_2 (O_{2p}). As a result, charge separation becomes more efficient. Nevertheless, the tri-metallic catalyst again showed intermediate level of gas yield (32.16%), which is due to the presence of layered structure shown by SEM (Figure 45).

Regarding the acidic-based catalysts in solar pyrolysis, its activity is concerned with the Bronsted acidity that is favored under high temperatures due to concentrated solar energy. It is noticed that all Hbeta catalysts resulted in a lower gas yield in solar pyrolysis compared to thermal pyrolysis; this is due to the very small differential temperature changes inside the reactor, which is opposite to the uniform surrounding temperatures inside the thermal furnace. Consequently, this have possibly resulted in undesired secondary reactions that would lead to carbon solids formation. As expected, Hbeta zeolite based catalysts suffer from lack of photo activity, unlike TiO_2 semi-conductors which are highly reactive at their superficial positive holes instead of internal active zeolite channels.

C. Pyrolytic Oil Analysis

In order to confirm the improved cracking and isomerization property due to noble metal palladium doping on Hbeta zeolite, the oil samples collected from the quartz tube reactor as shown in Figure 15, were tested by GC-MS in order to detect the hydrocarbon compounds. Samples of oil were collected in vials (Figure 55) and then filtered using a 22 μm syringe. Afterwards, the samples were diluted at a proportion 1:1 using ethanol as solvent. The diluted samples in the vials were placed in the GC auto-sampler, (Trace GC Ultra operated using Xcalibur software).

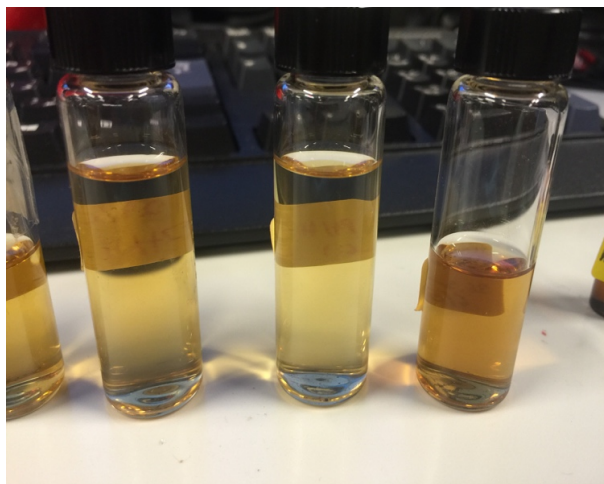


Figure 55 Pyrolytic oil samples diluted with ethanol

The carbon numbers of the hydrocarbons detected in the oil samples produced in presence of Hbeta and Pd/Hbeta catalysts are displayed in Figure 56.

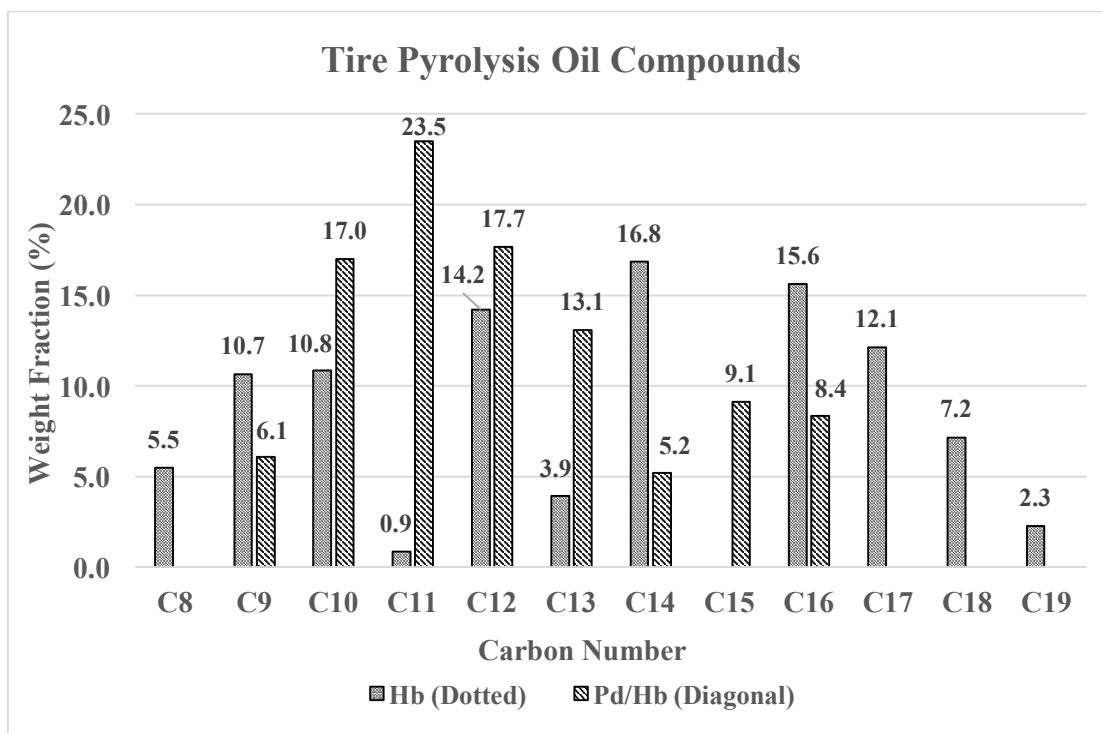


Figure 56 Carbon number distribution in pyrolytic oil with two different catalysts: Hbeta zeolite (Dotted) & Pd/Hbeta (Diagonal)

In the presence of the Hbeta bare catalyst, the pyrolytic oil hydrocarbons gave the highest three peaks of carbon number at values of 14.2%, 16.85% and 15.62% for C₁₂, C₁₄ and C₁₆ (Figure 56), respectively. On the other hand, after doping with Pd metal on the Hbeta zeolite, the majority of the pyrolytic oil hydrocarbons shifted to a lower carbon number range: C₁₀-C₁₃. In other words, the highest carbon number peaks are at values of 16.9%, 23.508% and 17.65% at C₁₀, C₁₁ and C₁₂, respectively (Figure 56). It is worth noting here that there was an occurrence of hydrocarbons with a high range of carbon number: C₁₆-C₁₉, in the presence of Hbeta zeolite only. On the other hand, the Pd/Hbeta catalyst showed minimum presence of hydrocarbons in the former range with only 8.36% at C₁₆ (Figure 56). This is a clear evidence of the influence of the dehydrogenation step

initiated by metallic sites, followed by the protonation and beta-scission mechanism induced by acidic sites of the Hbeta zeolite.

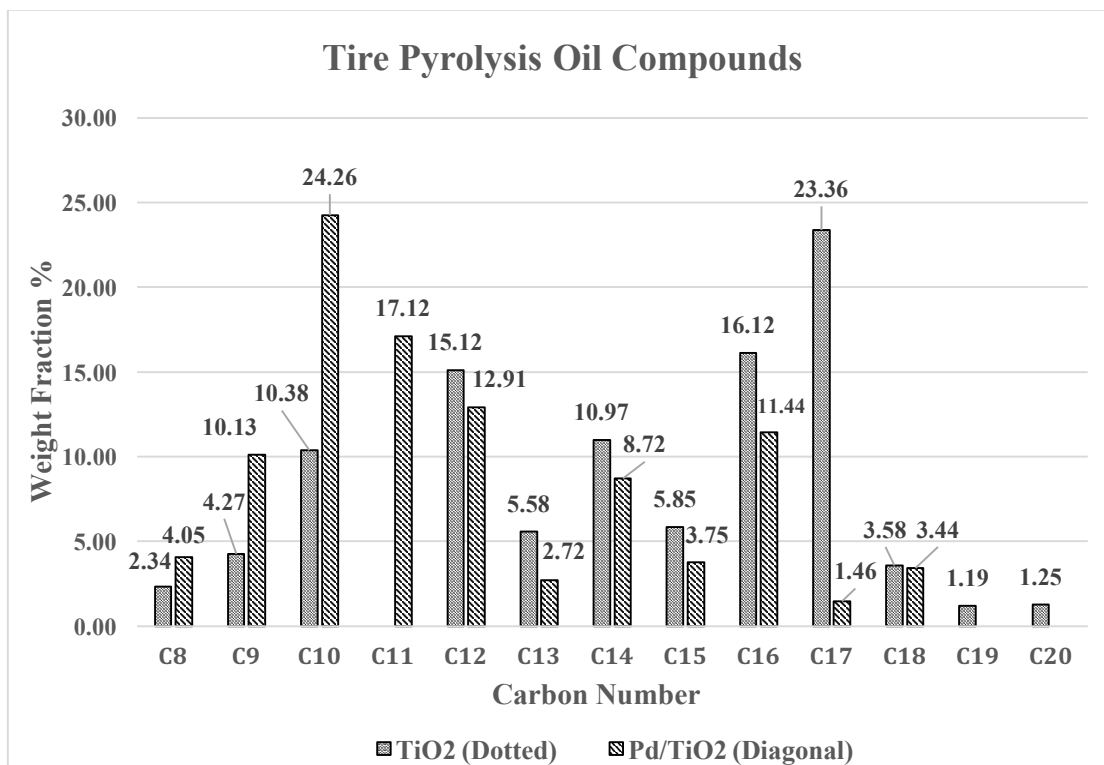


Figure 57 Carbon number distribution in pyrolytic oil with semi-conductor catalysts: TiO₂ (Dotted) & Pd/TiO₂ (Diagonal)

Similarly, the pyrolytic oil samples produced in the presence of the semi-conductor TiO₂ and Pd/TiO₂ were analyzed via GC-MS. The carbon number distributions for the collected oil are displayed in Figure 57.

It is noticed, in the presence of TiO₂, that the highest peaks were at C₁₇, C₁₆ and C₁₂ with values of 23.36%, 16.12%, and 15.12%, respectively (Figure 57). After doping palladium metal on Pd/TiO₂, the hydrocarbons shifted to a lower range of carbon number. For instance, the highest three peaks were detected for carbon numbers C₁₀, C₁₁, and C₁₂ at

values of 24.26%, 17.12%, and 12.91%, respectively. This is a strong evidence of the enhancements that the noble metal palladium brought on TiO_2 causing an increase in cracking.

CONCLUSION

The pyrolysis process considered as a waste to energy method was studied and optimized using heterogeneous catalysts; it was aimed to increase the gas yield % over pyrolytic oil and carbon black yields. Various enhancement strategies to overcome catalysis setbacks and increase activity were investigated via noble metals doping. The pyrolytic oil fractions were studied to investigate the catalyst effect on cracking, isomerization reactions and the carbon number.

The two types of pyrolysis: thermal and solar, were carried out with two different experimental setups under inert nitrogen gas with a constant flow and catalyst: rubber ratio. Nine different catalysts were synthesized by either wet impregnation or pore impregnation method followed by drying and calcination.

The cracking ability of both acidic Hbeta zeolites and semi-conductor TiO₂ catalytic supports were investigated by studying the pyrolytic gas yield conversion of thermal pyrolysis. Moreover, catalytic activity enhancement via noble metals doping was studied by synthesizing Hbeta zeolites and TiO₂ with platinum, palladium or a combination of both metals. The highest gas yield percentage attained was 37.02% in the presence of Pd/Hbeta zeolite followed by Pt/Hbeta zeolite at 36.43%. This is clear evidence of the dehydrogenation-hydrogenation step enhanced by the combination of acidic-noble metal-doped sites. As for the TiO₂ support, again palladium metal showed the highest gas yield of 37.48%, however, platinum doping over TiO₂ showed a weak performance of 24.39%. The BET analysis showed that the best structure was for Pd/Hbeta zeolite, such that the surface area reached 449m²/g and the pore size was 3.688 nm. As a result, using palladium metal resulted in a better catalytic activity and framework structure.

Solar pyrolysis tests helped clarify the photocatalytic activity of the semi-conductor TiO₂ based catalysts and Hbeta zeolite catalysts. Accordingly, it was noticed that TiO₂ bare catalyst had a gas yield (27.72%) higher than that of Hbeta zeolite, which is 25.62%. This implies the existence of both photocatalytic and Lewis acidity for TiO₂ supports. Meanwhile, the highest gas yield attained under solar light was 40.94% for Pd/TiO₂; this confirms that doping palladium metal serves as the best enhancement strategy for upgrading the photocatalytic activity by shifting energy harvesting into visible light region and preventing electron-hole recombination. Semi-conductor TiO₂ catalysts obtained higher conversion levels than Hbeta zeolites under solar energy even with smaller surface area. Hence, it is assumed that hydrocarbon cracking via oxidation takes place at positively charged vacant holes.

Finally, pyrolytic oil results confirmed that cracking took place by heterogeneous catalysts such that the compounds' carbon number decreased from C₁₄-C₁₈ to C₉-C₁₂.

Appendix

A.1

Temperature Interval	Energy Name	Energy Type	Enthalpy Change
25°C & 300°C	Sensible Heat	Endothermic	$C_p\Delta T$
300°C & 450°C	Heat of Reaction	Exothermic	ΔH_{rxn}
450°C & 510°C	Heat of Vaporization	Endothermic	ΔH_{vap}
510°C & 590°C	Sensible Heat	Endothermic	$C_p\Delta T$

Sensible heat (25°C - 300°C):

$$\Delta H_{sens} = C_p\Delta T = 1.895 + 3.18 \times 10^{-3}(573.15 - 298.15) = +522 \text{ KJ/Kg}$$

Heat of reaction (300°C - 450°C):

$$\Delta H_{rxn,SBR} = -560 \text{ KJ/Kg}$$

Heat of vaporization (450°C - 510°C):

$$\Delta H_{vap,SBR} = +180 \text{ KJ/Kg}$$

Sensible heat (510°C - 590°C):

$$\Delta H_{sens} = C_{p,gases}\Delta T = 502 \times 10^{-3}(863 - 783) = +40 \text{ KJ/Kg}$$

$$\Delta H_{sens} = C_{p,carbon}\Delta T = 7700 \times 10^{-3}(863 - 783) = +616 \text{ KJ/Kg}$$

BIBLIOGRAPHY

Aguado, J., Serrano, D., and Escola, J. (2008). "Fuels from waste plastics by thermal and catalytic processes: a review." *Ind Eng Chem Res*, 47(21), 7982-7992.

Aguado, J., Serrano, D., and Escola, J. (2006). "Catalytic upgrading of plastic wastes." *Feedstock Recycling and Pyrolysis of Waste Plastics: Converting Waste Plastics into Diesel and Other Fuels*, 73-110.

Aguado, R., Olazar, M., Vélez, D., Arabiourrutia, M., and Bilbao, J. (2005). "Kinetics of scrap tyre pyrolysis under fast heating conditions." *J.Anal.Appl.Pyrolysis*, 73(2), 290-298.

Ahoor, A. H., and Zandi-Atashbar, N. (2014). "Fuel production based on catalytic pyrolysis of waste tires as an optimized model." *Energy Conversion and Management*, 87 653-669.

Alberici, R. M., Canela, M. C., Eberlin, M. N., and Jardim, W. F. (2001). "Catalyst deactivation in the gas phase destruction of nitrogen-containing organic compounds using TiO₂/UV-VIS." *Applied Catalysis B: Environmental*, 30(3), 389-397.

Aylón, E., Callen, M., López, J., Mastral, A. M., Murillo, R., Navarro, M., and Stelmach, S. (2005). "Assessment of tire devolatilization kinetics." *J.Anal.Appl.Pyrolysis*, 74(1), 259-264.

Aylón, E., Fernández-Colino, A., Murillo, R., Navarro, M., García, T., and Mastral, A. (2010). "Valorisation of waste tyre by pyrolysis in a moving bed reactor." *Waste Manage.*, 30(7), 1220-1224.

Bak, T., Nowotny, J., Rekas, M., and Sorrell, C. (2002). "Photo-electrochemical hydrogen generation from water using solar energy. Materials-related aspects." *Int J Hydrogen Energy*, 27(10), 991-1022.

Barbooti, M. M., Mohamed, T. J., Hussain, A. A., and Abas, F. O. (2004). "Optimization of pyrolysis conditions of scrap tires under inert gas atmosphere." *J.Anal.Appl.Pyrolysis*, 72(1), 165-170.

Beaumont, O., and Schwob, Y. (1984). "Influence of physical and chemical parameters on wood pyrolysis." *Industrial & Engineering Chemistry Process Design and Development*, 23(4), 637-641.

Bennett, G. (1993). *Scrap Tire Technology and Markets: By US Environmental Protection Agency and C.Clark, K.Meardon and D.Russell of Pacific Environmental Services, Noyes Data Corp., Park Ridge, NJ, ISBN 0-8155-1317-8, 1993, 316 Pp., \$54.*

- Berrueco, C., Esperanza, E., Mastral, F., Ceamanos, J., and García-Bacaicoa, P. (2005). "Pyrolysis of waste tyres in an atmospheric static-bed batch reactor: Analysis of the gases obtained." *J.Anal.Appl.Pyrolysis*, 74(1), 245-253.
- Boccuzzi, F., Guglielminotti, E., Martra, G., and Cerrato, G. (1994). "Nitric oxide reduction by CO on Cu/TiO₂ catalysts." *Journal of Catalysis*, 146(2), 449-459.
- Bouchy, C., Hastoy, G., Guillon, E., and Martens, J. (2009). "Fischer-Tropsch waxes upgrading via hydrocracking and selective hydroisomerization." *Oil & Gas Science and Technology-Revue De L'IFP*, 64(1), 91-112.
- Bouvier, J., Charbel, F., and Gelus, M. (1987). "Gas-solid pyrolysis of tire wastes—kinetics and material balances of batch pyrolysis of used tires." *Resources and Conservation*, 15(3), 205-214.
- Bridgwater, A., and Peacocke, G. (2000). "Fast pyrolysis processes for biomass." *Renewable and Sustainable Energy Reviews*, 4(1), 1-73.
- Buekens, A. (2006). "Introduction to feedstock recycling of plastics." *Feedstock Recycling and Pyrolysis of Waste Plastics*, 1-41.
- Buekens, A. (1977). "Some observations on the recycling of plastics and rubber." *Conservation & Recycling*, 1(3-4), 247-271.
- Carneiro, J. T., Savenije, T. J., Moulijn, J. A., and Mul, G. (2011). "How phase composition influences optoelectronic and photocatalytic properties of TiO₂." *The Journal of Physical Chemistry C*, 115(5), 2211-2217.
- Carrasco, F., Bredin, N., Gningue, Y., and Heitz, M. (1998). "Environmental impact of the energy recovery of scrap tires in a cement kiln." *Environ.Technol.*, 19(5), 461-474.
- Cejka, J., Corma, A., and Zones, S. (2010). *Zeolites and catalysis: synthesis, reactions and applications*. John Wiley & Sons, .
- Chang, Y. (1996). "On pyrolysis of waste tire: degradation rate and product yields." *Resour.Conserv.Recycling*, 17(2), 125-139.
- Chen, C., Ma, W., and Zhao, J. (2010a). "Semiconductor-mediated photodegradation of pollutants under visible-light irradiation." *Chem.Soc.Rev.*, 39(11), 4206-4219.
- Chen, C., Ma, W., and Zhao, J. (2010b). "Semiconductor-mediated photodegradation of pollutants under visible-light irradiation." *Chem.Soc.Rev.*, 39(11), 4206-4219.
- Chen, X., and Mao, S. S. (2007a). "Titanium dioxide nanomaterials: synthesis, properties, modifications, and applications." *Chem.Rev.*, 107(7), 2891-2959.
- Chen, X., and Mao, S. S. (2007b). "Titanium dioxide nanomaterials: synthesis, properties, modifications, and applications." *Chem.Rev.*, 107(7), 2891-2959.

Chen, Y., Wang, H., and Goodwin, J. (1983). "Effect of preparation methods on the catalytic properties of zeolite-supported ruthenium in the Fischer-Tropsch synthesis." *Journal of Catalysis*, 83(2), 415-427.

Cheung, K., Lee, K., Lam, K., Chan, T., Lee, C., and Hui, C. (2011). "Operation strategy for multi-stage pyrolysis." *J.Anal.Appl.Pyrolysis*, 91(1), 165-182.

Chorkendorff, I., and Niemantsverdriet, J. (2003). "Introduction to Catalysis." *Concepts of Modern Catalysis and Kinetics*, 1-21.

Collins, L., Downs, W., Gibson, E., and Moore, G. (1974). "An evaluation of discarded tires as a potential source of fuel." *Thermochimica Acta*, 10(2), 153-159.

Conesa, J. A., Font, R., and Marcilla, A. (1996). "Gas from the pyrolysis of scrap tires in a fluidized bed reactor." *Energy Fuels*, 10(1), 134-140.

Conesa, J. A., Gálvez, A., Mateos, F., Martín-Gullón, I., and Font, R. (2008). "Organic and inorganic pollutants from cement kiln stack feeding alternative fuels." *J.Hazard.Mater.*, 158(2), 585-592.

Conesa, J. A., Martin-Gullon, I., Font, R., and Jauhiainen, J. (2004). "Complete study of the pyrolysis and gasification of scrap tires in a pilot plant reactor." *Environ.Sci.Technol.*, 38(11), 3189-3194.

Conner, W. C., Pajonk, G., and Teichner, S. (1986). "Spillover of sorbed species." *Advances in Catalysis*, 34 1-79.

Cunliffe, A. M., and Williams, P. T. (1998). "Composition of oils derived from the batch pyrolysis of tyres." *J.Anal.Appl.Pyrolysis*, 44(2), 131-152.

Cypres, R., and Bettens, B. (1989). "Production of benzoles and active carbon from waste rubber and plastic materials by means of pyrolysis with simultaneous post-cracking." *Pyrolysis and Gasification*, 209-229.

Dai, X., Yin, X., Wu, C., Zhang, W., and Chen, Y. (2001). "Pyrolysis of waste tires in a circulating fluidized-bed reactor." *Energy*, 26(4), 385-399.

Daugaard, D. E., and Brown, R. C. (2003). "Enthalpy for pyrolysis for several types of biomass." *Energy Fuels*, 17(4), 934-939.

de Marco Rodriguez, I., Laresgoiti, M., Cabrero, M., Torres, A., Chomon, M., and Caballero, B. (2001a). "Pyrolysis of scrap tyres." *Fuel Process Technol*, 72(1), 9-22.

de Marco Rodriguez, I., Laresgoiti, M., Cabrero, M., Torres, A., Chomon, M., and Caballero, B. (2001b). "Pyrolysis of scrap tyres." *Fuel Process Technol*, 72(1), 9-22.

- d'Hennezel, O., Pichat, P., and Ollis, D. F. (1998). "Benzene and toluene gas-phase photocatalytic degradation over H₂O and HCL pretreated TiO₂: by-products and mechanisms." *J.Photochem.Photobiol.A.*, 118(3), 197-204.
- Diez, C., Martinez, O., Calvo, L., Cara, J., and Morán, A. (2004). "Pyrolysis of tyres. Influence of the final temperature of the process on emissions and the calorific value of the products recovered." *Waste Manage.*, 24(5), 463-469.
- Dodds, J., Domenico, W., Evans, D., Fish, L., Lassahn, P., and Toth, W. (1983). *Scrap Tires: A Resource and Technology Evaluation of Tire Pyrolysis and Other Selected Alternate Technologies*, .
- Dũng, N. A., Klaewkla, R., Wongkasemjit, S., and Jitkarnka, S. (2009). "Light olefins and light oil production from catalytic pyrolysis of waste tire." *J.Anal.Appl.Pyrolysis*, 86(2), 281-286.
- Einaga, H., Futamura, S., and Ibusuki, T. (2001). "Complete oxidation of benzene in gas phase by platinumized titania photocatalysts." *Environ.Sci.Technol.*, 35(9), 1880-1884.
- Elbaba, I. F., Wu, C., and Williams, P. T. (2010). "Catalytic pyrolysis-gasification of waste tire and tire elastomers for hydrogen production." *Energy Fuels*, 24(7), 3928-3935.
- Ertl, G., Knozinger, H., and Weitkamp, J. (1997). *Handbook of heterogeneous catalysis*. VCH, .
- Eschemann, T. O., Bitter, J. H., and De Jong, K. P. (2014). "Effects of loading and synthesis method of titania-supported cobalt catalysts for Fischer–Tropsch synthesis." *Catalysis Today*, 228 89-95.
- Fan, J., Zhao, L., Yu, J., and Liu, G. (2012). "The effect of calcination temperature on the microstructure and photocatalytic activity of TiO₂-based composite nanotubes prepared by an in situ template dissolution method." *Nanoscale*, 4(20), 6597-6603.
- Feller, A., Guzman, A., Zuazo, I., and Lercher, J. A. (2004). "On the mechanism of catalyzed isobutane/butene alkylation by zeolites." *Journal of Catalysis*, 224(1), 80-93.
- Fernández, A., Barriocanal, C., and Alvarez, R. (2012). "Pyrolysis of a waste from the grinding of scrap tyres." *J.Hazard.Mater.*, 203 236-243.
- Fogler, H. S. (1999). "Elements of chemical reaction engineering." .
- Fox, M. A., and Dulay, M. T. (1993). "Heterogeneous photocatalysis." *Chem.Rev.*, 93(1), 341-357.
- Fujishima, A. (1972). "Electrochemical photolysis of water at a semiconductor electrode." *Nature*, 238 37-38.

- Fujishima, A., Rao, T. N., and Tryk, D. A. (2000). "Titanium dioxide photocatalysis." *Journal of Photochemistry and Photobiology C: Photochemistry Reviews*, 1(1), 1-21.
- Galvagno, S., Casu, S., Casabianca, T., Calabrese, A., and Cornacchia, G. (2002). "Pyrolysis process for the treatment of scrap tyres: preliminary experimental results." *Waste Manage.*, 22(8), 917-923.
- Gieré, R., Smith, K., and Blackford, M. (2006). "Chemical composition of fuels and emissions from a coal tire combustion experiment in a power station." *Fuel*, 85(16), 2278-2285.
- Gomez, C., Velo, E., Barontini, F., and Cozzani, V. (2009). "Influence of secondary reactions on the heat of pyrolysis of biomass." *Ind Eng Chem Res*, 48(23), 10222-10233.
- Gonzales, N. O., Bell, A. T., and Chakraborty, A. K. (1997). "Density functional theory calculations of the effects of local composition and defect structure on the proton affinity of H-ZSM-5." *The Journal of Physical Chemistry B*, 101(48), 10058-10064.
- González, J. F., Encinar, J. M., Canito, J. L., and Rodríguez, J. J. (2001). "Pyrolysis of automobile tyre waste. Influence of operating variables and kinetics study." *J.Anal.Appl.Pyrolysis*, 58 667-683.
- Groves, S. A., Lehrle, R. S., Blazsó, M., and Székely, T. (1991). "Natural rubber pyrolysis: Study of temperature-and thickness-dependence indicates dimer formation mechanism." *J.Anal.Appl.Pyrolysis*, 19 301-309.
- Haller, G. L., and Resasco, D. E. (1989). "Metal-support interaction: Group VIII metals and reducible oxides." *Advances in Catalysis*, 36 173-235.
- Haque, M. M., Bahnemann, D., and Muneer, M. (2012). *Photocatalytic degradation of organic pollutants: Mechanisms and Kinetics*. INTECH Open Access Publisher, .
- Haruta, M., Yamada, N., Kobayashi, T., and Iijima, S. (1989). "Gold catalysts prepared by coprecipitation for low-temperature oxidation of hydrogen and of carbon monoxide." *Journal of Catalysis*, 115(2), 301-309.
- Herlan, A. (1978). "On the formation of polycyclic aromatics: Investigation of fuel oil and emissions by high-resolution mass spectrometry." *Combust.Flame*, 31 297-307.
- Hosseini, M., Siffert, S., Tidahy, H., Cousin, R., Lamonier, J., Aboukais, A., Vantomme, A., Roussel, M., and Su, B. (2007). "Promotional effect of gold added to palladium supported on a new mesoporous TiO₂ for total oxidation of volatile organic compounds." *Catalysis Today*, 122(3), 391-396.
- Hu, X., Li, G., and Yu, J. C. (2009). "Design, fabrication, and modification of nanostructured semiconductor materials for environmental and energy applications." *Langmuir*, 26(5), 3031-3039.

- Isayev, A. (2005). "Recycling of rubber." .
- Islam, M. R., Haniu, H., and Beg, M. R. A. (2008). "Liquid fuels and chemicals from pyrolysis of motorcycle tire waste: product yields, compositions and related properties." *Fuel*, 87(13), 3112-3122.
- Jimmy, C. Y., Yu, J., and Zhao, J. (2002). "Enhanced photocatalytic activity of mesoporous and ordinary TiO₂ thin films by sulfuric acid treatment." *Applied Catalysis B: Environmental*, 36(1), 31-43.
- Kaminsky, W., Mennerich, C., and Zhang, Z. (2009). "Feedstock recycling of synthetic and natural rubber by pyrolysis in a fluidized bed." *J.Anal.Appl.Pyrolysis*, 85(1), 334-337.
- Kaminsky, W., and Sinn, H. (1980). "Pyrolysis of plastic waste and scrap tires using a fluidized-bed process." *ACS Symp. Ser.:(United States)*, Universitaet Hamburg, Germany, .
- Kar, Y. (2011). "Catalytic pyrolysis of car tire waste using expanded perlite." *Waste Manage.*, 31(8), 1772-1782.
- Kennedy, J. C., and Datye, A. K. (1998). "Photothermal heterogeneous oxidation of ethanol over Pt/TiO₂." *Journal of Catalysis*, 179(2), 375-389.
- Kim, S. B., and Hong, S. C. (2002). "Kinetic study for photocatalytic degradation of volatile organic compounds in air using thin film TiO₂ photocatalyst." *Applied Catalysis B: Environmental*, 35(4), 305-315.
- Kim, T., Lee, M., Lee, S., Park, Y., Jung, C., and Boo, J. (2005). "Development of surface coating technology of TiO₂ powder and improvement of photocatalytic activity by surface modification." *Thin Solid Films*, 475(1), 171-177.
- Kraeutler, B., and Bard, A. J. (1978). "Heterogeneous photocatalytic preparation of supported catalysts. Photodeposition of platinum on titanium dioxide powder and other substrates." *J.Am.Chem.Soc.*, 100(13), 4317-4318.
- Kudo, A., and Miseki, Y. (2009a). "Heterogeneous photocatalyst materials for water splitting." *Chem.Soc.Rev.*, 38(1), 253-278.
- Kudo, A., and Miseki, Y. (2009b). "Heterogeneous photocatalyst materials for water splitting." *Chem.Soc.Rev.*, 38(1), 253-278.
- Kühl, G. (1977). "The coordination of aluminum and silicon in zeolites as studied by x-ray spectrometry." *Journal of Physics and Chemistry of Solids*, 38(11), 1259-1263.
- Kühl, G. H. (1999). "Modification of zeolites." *Catalysis and Zeolites*, Springer, 81-197.

Kwon, E., and Castaldi, M. J. (2009). "Fundamental understanding of the thermal degradation mechanisms of waste tires and their air pollutant generation in a N₂ atmosphere." *Environ.Sci.Technol.*, 43(15), 5996-6002.

Kwon, E., and Castaldi, M. J. (2008). "Investigation of mechanisms of polycyclic aromatic hydrocarbons (PAHs) initiated from the thermal degradation of styrene butadiene rubber (SBR) in N₂ atmosphere." *Environ.Sci.Technol.*, 42(6), 2175-2180.

Kyari, M., Cunliffe, A., and Williams, P. T. (2005). "Characterization of oils, gases, and char in relation to the pyrolysis of different brands of scrap automotive tires." *Energy Fuels*, 19(3), 1165-1173.

Laird, D. A., Brown, R. C., Amonette, J. E., and Lehmann, J. (2009). "Review of the pyrolysis platform for coproducing bio- oil and biochar." *Biofuels, Bioproducts and Biorefining*, 3(5), 547-562.

Leung, D., and Wang, C. (1998). "Kinetic study of scrap tyre pyrolysis and combustion." *J.Anal.Appl.Pyrolysis*, 45(2), 153-169.

Levendis, Y. A., Atal, A., Carlson, J., Dunayevskiy, Y., and Vouros, P. (1996). "Comparative study on the combustion and emissions of waste tire crumb and pulverized coal." *Environ.Sci.Technol.*, 30(9), 2742-2754.

Li, S., Yao, Q., Chi, Y., Yan, J., and Cen, K. (2004a). "Pilot-scale pyrolysis of scrap tires in a continuous rotary kiln reactor." *Ind Eng Chem Res*, 43(17), 5133-5145.

Li, S., Yao, Q., Chi, Y., Yan, J., and Cen, K. (2004b). "Pilot-scale pyrolysis of scrap tires in a continuous rotary kiln reactor." *Ind Eng Chem Res*, 43(17), 5133-5145.

Li, X., He, J., Meng, M., Yoneyama, Y., and Tsubaki, N. (2009). "One-step synthesis of H- β zeolite-enwrapped Co/Al₂O₃ Fischer-Tropsch catalyst with high spatial selectivity." *Journal of Catalysis*, 265(1), 26-34.

Litter, M. I. (1999). "Heterogeneous photocatalysis: transition metal ions in photocatalytic systems." *Applied Catalysis B: Environmental*, 23(2), 89-114.

Liu, G., Yang, H. G., Pan, J., Yang, Y. Q., Lu, G. Q., and Cheng, H. (2014a). "Titanium dioxide crystals with tailored facets." *Chem.Rev.*, 114(19), 9559-9612.

Liu, K., Cao, M., Fujishima, A., and Jiang, L. (2014b). "Bio-inspired titanium dioxide materials with special wettability and their applications." *Chem.Rev.*, 114(19), 10044-10094.

Liu, L., and Chen, X. (2014). "Titanium dioxide nanomaterials: Self-structural modifications." *Chem.Rev.*, 114(19), 9890-9918.

- Lloyd, A. C. (2006). "Technology Evaluation and Economic Analysis of Waste Tire Pyrolysis, Gasification, and Liquefaction." *University of California Riverside, Integrated Waste Management Board*, 97.
- López, G., Olazar, M., Aguado, R., and Bilbao, J. (2010). "Continuous pyrolysis of waste tyres in a conical spouted bed reactor." *Fuel*, 89(8), 1946-1952.
- Lopez, G., Olazar, M., Amutio, M., Aguado, R., and Bilbao, J. (2009). "Influence of tire formulation on the products of continuous pyrolysis in a conical spouted bed reactor." *Energy Fuels*, 23(11), 5423-5431.
- Lv, K., Cheng, B., Yu, J., and Liu, G. (2012). "Fluorine ions-mediated morphology control of anatase TiO₂ with enhanced photocatalytic activity." *Physical Chemistry Chemical Physics*, 14(16), 5349-5362.
- Lv, K., Xiang, Q., and Yu, J. (2011). "Effect of calcination temperature on morphology and photocatalytic activity of anatase TiO₂ nanosheets with exposed {001} facets." *Applied Catalysis B: Environmental*, 104(3), 275-281.
- Ma, Y., Wang, X., Jia, Y., Chen, X., Han, H., and Li, C. (2014). "Titanium dioxide-based nanomaterials for photocatalytic fuel generations." *Chem.Rev.*, 114(19), 9987-10043.
- Maeda, K. (2011). "Photocatalytic water splitting using semiconductor particles: history and recent developments." *Journal of Photochemistry and Photobiology C: Photochemistry Reviews*, 12(4), 237-268.
- Maher, P., Hunter, F., and Scherzer, J. (1971). "Crystal structures of ultrastable faujasites." *Adv.Chem.Ser.*, 101 266-278.
- Maira, A., Yeung, K. L., Soria, J., Coronado, J., Belver, C., Lee, C., and Augugliaro, V. (2001). "Gas-phase photo-oxidation of toluene using nanometer-size TiO₂ catalysts." *Applied Catalysis B: Environmental*, 29(4), 327-336.
- Malkow, T. (2004). "Novel and innovative pyrolysis and gasification technologies for energy efficient and environmentally sound MSW disposal." *Waste Manage.*, 24(1), 53-79.
- Marci, G., Addamo, M., Augugliaro, V., Coluccia, S., Garcia-López, E., Loddo, V., Martra, G., Palmisano, L., and Schiavello, M. (2003). "Photocatalytic oxidation of toluene on irradiated TiO₂: comparison of degradation performance in humidified air, in water and in water containing a zwitterionic surfactant." *J.Photochem.Photobiol.A.*, 160(1), 105-114.
- Martínez, J. D., Puy, N., Murillo, R., García, T., Navarro, M. V., and Mastral, A. M. (2013). "Waste tyre pyrolysis—a review." *Renewable and Sustainable Energy Reviews*, 23 179-213.

- Martra, G. (2000). "Lewis acid and base sites at the surface of microcrystalline TiO₂ anatase: relationships between surface morphology and chemical behaviour." *Applied Catalysis A: General*, 200(1), 275-285.
- Mastral, A., Callen, M., and Garcia, T. (2000a). "Fluidized bed combustion (FBC) of fossil and nonfossil fuels. A comparative study." *Energy Fuels*, 14(2), 275-281.
- Mastral, A., Murillo, R., Callen, M., Garcia, T., and Snape, C. (2000b). "Influence of process variables on oils from tire pyrolysis and hydrolysis in a swept fixed bed reactor." *Energy Fuels*, 14(4), 739-744.
- Mastral, A., Murillo, R., Callén, M., and Garcia, T. (1999a). "Application of coal conversion technology to tire processing." *Fuel Process Technol*, 60(3), 231-242.
- Mastral, A. M., Callén, M. S., Murillo, R., and García, T. (1999b). "Combustion of high calorific value waste material: Organic atmospheric pollution." *Environ.Sci.Technol.*, 33(23), 4155-4158.
- Mastral, A. M., Murillo, R., Perez-Surio, M. J., and Callén, M. (1996). "Coal hydrocprocessing with tires and tire components." *Energy Fuels*, 10(4), 941-947.
- Miguel, G. S., Fowler, G. D., and Sollars, C. J. (1998). "Pyrolysis of tire rubber: porosity and adsorption characteristics of the pyrolytic chars." *Ind Eng Chem Res*, 37(6), 2430-2435.
- Murillo, R., Aylón, E., Navarro, M., Callén, M., Aranda, A., and Mastral, A. (2006a). "The application of thermal processes to valorise waste tyre." *Fuel Process Technol*, 87(2), 143-147.
- Murillo, R., Aranda, A., Aylón, E., Callén, M. S., and Mastral, A. M. (2006b). "Process for the separation of gas products from waste tire pyrolysis." *Ind Eng Chem Res*, 45(5), 1734-1738.
- Napoli, A., Soudais, Y., Lecomte, D., and Castillo, S. (1997). "Scrap tyre pyrolysis: Are the effluents valuable products?" *J.Anal.Appl.Pyrolysis*, 40 373-382.
- Ni, M., Leung, M. K., Leung, D. Y., and Sumathy, K. (2007). "A review and recent developments in photocatalytic water-splitting using TiO₂ for hydrogen production." *Renewable and Sustainable Energy Reviews*, 11(3), 401-425.
- Ochiai, T., and Fujishima, A. (2012). "Photoelectrochemical properties of TiO₂ photocatalyst and its applications for environmental purification." *Journal of Photochemistry and Photobiology C: Photochemistry Reviews*, 13(4), 247-262.
- Oyedun, A., Lam, K., Fittkau, M., and Hui, C. (2012). "Optimisation of particle size in waste tyre pyrolysis." *Fuel*, 95 417-424.

Pakdel, H., Pantea, D. M., and Roy, C. (2001). "Production of dl-limonene by vacuum pyrolysis of used tires." *J.Anal.Appl.Pyrolysis*, 57(1), 91-107.

Park, H., Park, Y., Kim, W., and Choi, W. (2013). "Surface modification of TiO₂ photocatalyst for environmental applications." *Journal of Photochemistry and Photobiology C: Photochemistry Reviews*, 15 1-20.

Pasternak, S., and Paz, Y. (2013). "On the similarity and dissimilarity between photocatalytic water splitting and photocatalytic degradation of pollutants." *ChemPhysChem*, 14(10), 2059-2070.

Ren, C., Qiu, W., Zhang, H., He, Z., and Chen, Y. (2015). "Degradation of benzene on TiO₂/SiO₂/Bi₂O₃ photocatalysts under UV and visible light." *Journal of Molecular Catalysis A: Chemical*, 398 215-222.

Rezaiyan, J., and Cheremisinoff, N. P. (2005). *Gasification technologies: a primer for engineers and scientists*. CRC press, .

Roy, C., Darmstadt, H., Benallal, B., and Amen-Chen, C. (1997). "Characterization of naphtha and carbon black obtained by vacuum pyrolysis of polyisoprene rubber." *Fuel Process Technol*, 50(1), 87-103.

Roy, C., Labrecque, B., and de Caumia, B. (1990). "Recycling of scrap tires to oil and carbon black by vacuum pyrolysis." *Resour.Conserv.Recycling*, 4(3), 203-213.

Sakai, N., Fujishima, A., Watanabe, T., and Hashimoto, K. (2003). "Quantitative evaluation of the photoinduced hydrophilic conversion properties of TiO₂ thin film surfaces by the reciprocal of contact angle." *The Journal of Physical Chemistry B*, 107(4), 1028-1035.

Scheirs, J. (2006a). "Overview of commercial pyrolysis processes for waste plastics." *Feedstock Recycling and Pyrolysis of Waste Plastics: Converting Waste Plastics into Diesel and Other Fuels*, 381-433.

Scheirs, J. (2006b). "Overview of commercial pyrolysis processes for waste plastics." *Feedstock Recycling and Pyrolysis of Waste Plastics: Converting Waste Plastics into Diesel and Other Fuels*, 381-433.

Scheirs, J., and Kaminsky, W. (2006). *Feedstock recycling and pyrolysis of waste plastics*. John Wiley & Sons, .

Shulman, V. (2004). *Tyre recycling*. iSmithers Rapra Publishing, .

Sinn, H., Kaminsky, W., and Janning, J. (1976). "Processing of plastic waste and scrap tires into chemical raw materials, especially by pyrolysis." *Angewandte Chemie International Edition in English*, 15(11), 660-672.

- Sun, B., Smirniotis, P. G., and Boolchand, P. (2005). "Visible light photocatalysis with platinized rutile TiO₂ for aqueous organic oxidation." *Langmuir*, 21(24), 11397-11403.
- Tada, H., Ishida, T., Takao, A., and Ito, S. (2004). "Drastic enhancement of TiO₂-photocatalyzed reduction of nitrobenzene by loading Ag clusters." *Langmuir*, 20(19), 7898-7900.
- Ucar, S., Karagoz, S., Ozkan, A. R., and Yanik, J. (2005). "Evaluation of two different scrap tires as hydrocarbon source by pyrolysis." *Fuel*, 84(14), 1884-1892.
- Unapumnuk, K., Keener, T. C., Lu, M., and Liang, F. (2008). "Investigation into the removal of sulfur from tire derived fuel by pyrolysis." *Fuel*, 87(6), 951-956.
- Vannice, M. A. (1982). "Titania-supported metals as CO hydrogenation catalysts." *Journal of Catalysis*, 74(1), 199-202.
- Von Ballmoos, R., Harris, D., Magee, J., Ertl, G., Knözinger, H., and Weitkamp, J. (1997). "Handbook of Heterogeneous Catalysis." .
- Vorontsov, A., Kurkin, E., and Savinov, E. (1999). "Study of TiO₂ deactivation during gaseous acetone photocatalytic oxidation." *Journal of Catalysis*, 186(2), 318-324.
- Wainwright, M. S., and Foster, N. R. (1979). "Catalysts, kinetics and reactor design in phthalic anhydride synthesis." *Catalysis Reviews—Science and Engineering*, 19(2), 211-292.
- Wampler, T. P. (2006). *Applied pyrolysis handbook*. CRC Press, .
- Wang, J., Zhong, J., Gong, M. C., Wang, M., and Chen, Y. (2005a). *Gas-Phase Photocatalytic Oxidation of Benzene Over Titanium Dioxide Loaded on Strontium Cerate*, .
- Wang, R., Hashimoto, K., Fujishima, A., Chikuni, M., Kojima, E., Kitamura, A., Shimohigoshi, M., and Watanabe, T. (1998). "Photogeneration of highly amphiphilic TiO₂ surfaces." *Adv Mater*, 10(2), 135-138.
- Wang, X., Yu, J. C., Hou, Y., and Fu, X. (2005b). "Three- Dimensionally Ordered Mesoporous Molecular- Sieve Films as Solid Superacid Photocatalysts." *Adv Mater*, 17(1), 99-102.
- Wang, X., Yu, J. C., Hou, Y., and Fu, X. (2005c). "Three- Dimensionally Ordered Mesoporous Molecular- Sieve Films as Solid Superacid Photocatalysts." *Adv Mater*, 17(1), 99-102.
- Weitkamp, J. (2012). "Catalytic hydrocracking—mechanisms and versatility of the process." *ChemCatChem*, 4(3), 292-306.

Wen, J., Li, X., Liu, W., Fang, Y., Xie, J., and Xu, Y. (2015a). "Photocatalysis fundamentals and surface modification of TiO₂ nanomaterials." *Chinese Journal of Catalysis*, 36(12), 2049-2070.

Wen, J., Li, X., Liu, W., Fang, Y., Xie, J., and Xu, Y. (2015b). "Photocatalysis fundamentals and surface modification of TiO₂ nanomaterials." *Chinese Journal of Catalysis*, 36(12), 2049-2070.

Williams, P. T., and Besler, S. (1995). "Pyrolysis-thermogravimetric analysis of tyres and tyre components." *Fuel*, 74(9), 1277-1283.

Williams, P. T., Besler, S., and Taylor, D. T. (1990). "The pyrolysis of scrap automotive tyres: The influence of temperature and heating rate on product composition." *Fuel*, 69(12), 1474-1482.

Williams, P. T., and Brindle, A. J. (2002). "Catalytic pyrolysis of tyres: influence of catalyst temperature." *Fuel*, 81(18), 2425-2434.

Williams, P., Besler, S., Taylor, D., and Bottrill, R. (1995). "The pyrolysis of automotive tyre waste." *J.Inst.Energy*, 68(474), 11-21.

Xu, J., Ao, Y., Fu, D., and Yuan, C. (2008). "Synthesis of Bi₂O₃-TiO₂ composite film with high-photocatalytic activity under sunlight irradiation." *Appl.Surf.Sci.*, 255(5), 2365-2369.

Yang, J., and Roy, C. (1996). "A new method for DTA measurement of enthalpy change during the pyrolysis of rubbers." *Thermochimica Acta*, 288(1), 155-168.

Yu, J., Jimmy, C. Y., Ho, W., and Jiang, Z. (2002). "Effects of calcination temperature on the photocatalytic activity and photo-induced super-hydrophilicity of mesoporous TiO₂ thin films." *New Journal of Chemistry*, 26(5), 607-613.

Yu, J., Jimmy, C. Y., Ho, W., Leung, M. K., Cheng, B., Zhang, G., and Zhao, X. (2003a). "Effects of alcohol content and calcination temperature on the textural properties of bimodally mesoporous titania." *Applied Catalysis A: General*, 255(2), 309-320.

Yu, J., Jimmy, C. Y., Leung, M. K., Ho, W., Cheng, B., Zhao, X., and Zhao, J. (2003b). "Effects of acidic and basic hydrolysis catalysts on the photocatalytic activity and microstructures of bimodal mesoporous titania." *Journal of Catalysis*, 217(1), 69-78.

Yu, J., Yu, H., Cheng, B., Zhao, X., Yu, J. C., and Ho, W. (2003c). "The effect of calcination temperature on the surface microstructure and photocatalytic activity of TiO₂ thin films prepared by liquid phase deposition." *The Journal of Physical Chemistry B*, 107(50), 13871-13879.

Zeaiter, J., Ahmad, M. N., Rooney, D., Samneh, B., and Shammas, E. (2015). "Design of an automated solar concentrator for the pyrolysis of scrap rubber." *Energy Conversion and Management*, 101 118-125.

Zhang, Q. (2003). "Gas-phase photo catalytic reaction properties of benzene on TiO₂." *China Environmental Science-Chinese Edition*, 23(6), 661-664.

Zhang, Q., Zhang, F., and Zhang, G. (2004). "Reaction mechanism of gas-phase photocatalytic oxidation of benzene on TiO₂." *Chinese Journal of Catalysis*, 25(1), 39-43.

Zhang, X., Wang, T., Ma, L., and Chang, J. (2008). "Vacuum pyrolysis of waste tires with basic additives." *Waste Manage.*, 28(11), 2301-2310.

Zhong, J. B., Lu, Y., Jiang, W. D., Meng, Q. M., He, X. Y., Li, J. Z., and Chen, Y. Q. (2009). "Characterization and photocatalytic property of Pd/TiO₂ with the oxidation of gaseous benzene." *J.Hazard.Mater.*, 168(2), 1632-1635.

Zhou, M., Yu, J., Liu, S., Zhai, P., and Jiang, L. (2008). "Effects of calcination temperatures on photocatalytic activity of SnO₂/TiO₂ composite films prepared by an EPD method." *J.Hazard.Mater.*, 154(1), 1141-1148.